Characterization of Fatigue Damage in Aerospace Materials under Complex Multiaxial Loading

by

Siddhant Datta

A Dissertation Presented in Partial Fulfillment
of the Requirements for the Degree
Doctor of Philosophy

Approved August 2018 by the
Graduate Supervisory Committee:

Aditi Chattopadhyay, Chair
Yongming Liu
Hanqing Jiang
Hamidreza Marvi
Pingbo Tang
Nagaraja Iyyer
Masoud Yekani Fard

ARIZONA STATE UNIVERSITY

December 2018

ABSTRACT

Multiaxial mechanical fatigue of heterogeneous materials has been a significant cause of concern in the aerospace, civil and automobile industries for decades, limiting the service life of structural components while increasing time and costs associated with inspection and maintenance. Fiber reinforced composites and light-weight aluminum alloys are widely used in aerospace structures that require high specific strength and fatigue resistance. However, studying the fundamental crack growth behavior at the micro- and macroscale as a function of loading history is essential to accurately predict the residual fatigue life of components and achieve damage tolerant designs. The issue of mechanical fatigue can be tackled by developing reliable in-situ damage quantification methodologies and by comprehensively understanding fatigue damage mechanisms under a variety of complex loading conditions. Although a multitude of uniaxial fatigue loading studies have been conducted on light-weight metallic materials and composites, many service failures occur from components being subjected to variable amplitude, mixed-mode multiaxial fatigue loadings. In this research, a systematic approach is undertaken to address the issue of fatigue damage evolution in aerospace materials by:

(i) Comprehensive investigation of micro- and macroscale crack growth behavior in aerospace grade Al 7075 T651 alloy under complex biaxial fatigue loading conditions. The effects of variable amplitude biaxial loading on crack growth characteristics such as crack acceleration and retardation were studied in detail by exclusively analyzing the influence of individual mode-I, mixed-mode and mode-II overload and underload fatigue cycles in an otherwise constant amplitude mode-

I baseline load spectrum. The micromechanisms governing crack growth behavior under the complex biaxial loading conditions were identified and correlated with the crack growth behavior and fracture surface morphology through quantitative fractography.

(ii) Development of novel multifunctional nanocomposite materials with improved fatigue resistance and *in-situ* fatigue damage detection and quantification capabilities. A state-of-the-art processing method was developed for producing sizable carbon nanotube (CNT) membranes for multifunctional composites. The CNT membranes were embedded in glass fiber laminates and *in-situ* strain sensing and damage quantification was achieved by exploiting the piezoresistive property of the CNT membrane. In addition, improved resistance to fatigue crack growth was observed due to the embedded CNT membrane.

The sun is the same, in a relative way, but you are older

-Floyd

ACKNOWLEDGMENTS

I would like to express my deepest gratitude to my advisor, Regents' Professor Aditi Chattopadhyay for her valuable advice, encouragement and support throughout my doctoral studies. I am sincerely grateful for the guidance and challenges she provided, which developed in me a passion for research. I would also like to thank the members of my Supervisory Committee, Prof. Yongming Liu, Prof. Hanqing Jiang, Prof. Hamidreza Marvi, Prof. Pingbo Tang, Prof. Masoud Yekani Fard and Dr. Nagaraja Iyyer for volunteering their time to provide valuable insight and advice in regard to my research. I would like to appreciate the guidance and mentorship I've received from Dr. Yingtao Liu and Dr. Bonsung Koo. Dr. Liu helped me realize the importance of publishing quality research work and gave me the opportunity to learn under his guidance. I would also like to thank my friends and fellow graduate students for their support, feedback and friendship which created a pleasant work environment. I would also like to express my gratitude to Dr. B.M. Nagabhushana, who introduced me to the world of scientific research during my undergraduate degree. Special thanks to my girlfriend, Dr. Tulika Shokeen, for believing in me and supporting all my decisions throughout the course of my education from high school, all the way till the completion of my graduate studies.

I would like to thank the funding agencies for the research presented in this dissertation, which is supported in part by the US Naval Air Systems Command and Technical Data Analysis, prime contract #N68335-16-G-0009, DO 0001, Program manager Dr. Nagaraja Iyyer, Technical Monitor Dr. Nam Phan; Office of Naval Research, under the Grant N00014-17-1-2037, Program Manager Mr. William Nickerson.

TABLE OF CONTENTS

Page

CHAPTER Page

LIST OF TABLES

Table Page

LIST OF FIGURES

Figure Page

Figure Page

Figure Page

1 INTRODUCTION

1.1 Motivation

Service lives of aerospace structures often comprise multiaxial mechanical fatigue conditions that deteriorate the strength and integrity of the structures over time. Furthermore, mechanical fatigue damage has been recognized to be the leading cause of structural failure in the aerospace industry, causing major concern regarding the safety, inspection, and maintenance of aircrafts. The material systems used in aerospace structures must satisfy the unique criteria of possessing high specific-strength, stiffness and fatigue resistance. Hence several light-weight heterogeneous materials systems, such as fiber-reinforced polymer (FRP) composite materials and Aluminum alloys, have been extensively used in these structures, however their governing fatigue damage mechanisms have been found to be distinctly different. A multitude of fatigue studies have been conducted to understand the damage evolution mechanisms in aerospace materials with the goal of: i) developing accurate prediction methodologies for residual useful life (RUL); ii) detecting and quantifying damage evolution in real-time to monitor structural integrity and safety.

Most research studies published in literature on aerospace grade Al alloys have been conducted under uniaxial fatigue loading conditions, and the corresponding crack initiation and propagation mechanisms have been thoroughly investigated. In the past, uniaxial fatigue loading has been applied on suitably designed specimens through specialized load-transfer fixtures to induce different fatigue-fracture modes (mode I, II and

III), and several researchers have studied the damage initiation and propagation characteristics under different combinations of mixed-mode fatigue loads. However, in realistic service life conditions, the fatigue loads are often multiaxial with variable amplitudes and can be in-phase or out-of-phase, leading to complex fatigue-fracture behavior. Multiaxial fatigue studies are relatively uncommon due to the requirement of expensive and complex multi-actuator testframes. Hence, there is a need for comprehensive experimental investigation of multiaxial fatigue behavior of aerospace grade Al alloys subjected to flight loading spectra that comprise overloads, underloads and mixed-mode fatigue cycles. It is essential to understand the governing micromechanisms of fatigue crack initiation and propagation under these realistic multiaxial service loads to accurately predict failure life. Crack growth phenomena such as crack retardation and acceleration under variable amplitude and/or mixed-mode loading conditions need to be explored in detail, with the goal of gaining insight into the relationship between loading history and crack growth characteristics such as growth rate, crack profile and fracture surface morphology. Therefore, as part of this thesis, systematic and comprehensive experimental investigations have been performed to characterize the micro- and macroscale multiaxial fatigue behavior under the influence of overloads and underloads of different magnitudes, varying mode-mixities, occurring at different stages of fatigue crack propagation. In addition, the fatigue-fracture micromechanisms that govern crack retardation and acceleration under variable amplitude loads have been identified through quantitative fractography and correlated with macroscopic crack growth.

In the case of FRP composites used in aerospace applications, numerous studies have been conducted to characterize and enhance their fatigue resistance and possibly induce *in-situ* damage-sensing multifunctional properties through the use of nanomaterials. Composite materials offer the unique opportunity for incorporation of high-strength, multifunctional nano-reinforcements such as CNTs, that can alter the material architecture of composites at the nanoscale and potentially improve overall material properties such as strength, fatigue resistance, and thermal and electrical conductivity. Carbon nanotubes also exhibit piezoresistivity, a property that can be potentially exploited to sense deformation and damage in the host FRP materials, through measurement of changes in electrical resistance. Several researchers have attempted to use CNTs as nanofillers in FRPs and have reported significant improvements in mechanical, thermal and electrical properties, although harnessing the real potential of CNT reinforcements at a structural scale remains a challenging task due to the complexities associated with processing and fabrication. *In-situ* strain sensing and damage detection, in addition to improvement in fatigue performance, have been reported for CNT based polymer composites. However, accurate *in-situ* quantification of strain and fatigue damage is still to be accomplished, especially at the structural scale.

In the research work presented in this thesis, an effort has been dedicated to developing a novel CNT-based FRP composite that exhibits improved resistance to fatigue damage and exhibits multifunctional capabilities such as *in-situ* stain and damage quantification. In addition, processing methods have been developed to efficiently fabricate sizable multifunctional composite materials to extend the application of self-sensing CNT based composites to the structural scale. The background of relevant research is discussed in Section 1.2 and Section 1.3.

1.2 Background of Mechanical Fatigue in Metallic Materials

The growth of fatigue cracks in high-strength, aerospace grade Al alloys has been an issue of great importance to the aerospace industry and has been extensively studied by many researchers in the past few decades. Aerospace components are exposed to a wide variety of multiaxial mixed-mode fatigue loading conditions during their service life; therefore, fundamental understanding of fatigue damage accumulation and progression under such loading conditions is essential to predicting their useful life (Carpinteri, Spagnoli, & Vantadori, 2003; Jiang, 2000; Socie, 1987; Sunder & Ilchenko, 2011; You & Lee, 1996; Zenner, Simbürger, & Liu, 2000). Specifically, variable amplitude (VA) loading is one of the most complex loading scenarios experienced by these components and understanding the phenomena which govern the crack growth mechanisms activated under a series of random amplitude loads is a challenging task (Neerukatti, Datta, Chattopadhyay, Iyyer, & Phan, 2016a; Pommier, 2003; Sonsino, 2007; Datta, Chattopadhyay, Iyyer, & Phan, 2018; Datta & Chattopadhyay, 2018). Although a multitude of studies has been reported on the fatigue behavior of metallic materials under uniaxial and/or pure mode-I loading conditions with overloads and underloads (Schijve & Broek, 1962; Zhang et al., 1987), there is very limited understanding of the crack growth behavior under complex multiaxial loading. Uniaxial VA fatigue behavior of Al alloys has been studied over the past decades using load spectra such as TWIST and FALSTAF in addition to spectra with single or periodic overloads and underloads (Colin & Fatemi, 2010; Corbly & Packman, 1973; Lankford & Davidson, 1981; Mikheevskiy & Glinka, 2009; Schweizer, Seifert, Nieweg, Von Hartrott, & Riedel, 2011; Skorupa, 1999; Suresh, 1983; Trebules, Roberts, & Hertzberg, 1973; Ward-Close, Blom, & Ritchie, 1989; Zhao, Zhang, & Jiang, 2008). However, the crack growth behavior under biaxial VA loading conditions remains mostly unexplored.

Lee et al. (Lee, Glinka, Vasudevan, Iyyer, & Phan, 2009) studied the constant and VA uniaxial fatigue behavior of Al 7075-T651 alloy in vacuum, air, and saline environments, using a tension-tension and a tension-compression type load spectrum. Their results showed increased fatigue life (slower crack growth) in the case of tension-tension type spectrum due to the occurrence of overloads; unequal striation spacing was observed as a manifestation of the varying crack growth rate. Schijve et al. (Schijve, Skorupa, Skorupa, Machniewicz, & Gruszczynski, 2004a) reported a fatigue study on Al alloy D16 where VA tests included experiments with single overloads, periodic overloads and underloads and the flight-simulation load history FALSTAFF. An overload ratio of 2 was used in the single overload tests, and delayed crack retardation was reported. The slight delay in crack retardation after overload was attributed to residual stresses and plasticity induced crack closure in the wake of the crack-tip that reduce the effective ΔK. Fractography results correlating striation spacing with macroscopic crack growth rates were also presented, and their direct dependence on the load history was established. In another study, Schijve (1999) studied the uniaxial VA fatigue crack growth behavior of Al 2023-T3 and Al 7075-T6 by using load spectra with periodic overload cycles superimposed on constant amplitude (CA) cycles. Quantitative fractography and macroscopic crack growth measurements showed that the retardation effects became more prominent with an increase in overload ratio and with increase in the number of overloads within an overload block. Overload blocks also acted as marker loads and facilitated microscopic crack growth measurements. In case of high overloads, total crack arrest was observed after the crack-tip propagated about 500 µm into the overload plastic zone (Ranganathan et al., 2011; Schijve, 1999). Of the many proposed mechanisms for crack retardation, residual compressive stresses and plasticity induced crack closure provide a primary basis for justifying the load-interaction effects. Therefore, many existing models for predicting crack growth rates are based on the crack closure concept (Harmain, 2010; Huang, Torgeir, & Cui, 2008; Newman, 1981; Zhao et al., 2008). However, direct experimental evidence for the dominant role of plasticity induced crack closure is limited.

A biaxial fatigue study was conducted by Shanyavskiy (2011); cruciform specimens of Al-based alloys were subjected to CA and VA loading, including sequences of various overloads. The study showed that semi-elliptical fatigue cracks grew faster and striation spacing became larger with increasing biaxiality ratio. Analysis of crack growth rate before and after overload, for various biaxiality and stress ratios, revealed tensile mode-I fractures inside the specimen after an overload and shear lip formation at the specimen surface. Delayed crack retardation was reported, caused by shear stress on the shear lip surface. Significant adverse effect of tensile stress biaxiality on crack growth rate under periodic overloads in a fighter aircraft load spectrum was shown by Liu and Dittmer (1979). This increase in crack growth rate was attributed to the transverse tensile load that reduces the plastic zone size at the crack-tip. Sunder and Ilchenko (2011) studied the biaxial fatigue crack growth behavior in cruciform test coupons using CA loading (both in-phase and out-of-phase) and a modified TWIST load spectrum superimposed with biaxial quasistatic load simulating internal cabin pressure. They found that the crack growth rates were sensitive to load biaxiality under CA as well as spectrum loading. The fracture features were also found to be highly dependent on the load history. However, the crack growth behavior was not directly correlated with the microscale fracture features, and the mechanisms governing crack propagation under the complex loading conditions were not discussed in detail.

In this research work, experimental investigations have been conducted to gain a comprehensive insight into the nature of crack propagation under the influence of random amplitude biaxial fatigue loading by studying the effect of individual overloads and underloads of different magnitudes. The primary goal is to characterize the in-plane biaxial fatigue crack propagation behavior and investigate the underlying microscale mechanisms in Al-7075 T651 test specimens subjected to single overloads or underloads of different magnitudes occurring at different fatigue crack lengths. Detailed quantitative fractography studies were conducted, and the results provide insight into the active micromechanisms that govern crack growth behavior in the event of an abrupt change in biaxial cyclic load. The effects of different overload magnitudes on fatigue crack growth were analyzed and correlated with instantaneous crack length, crack-tip plasticity, and the fracture surface morphology.

In many practical cases with VA multiaxial fatigue loading, the cracks are not normal to the maximum principal stress direction, leading to overloads/underloads that cause mixed-mode (combined modes I and II) stress-states at the crack tip (Qian, & Fatemi, 1996;

Richard, Schramm, & Schirmeisen, 2014). This type of loading can commonly arise when cyclic loads along different axes with respect to the crack are non-proportional or have unequal magnitudes, causing a combination of shear and normal stresses at the crack tip. Another scenario with multiaxial mixed-mode loading can arise due to the occurrence of crack deflection or crack branching during crack growth (Silva, De Jesus, Xavier, Correia, & Fernandes, 2017; Shamsaei, Nima, & Fatemi, 2014). Most importantly, the effects of multiaxial mixed-mode overloads on the micro- and macroscale crack growth are yet to be completely explored.

To study the crack propagation behavior under mixed-mode (mode I+II) and pure mode-II fatigue loads of different magnitudes, several researchers have used Compact Tension Shear (CTS) specimens with a uniaxially loaded Richard's type loading device to induce the mode-mixity (Borrego, Antunes, Costa, & Ferreira 2016; Hashemi, & Taslim, 1986; Dahlin, & Olsson, 2004). Srinivas and Vasudevan studied the influence of mixed-mode (mode I+II) overloads on mode-I fatigue crack growth in D16AT Al alloy using CTS specimens and the aforementioned loading device. It was observed that the degree of retardation decreased with a decrease in stress intensity ratio K_I/K_{II}. It was also reported that retardation periods increased with increase in R_{OL} (Srinivas, &Vasudevan, 1993). Sander and Richard used a similar experimental setup for Al 7075 T651 alloy and conducted experimental investigations on both mixed-mode overloads, which are interspersed into a Mode I baseline level loading, and mixed mode block loadings (Sander & Richard, 2006). The experimental investigations showed that retardation effect decreases with an increasing amount of mode-II in the overload. Due to the block loading, the fatigue crack growth rate is retarded as well, and crack deflection occurred. The kinking angle was found to be a function of fraction of mode-II stresses. Pure mode-II overloads were seen to have negligible effect on the crack growth rate. Borrego et al. reported a mixed-mode (mode-I+II) fatigue study on CTS specimens of AlMgSi1-T6 aluminum alloy for different mode-mixity levels. They showed that crack closure levels were higher in mixed-mode loading condition as compared to pure mode-I loading. For smaller crack lengths, the closure levels due to mixed-mode loading were found to be significantly higher than at higher crack lengths. Such behavior is attributed to the dominance of roughness induced crack closure (Borrego, Antunes, Costa, & Ferreira 2016).

Another more effective and realistic way of studying mixed-mode fatigue under actual biaxial loading (instead of applying uniaxial loading with mixed-mode fixtures such as Richard's loading device) is the use of cruciform geometry specimens with biaxial fatigue frames. Mall et al. and Neerukatti et al. used cruciform specimens for biaxial fatigue tests for their studies on the effects of out-of-phase loading that results in continuously oscillating mode-mixity (mode I+II) at the crack tip (Neerukatti, Datta, Chattopadhyay, Iyyer, & Phan, 2016; Mall & Perel, 2015). Neerukatti et al. observed decrease in crack growth rate as the phase angle between x and y loads was increased from 0˚ to 180˚, where peak level of mode-mixity during a fatigue cycle increased with the applied phase difference. Crack turning was observed for 45˚ and 90˚ phase difference cases and consistently competing mode-I, and II fracture micromechanisms were identified through fracture surface analysis. For 180˚ phase difference, initial crack was observed to split into two cracks due to the dominance of mode-II driving forces, and the cracks grew in directions that maximized K_I. Mall et al. applied out-of-phase loading to a mode-I pre-crack and observed that the crack split into two cracks that grew symmetrically about the pre-crack and the angle of splitting was found to be in close agreement with the Erdogan and Sih relation for maximized hoop stress at the propagating crack-tip (Erdogan & Sih, 1963).

Although a multitude of studies have been published in literature about the effects of mixed-mode fatigue loading, there is lack of experimental evidence identifying and explaining the governing crack growth micromechanisms. The effects of mode-mixity on crack closure levels and crack growth rates have been found to be different for small cracks, as compared to long cracks. However, there are significant discrepancies in the crack growth studies in literature with regard to the role of fatigue crack length. Limited studies have been conducted on understanding the governing mechanisms of crack retardation and acceleration effects in multiaxial mixed-mode loading conditions. Hence, in this thesis, an effort has been made to comprehensively investigate the effects of individual mixed-mode overloads of different magnitudes and mode-mixity on baseline mode-I fatigue crack growth in Al 7075 T6 cruciform specimens under biaxial loading

1.3 Background of Carbon Nanotube-based Polymer Composites

1.3.1 Multifunctional Carbon Nanotube Buckypaper Membranes

Since the discovery of carbon nanotubes (CNTs) by Iijima (1991), CNTs have gained immense popularity in the field of nanocomposites by exhibiting an unprecedented combination of beneficial mechanical, thermal and electrical properties. The use of CNTs as nano-filler in polymer composites has shown considerable improvement in mechanical properties such as tensile and compressive strength, elastic modulus and fatigue resistance in addition to enhanced thermal and electrical properties (Thostenson, Ren & Chou, 2001; Cheng, Bao, Park, Liang, Zhang, and Wang, 2009; Ashrafi, Guan, Mirjalili, Hubert, Simard & Johnston, 2010). Recently, polymer/CNT nanocomposites have received extensive recognition for the versatility they offer in a variety of applications such as water purification, gas sensing, strain sensing, super capacitance, fuel cell electrodes, fire retardant coatings, artificial muscles, EMI shielding and self-heating hybrid composites for de-icing (Dumée, Sears, Schütz et al, 2010; Slobodian, Riha, Lengalova, Svoboda, & Saha, 2011; Benlikaya, Slobodian, & Riha, 2013; Kang, Schulz, Kim, Shanov, & Shi, 2006; Zheng, Qian, Yu, & Wei, 2013; Zhu, Ku, Zheng et al, 2010; Park J.G., Louis, Cheng et al, 2009; Chu, Zhang, Liu, & Leng, 2014; Vohrer, Kolaric, Haque, Roth, & Detlaff-Weglikowska 2004). These applications employ CNTs in the form of a membrane, also known as buckypaper, which is a thin porous membrane of highly entangled CNTs held together by van der Waals forces.

Vacuum filtration is the popular method used by many researchers for manufacturing buckypaper (Dumée, Sears, Schütz et al, 2010; Slobodian, Riha, Lengalova, Svoboda, & Saha, 2011; Benlikaya, Slobodian, & Riha, 2013; Rein et al. 2011; Dharap 2004). This method involves vacuum-assisted filtration of a homogeneously dispersed CNT solution using a Polytetrafluoroethylene (PTFE) or nylon filter with sub-micron sized pores. CNTs are deposited on the filter surface and form a thin membrane (i.e., buckypaper) that can be lifted off the filter surface after drying. Dumee et al. (2010) developed a buckypaper membrane for water purification using the vacuum filtration manufacturing method. This technique has been used for manufacturing buckypaper membranes for use as an embedded strain sensor in epoxy dog-bone specimens by Rein et al. (2011), as a smart skin for strain sensing in aircraft wings by Dharap et al. (2004), and as a de-icing glass fiber reinforced polymer (GFRP) nanocomposites by Chu et al. (2014). The implementation of most of these nascent ideas has been limited to laboratory scale due to the size limitations posed by the current fabrication methods for buckypaper. A more rapid, large-scale manufacturing technique is critical to extend the application of these multifunctional capabilities to the industrial scale.

Vacuum filtration method limits the size of the manufactured buckypaper to the diameter of the filter being used and can also lead to a heterogeneous distribution of CNT bundles in the finished product (Cherng, 2004). Using filters with larger diameters may not completely solve the issue since it would require large volumes of CNT solution to be filtered. Maintaining homogeneous dispersion in a large volume of CNT solution is a challenging task due to the tendency of CNTs to form agglomerates/clusters. Filtering larger quantities of solution through sub-micron filters can take several hours depending on the diameter and pore size of the filter, the volume of solution being filtered, and the pressure difference applied by a vacuum pump. Another disadvantage of this method is the need of surfactants or chemical functionalization of CNTs to assist in obtaining a stable uniform dispersion during filtration (Islam, Rojas, Bergey, Johnson, and Yodh, 2003; Ounnunkad, Minett, Misides et al, 2011). Following filtration, the surfactants can be challenging to remove from the buckypaper and can hamper the efficiency of the membrane for applications such as water purification, gas separation, and biofuel cell electrodes (Rein, Breuer, & Wagner, 2011). Chemical modification of CNTs prior to the filtration can also degrade the functionality of buckypaper for the aforementioned applications (Chih-Yen 2005; Liu, Li, Wang, Gu, Li, & Zhang, 2013; Tasis, Tagmatarchis, Georgakilas, & Prato 2003; Sears, Dumée, Schütz et al, 2010). Another fabrication method for CNT membranes, which is not so commonly used by researchers possibly due to its complexity, is hydro-entanglement developed by Zhang (2008). This method involves impregnation of high-speed water jets on to CNTs present on a porous substrate. The CNTs get highly entangled due to the high pressure of water jets but this process requires high power consumption, and it has a complex set up, limiting its capability to smaller size membranes. A method for manufacturing continuous strips of buckypaper was developed by Young (2009) using a continuous 1.5” wide filter made of ABS plastic. The method shows good potential for manufacturing continuous buckypaper strips. However, the design complexities of the vacuum filtration system used in this method lead to longer processing time and fabrication of wider continuous buckypaper membranes could be a challenging task. Recently, a slurry-based fabrication process, with a few similarities to the proposed method in this paper, was developed by Veliky (2014). The method utilized CNT/paraffin wax slurry produced through sonication to form molds from which paraffin wax could be extracted. Vacuum bagging method was used to obtain thin CNT membranes by pushing out the paraffin wax, and thin membranes could be obtained. Nevertheless, CNT membranes did not have a completely smooth surface finish, and larger CNT membranes would require bigger vacuum bagging setups and higher power consumption. Hence, in this dissertation, an effort has been made to develop feasible processing methods for larger buckypapers with the aim of embedding them in FRPs. The microstructure and properties have been characterized to validate the suitability of the buckypapers for polymer infusion and embedment in composite materials.

1.3.2 Carbon Nanotube Embedded Fiber Reinforced Polymers

Fiber reinforced polymer (FRP) composites are extensively used in aerospace and automotive industry mainly due to their high specific strength, reasonable fatigue life, and low cost. However, monitoring damage in composites using real-time sensors or non-destructive evaluation techniques is a challenging task due to their complex and heterogeneous microstructure. Recently, the aerospace industry has focused its research on developing multifunctional composites with superior mechanical properties and self-sensing capabilities that enable the composite to autonomously sense deformation and damage in real-time. The self-sensing capability is an important feature that can reduce maintenance and inspection time while increasing the safety of aerospace structures (Balageas, Fritzen, & Güemes, 2010; Giurgiutiu, Zagrai, & Jing Bao, 2002). Many recent studies have focused on employing the piezoresistive property of CNTs for structural health monitoring (SHM) in composite structures. The advantage of piezoresistive based sensing is that it does not require expensive equipment for instrumentation or the placement of discrete sensors that can compromise structural strength or performance. When added as a nanofiller in FRPs, CNTs form a conductive percolation network, thereby rendering the structure conductive. Owing to the conductive and piezoresistive nature of CNTs and their percolation networks, many researchers have demonstrated electrical resistance based SHM of such composite structures (Alexopoulos, Bartholome, Poulin, & Marioli-Riga, 2010; Böger, Wichmann, Meyer, & Schulte, 2008; Dharap, Li, Nagarajaiah, & Barrera, 2004; Kang, Schulz, Kim, Shanov, & Shi, 2006; Rai, Subramanian, & Chattopadhyay, 2016; Yu & Kwon, 2009).

Alexopoulos et al. developed a CNT based polyvinyl alcohol fiber which, when embedded in GFRPs, enabled real-time strain and damage monitoring of the GFRP under static and cyclic load (Alexopoulos et al, 2010). Kim et al. demonstrated damage detection in 3D braided composites using dispersed CNTs in the polymer matrix and measuring the electrical resistance change of the composite as the composite was loaded (Kim et al., 2010). Vertuccio et al. investigated the strain and damage sensing capability of CNT embedded resins under static and cyclic strain (Vertuccio, Vittoria, Guadagno, & De Santis, 2015). They showed that the strain sensitivity of CNT based composites could be controlled by varying the weight fraction of CNT nanofiller in the host structure.

Rein et al. explored the effects of a wide range of strains on the electrical response of BP embedded in different types of polymers (Rein, Breuer, & Wagner, 2011). They reported observing high strain-sensitivity of BP even at strains as high as 30%. The electromechanical response of the BP sensors used in their study was also found to be influenced by local defects and geometry. Zhang et al. embedded BP in glass fiber laminates for strain and damage sensing through electrical resistance measurements and analyzed BP sensitivity in different strain ranges (Z. Zhang, Wei, Liu, & Leng, 2015). Buckypaper was embedded in bonded joints in a study by Rai et al. and real-time strain monitoring was done using the piezoresistive response during pull off tests (Rai, Datta, Chattopadhyay, & Lopez, 2017). However, most of these studies found in the literature provide a qualitative measure of damage in the material based on residual resistance increment. Also, there has been little effort done to correlate residual resistance increments to quantitatively express damage in such composites. Thus, a novel method for real-time fatigue crack length quantification in a new type of BP embedded GFRP composite has been presented in Chapter 3.

In this dissertation, CNT BPs manufactured using the novel fabrication process have been used to successfully induce multifunctional capabilities, such as strain sensing, damage quantification, and improved fatigue resistance, in GFRP laminates. The capability of this BP manufacturing process to rapidly manufacture sizable membranes is demonstrated and its potential to advance CNT membrane-based composites to structural scale applications is realized through the development of self-sensing GFRPs (SGFRPs) with superior resistance to fatigue crack growth. The ability to autonomously sense and quantify strain and damage in real time has been demonstrated through in-situ resistance measurements during fatigue loading.

1.4 Objectives of the Work

The overreaching goal of the present work is to obtain a comprehensive understanding of fatigue damage evolution in an aerospace grade Al alloy under biaxial loading conditions. In addition, research has been conducted to develop a multifunctional composite with improved fatigue resistance and *in-situ* damage quantification capability. The following are the principal objectives of this work:

1.4.1 Fatigue Crack Growth Behavior of Al 7075 under Complex Biaxial Loading

- Study in-plane biaxial fatigue crack growth behavior in Al 7075 aerospace grade alloy under variable amplitude loading (VAL) conditions. Investigate the underlying microscale fracture mechanisms that govern fatigue crack growth under biaxial VAL conditions and develop numerical models to predict crack growth and fatigue life.
- Investigate the influence of individual overloads and underloads with biaxiality ratio (BR) of 1 (pure mode-I) on the micro- and macroscale fatigue crack growth behavior of Al 7075 alloy. Analyze the effect of overload magnitude and fatigue crack length at the time of overload, on crack retardation behavior and identify the governing micromechanisms through quantitative fractography. Develop phenomenological numerical models to predict crack retardation and fatigue life under the influence of overloads of different magnitudes.
- Study the effects of overloads of different magnitudes with BR of 0.5 and 0.75 (mixed-mode) on crack retardation behavior of Al 7075 alloy. Analyze the crack growth and micromechanisms resulting from mixed-mode overloads for short and long fatigue cracks. Identify the contributions of different crack closure mechanisms to crack retardation for different mode-mixity overloads occurring at different crack lengths.

1.4.2 Carbon Nanotube-based Multifunctional Composites

- Develop efficient fabrication methods for CNT membranes (buckypapers) which can be embedded in the interlaminar regions of FRPs. Rapid production of larger sized CNT membranes is essential for extending their multifunctional attributes to structural scale applications.

- Investigate the microstructural characteristics and electrical properties of buckypapers fabricated from the novel slurry compression method. Characterize the pore-size distribution and specific surface area (SSA) of buckypaper to assess its suitability for use in polymer matrix composites.
- Develop multifunctional self-sensing composites using buckypaper by exploiting the electrical and piezoresistive properties. Embedding buckypaper into fiber reinforced polymer composites to enable in-situ strain sensing and fatigue damage quantification based on electrical conductivity signals.

1.5 Outline

This dissertation is structured as follows:

Chapter 2 presents the detailed investigation on biaxial fatigue crack growth behavior of Al 7075 aerospace grade alloy under pure mode-I (BR=1) VAL conditions. Specifically, the effects of individual overloads and underloads of different magnitudes on micro- and macroscale crack growth behavior have been analyzed and correlated to fracture surface morphology and crack growth rates. Different micromechanisms responsible for crack retardation in case overloads, and crack acceleration in case of underloads, have been identified using scanning electron microscopy (SEM). Furthermore, studies have been presented on the load interaction effects between CA fatigue cycles, overloads, and underloads, to better understand variable amplitude biaxial fatigue crack growth behavior in Al 7075 alloy. Using the experimental data, a numerical formulation is developed for a phenomenological model to predict crack retardation behavior, and fatigue life under VA biaxial fatigue loading. Parameters such as overload magnitude, instantaneous crack length and stress intensity factor are used to predict crack growth rates in the event of overloads and the corresponding fatigue life is estimated.

Chapter 3 discusses the crack growth characteristics, and fatigue-fracture micromechanisms in case of mixed-mode (mode I+II) overloads having BR of 0.5 and 0.75. The contributions of different crack closure mechanisms such as mode-I plasticity-induced crack closure, crack blunting and roughness induced crack closure were identified through detailed fractography and correlated to the micro- and macroscale crack growth behavior. The role of instantaneous crack length, overload mode-mixity and overload ratio in governing the crack-tip behavior is investigated in detail through extensive fatigue testing.

Chapter 4 introduces the novel rapid fabrication method for sizable buckypapers and presents the microstructural and electrical characterization results for the as-fabricated buckypapers. The properties are then compared with properties of buckypapers fabricated using conventional fabrication methods published in literature. The porosity of buckypapers is analyzed, and their suitability for embedding in fiber reinforced polymer composites is evaluated. Buckypaper/epoxy films were fabricated, and the quality of resin impregnation and their mechanical properties are presented.

The applications of buckypaper in composite laminates as a smart layer are presented in Chapter 5. Self-sensing glass fiber laminates with embedded buckypaper were developed and tested under static and fatigue loading conditions. Their piezoresistive response was used to sense strain under static and cyclic loading. A measurement model for in-situ quantification of fatigue damage is also presented. Good correlation between sensed crack length and actual crack length have been demonstrated and the fatigue life improvement achieved due to embedding buckypaper has been highlighted.

Chapter 6 discusses the contributions made through the research efforts conducted as a part of this dissertation. The potential research directions and future work is also discussed, with ideas to extend this work to additional meaningful applications.

2 VARIABLE AMPLITUDE MODE-I BIAXIAL FATIGUE CRACK GROWTH IN AL 7075 T651 ALLOY

2.1 Introduction

Metallic aerospace structures are subjected to complex biaxial fatigue loading during their service lives, and the loading spectra often consist of variable amplitude (VA) loads in the form of overloads and underloads. The overloads and underloads are known to cause crack acceleration and deceleration behavior, respectively, and directly affect the failure life of structural components. Therefore, understanding the crack growth behavior and the corresponding governing micromechanisms that get activated in the event of overloads/underloads in aerospace grade alloys is critical to predict the residual useful life (RUL) of structures. Often, the service life VA loading conditions comprise a series of overloads and underloads of different magnitudes, that may occur at different instantaneous fatigue crack lengths. The effects of overloads/underloads of varying magnitudes, occurring at different crack lengths can be significantly different, and the crack acceleration/deceleration characteristics and fatigue-fracture micromechanisms become highly complex. Hence, understanding the influence of loading history and the interaction of overloads/underloads, on micro- and macroscale crack growth behavior becomes a challenging task.

There has been considerable research done towards the investigation of uniaxial fatigue crack growth behavior under the influence of overloads and underloads, however to the best of author’s knowledge, there have no studies in literature on biaxial fatigue behavior with overloads/underloads. Moreover, many crack retardation and acceleration mechanisms have been proposed in literature, nevertheless there is lack of experimental evidence and in some studies, significant discrepancies exist in the crack growth behaviors observed at different length scales. Hence, as part this thesis, a comprehensive experimental study has been conducted to exclusively investigate the effects of individual overloads and underloads of different magnitudes on micro- and macroscale crack growth characteristics. In addition, the crack retardation and acceleration micromechanisms have been identified through quantitative fractography using scanning electron microscopy (SEM), and their dependence on instantaneous fatigue crack length has been discussed.

To investigate the effects of overloads of different magnitudes, load spectra were carefully designed such that a single overload of certain R_{OL} was inserted in a baseline mode-I constant amplitude (CA) load spectrum. The fatigue crack growth rates were monitored through a high-resolution camera, and the crack retardation behavior was studied for R_{OL} of 1.75, 2.0 and 2.25. The effect of fatigue crack length on retardation behavior was also investigated, and different retardation micromechanisms were observed for small versus long cracks. Quantitative fractography was performed to identify the fatigue-fracture mechanisms that get activated post-overload by examining the fracture surface morphology in the overload affected zone ahead of the crack-tip, where the slowed crack growth was observed. Furthermore, biaxial fatigue tests with single underloads and combination of single overload and underload were conducted to analyze the crack acceleration caused by an underload and study the interaction of an underload with overload.

2.2 Materials and Experimental Methods

2.2.1 Biaxial Fatigue Test Setup

Experiments were conducted using the MTS planar biaxial/torsion load frame with a dynamic load capacity of 100kN in both horizontal and vertical directions, shown in Figure 2.1. The testframe is equipped with six independent controllers; this allows testing under a wide range of biaxial loading conditions, including in-phase, out-of-phase, proportional and non-proportional loading. Specimen design is critical to accurate estimation of fatigue life.

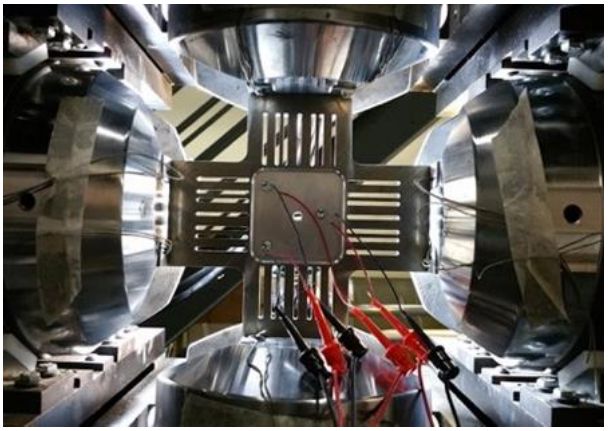

Figure 2.1: Cruciform specimen in biaxial fatigue frame

The cruciform specimen, shown in Figure 16, was designed such that the central web area had uniform stress distribution for initial yielding. The specimens were machined from 6.35mm rolled Al7075-T651 sheets with the thickness of web area at 1.8mm. A hole of diameter 6.35mm was cut at the center of the web area and a notch of length 1.5mm and width 0.36mm was made at an angle of 45˚ (Figure 2.2) to facilitate crack initiation. The presence of the notch at 45˚ angle facilitates the calculation of mode-I stress intensity factor

(SIF) at the crack tip when the crack initiates and propagates under the applied biaxial fatigue loading. In the absence of this notch, the cracks could initiate at any arbitrary orientation from the periphery of the center hole and the resulting test data would not provide meaningful information. Mall and Perel (2015) used a similar notch design at the center hole of a cruciform specimen to facilitate their study on the effect of out-of-phase loading that causes mode mixity in cruciform specimens. A high-resolution camera was positioned on the rear side of the specimen to capture the crack initiation and growth. The camera was programmed using LabVIEW to take images at user-defined time intervals. This allowed calculation of the cycles for crack initiation, propagation and final failure.

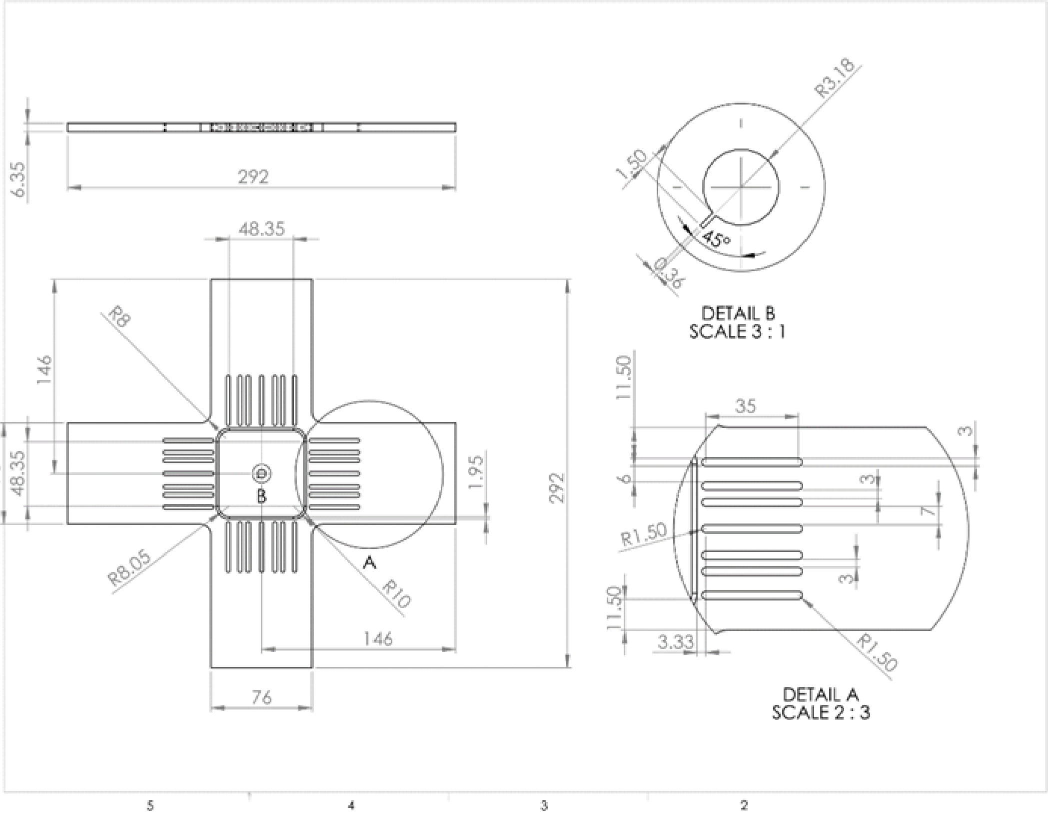

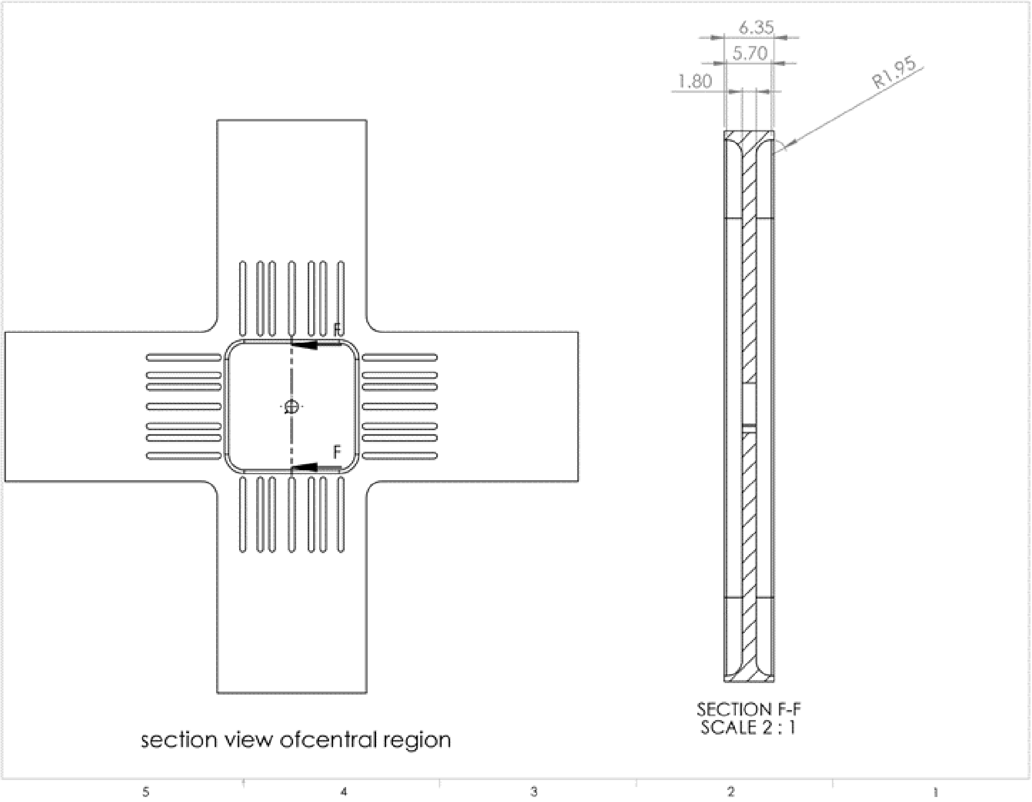

Figure 2.2: Cruciform specimen sketch with dimensions

2.2.2 Biaxial Testing Conditions with Single Overloads (BR_{OL}=1)

To study the effects of a single overload on biaxial fatigue crack propagation, fatigue load spectrums were generated with single overload excursions in an otherwise CA loading with P_{max} = 15kN, R = 0.1 and a frequency of 10Hz. For the tests with single overloads, overload ratios (R_{OL}=P_{OL}/P_{max}) of 1.75, 2 and 2.25 were used in order to investigate the effect of overload magnitude on fatigue crack growth behavior at different crack lengths (a_{OL}) as detailed in Table 2.1.

Table 2.1: Overload tests conducted with R_{OL} of 1.75, 2 and 2.25 occurring at different crack lengths (a_{OL})

Test ID	**R-ratio**	**P_{max}(kN)**	**P_{OL}(kN)**	**R_{OL} (P_{OL}/P_{max})**	**a_{OL}(mm)**	**N_{OL}(cycle)**
OL_T1	0.1	15	26.25	**1.75**	**3.76**	30,000
OL_T1	0.1	15	26.25	**1.75**	**15.99**	65,000
OL_T3	0.1	15	26.25	**1.75**	**9.16**	25,000
OL_T7	0.1	15	26.25	**1.75**	**2.1**	25,000
OL_T7	0.1	15	26.25	**1.75**	**4.75**	45,000
OL_T10	0.1	15	30	**2.00**	**6.77**	30,000
OL_T11	0.1	15	30	**2.00**	**9.33**	30,000
OL_T4	0.1	15	33.75	**2.25**	**4.9**	25,000
OL_T4	0.1	15	33.75	**2.25**	**6**	45,000
OL_T4	0.1	15	33.75	**2.25**	**11.18**	126,000
OL_T12	0.1	15	33.75	**2.25**	**3**	30,000
OL_T12	0.1	15	33.75	**2.25**	**10.73**	80,000
OL_T12	0.1	15	33.75	**2.25**	**27.45**	140,000

2.2.3 Biaxial Testing with Underloads and Overload/Underload Combinations

For the tests with single underloads, underload ratio (R_{UL}=P_{UL}/P_{max}) of -0.5 was used in order to investigate the effect of underloads on fatigue crack growth behavior at different crack lengths (a_{UL}) as detailed in Table 2.2.

Table 2.2: Underload tests with R_{UL} of -0.5 occurring at different crack lengths (a_{UL})

Test ID	R-ratio	P_{max}(kN)	P_{UL}(kN)	R_{OL} (P_{OL}/ P_{max})	a_{UL}(mm)	N_{UL}(cycle)
UL_T1	0.1	15	- 7.5	-0.5	7.8	30,000
UL_T2	0.1	20	-10	-0.5	15.9	65,000

To study the interaction of crack growth mechanisms between overloads and underloads of different magnitudes, biaxial fatigue load spectra were generated with single overload immediately followed by an underload in an otherwise constant amplitude spectrum of 1.5-15 kN fatigue cycles. Crack propagation behavior was investigated under the combination of single overload of R_{OL} = 1.75 and underload of R_{UL} = -0.5 for small and large fatigue cracks, and the test parameters are presented in Table 2.3.

Table 2.3: Fatigue tests with combination of overload and underload

Test ID	R-ratio	P_{max}(kN)	P_{OL}(kN)	P_{UL}(kN)	R_{OL} (P_{OL}/ P_{max})	R_{UL} (P_{UL}/ P_{max})	a_{cmb}(mm)	N_{cmb}(cycle)
OL_T13	0.1	15	26.25	-7.5	1.75	-0.5	5.37	30,000
OL_T14	0.1	15	26.25	-7.5	1.75	-0.5	13.31	50,000
OL_T15	0.1	15	26.25	-7.5	1.75	-0.5	4.21	30,000
OL_T16	0.1	15	26.25	-7.5	1.75	-0.5	11.40	50,000

2.2.4 Quantitative Fractography for Crack Retardation Micromechanisms

Following the fatigue tests, quantitative fractography was performed on the fatigued specimens using SEM. The microstructural crack growth features obtained were correlated to the load history, crack growth rate and crack-tip plasticity. Fracture features corresponding to overloads of different magnitudes were identified and their influence on crack growth rate was investigated. Specifically, the transient region, which is the overload affected region where crack retardation is observed, was scanned for fracture modes known to resist crack propagation. Although, micromechanisms such as crack-tip blunting due to plasticity, roughness induced crack closure due to mode-mixity, crack deflection and crack-tip splitting have been reported to reduce crack growth rate, it is crucial to determine their individual contributions with respect to different overload magnitudes and instantaneous crack length. Fracture surfaces were cut out from the fatigued cruciform specimens using a low-speed diamond saw, and then sonicated in acetone to remove debris and the cutting fluid. Cleaned fracture surfaces were dried using compressed air and then mounted onto metallic stubs for SEM analysis.

2.2.4 Crack-tip Plasticity (Analytical)

To evaluate Stress Intensity Factor (K) for the fatigue crack, a quasi-static finite-element simulation of the three-dimensional cruciform geometry was conducted using ABAQUS/Standard (ABAQUS v6.10). The direction of crack propagation was considered as the normal to the crack front plane. The finite element model along with the mesh is shown in Figure 2.3. A fine mesh was created in the crack tip region to ensure accurate contour integral calculations using 10 contours. Displacement boundary conditions were applied to restrict out-of-plane motion of the cruciform specimen. Surface traction boundary conditions were applied along the ends of cruciform arms to simulate the applied tensile loading. The cruciform model was meshed using tetrahedron elements and a total of 73,313 elements were generated to achieve convergence. Since the fatigue tests were conducted with a biaxiality ratio (BR) of 1, the fatigue crack in all the tests grew along the 45° notch, resulting in pure mode-I crack growth, hence the value of KII and KIII were found to be negligible and were not considered for crack-tip plastic zone size calculations. The cyclic loads (1.5-15 kN) used in this study were well within the elastic regime, as observed from quasistatic biaxial tensile tests performed in previous work by Neerukatti and Datta et al. (2017). Therefore, plasticity was assumed to be confined to a small region around the crack-tip and linear elastic fracture mechanics approach was adopted.

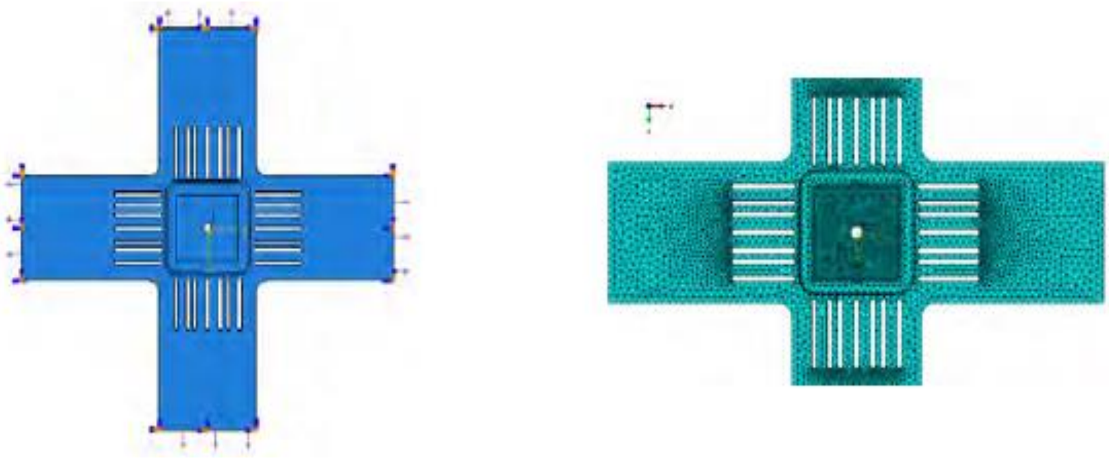

Figure 2.3: Finite element model and mesh for evaluating K_I

To better understand the micromechanisms governing the noticeable changes in fatigue crack growth rates due to overloads and underloads, plastic zone size for different crack lengths was calculated using Irwin’s model. The plastic zone diameter under cyclic loading is calculated using equation (2.1) as,

$$r_{p,CA} = \frac{1}{\beta\pi}\left(\frac{\Delta K_i}{2\sigma_y}\right)^2 \tag{2.1}$$

and the monotonic overload plastic zone size is calculated using equation (2.2) as,

$$r_{p,OL} = \frac{1}{\beta\pi}\left(\frac{K_{OL}}{\sigma_y}\right)^2 \tag{2.2}$$

In equations (2.1) and (2.2), β = 1 and 3 for plane stress and plane strain conditions, respectively. ΔK_i is stress intensity factor range under CA loading for a fatigue crack length a_i at the i^{th} fatigue cycle. σ_y is the yield stress of the material (420.3 MPa for Al 7075-T651) and β = 1 since the web area is 1.8 mm thick, resulting in plane stress condition.

2.3 Results and Discussions

2.3.1 Overload Ratios of 1.75 and 2.0

The load spectrum used for specimen OL_T1, is shown in Figure 2.4. Single overloads with R_{OL}=1.75 were inserted in the load spectrum after 30,000 and 65,000 CA fatigue cycles. The crack length as a function of fatigue cycles for specimen OL_T1 is shown in Figure 2.5a along with crack growth from a CA test for comparison; it can be observed that on application of an overload, the crack growth undergoes significant retardation. At the first overload at 30,000 cycles, when the crack length is 3.77 mm, an immediate and drastic reduction in the crack growth rate (da/dN) was observed as shown in Figures 2.5a and 2.5b. When the second overload was applied, at 65,000 cycles and at a crack length of 16.3 mm, the crack growth rate drops drastically, but not immediately, unlike when overload was applied at a smaller crack length of 3.77 mm. It can be seen from Figure 2.5b, when overload occurs at 65,000 cycles (16.3 mm crack), the crack growth rate remains approximately the same up to a crack increment of 0.4 mm before getting severely decelerated. This phenomenon of delayed retardation has been reported by several researchers and is seen to occur at relatively larger crack lengths, as observed in the experimental results of this paper. Following this decrease, the crack growth rate gradually increased in small increments before resuming a behavior similar to the one observed before the overload. Immediately after the first overload, at crack length of 3.77 mm, the crack grew at significantly slower growth rates for another 0.39 mm, before the crack growth rate recovered and became comparable to the rate before the overload. After the second overload, at crack length of 16.3 mm, the retarded crack growth was observed for 0.66 mm crack increment, before the crack growth rate recovered completely.

An important term introduced here is Rd, known as the recovery distance. This is the length of the transient region formed ahead of the crack-tip at overload. Rd can also be defined as the distance travelled by the crack-tip after an overload until the crack retardation effects wear off and the crack growth rates resume normal growth values. Hence, for OL_T1, the Rd values after overload of R_{OL}=1.75 were 0.39 mm (390 µm) at a crack length of 3.77 mm and 0.66 mm (660 µm) at a crack length of 16.3 mm.

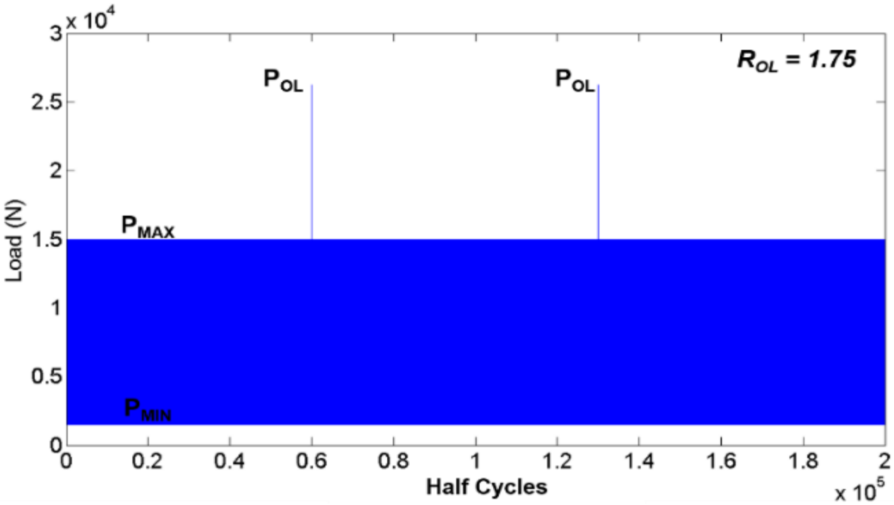

Figure 2.4: Load Spectrum with single overloads of R_{OL} = 1.75 at 30,000 and 65,000 cycles

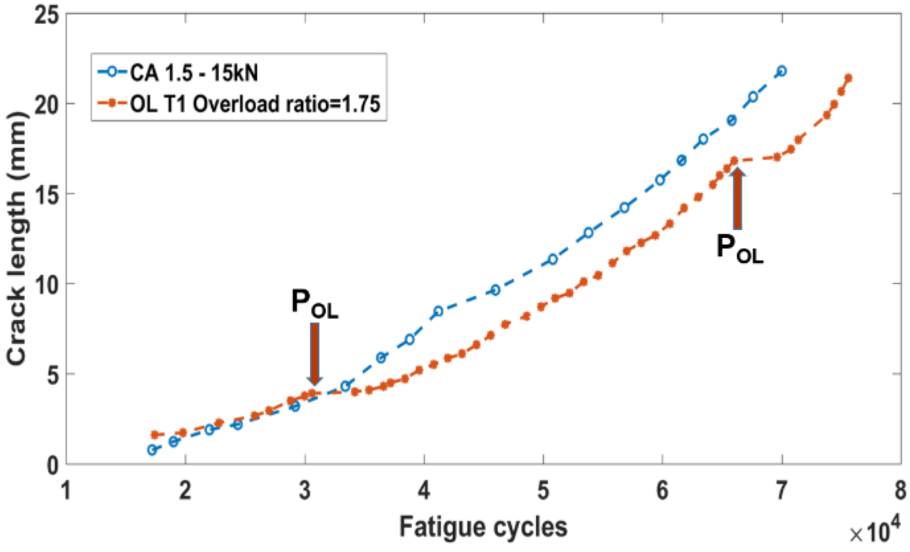

(a)

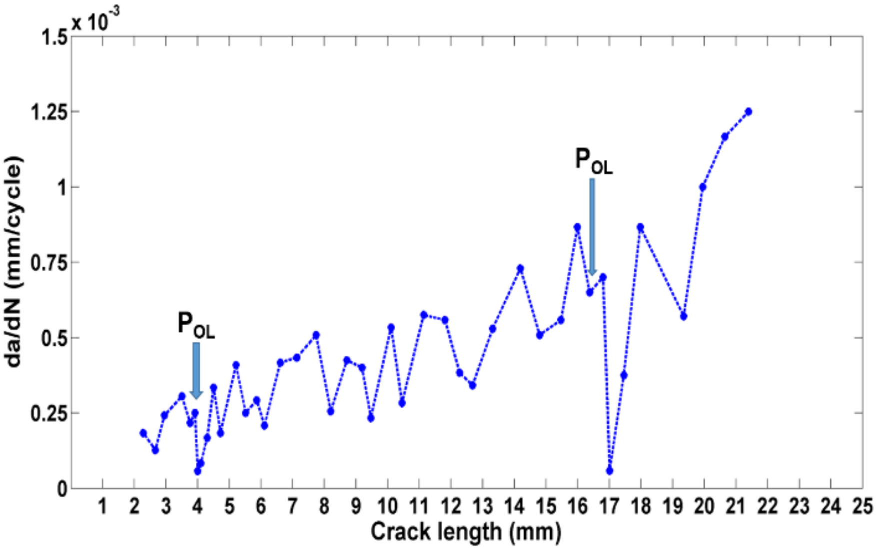

(b)

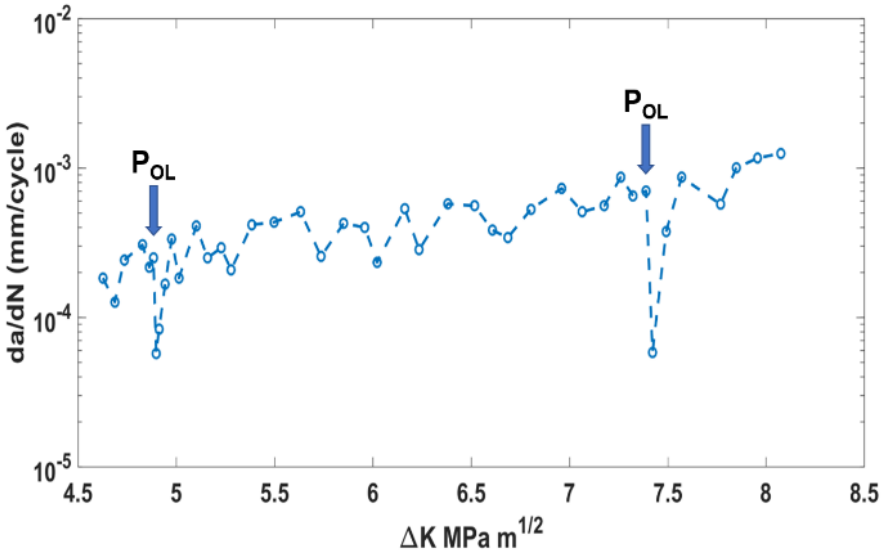

(c)

Figure 2.5: Specimen OL_T1 (a) Crack length as a function of fatigue cycles; (b) crack growth rate as a function of crack length; (c) crack growth rate as a function of ΔK

Table 2.4 highlights the results of fatigue tests conducted with single overloads of R_{OL}=1.75, and the data is presented in the increasing order of crack length (a_{OL}) at which the overload occurred. It can be seen that although the cyclic plastic zone size ($r_{p,CA}$) at the crack-tip (calculated using equation (1)) increased with increasing crack length, it remained in the range of 10-25 µm which is comparable to the width of the rolled grains in Al 7075 alloy. This implies that the plasticity induced crack closure effects on crack growth are not as significant during the CA part of the loading since crack-tip plasticity is confined to a smaller region compared to the crack length (a_i). When a single overload of R_{OL}=1.75 occurs, it causes a monotonic overload plastic zone ($r_{p,OL}$) to form around the crack-tip, the size of which is calculated using equation (2) and is directly proportional to the crack length at overload (a_{OL}). For tests conducted with R_{OL}=1.75, $r_{p,OL}$ was calculated to be in the range of 153.67-359.8 µm for a_{OL} ranging from 2.1 to 16.3 mm. Many researchers have reported their observations on fatigue crack retardation effects due to single overloads in uniaxial fatigue specimens. In the work done by Zhao et al (2008), on effects of single overloads on uniaxial fatigue behavior of Al 7075, the transient region was found to be equal to, or less than, the monotonic overload plastic zone size formed due to the overload. However, under biaxial loading, the size of the transient region (R_d) was found to be greater than $r_{p,OL}$ by a factor of 2 - 3, as shown in Table 2.4. R_d was found to increase with a_{OL}, and the retardation effects were more prominent at larger values of $a_{OL.}$ This observation can be attributed to the larger plastic zone formed when overload occurs at a larger crack length. Since overload causes substantial increment in the plastic zone size around the crack-tip, plasticity induced crack closure in the form of crack-tip blunting and residual compressive stresses becomes dominant and results in the noteworthy decrease in crack growth rate. This crack-tip blunting phenomenon due to sudden overload was also confirmed by fractography and the SEM micrographs of overload affected regions at a_{OL} of 3.77 mm and 16.3 mm, as shown in Figure 2.6, where the yellow arrow marks the direction of crack propagation.

Table 2.4: Fatigue tests with R_{OL} = 1.75

Spec. ID	**a_{OL}(mm)**	**ΔK (MPa√m)**	**K_{OL} (MPa√m)**	**$r_{p,CA}$ (µm)**	**$r_{p,OL}$ (µm)**	**R_d (µm)**	$\left(\frac{da}{dN}\right)_{CA}$	$\left(\frac{da}{dN}\right)_{OL}$
OL_T7	2.1	4.74	9.22	10.16	153.67	360	2.67×10^{-4}	1.84×10^{-5}
OL_T1	3.77	4.86	9.455	10.67	161.41	390	2.5×10^{-4}	5.7×10^{-5}
OL_T7	4.75	5.31	10.32	12.72	192.40	600	3.3×10^{-4}	3.77×10^{-5}

OL_T3	9.16	6.31	12.27	17.97	271.84	620	$5.5x10^{-4}$	$1.4 x10^{-4}$
OL_T1	16.3	7.26	14.11	23.8	359.8	660	$8.67x10^{-4}$	$5.83x10^{-5}$

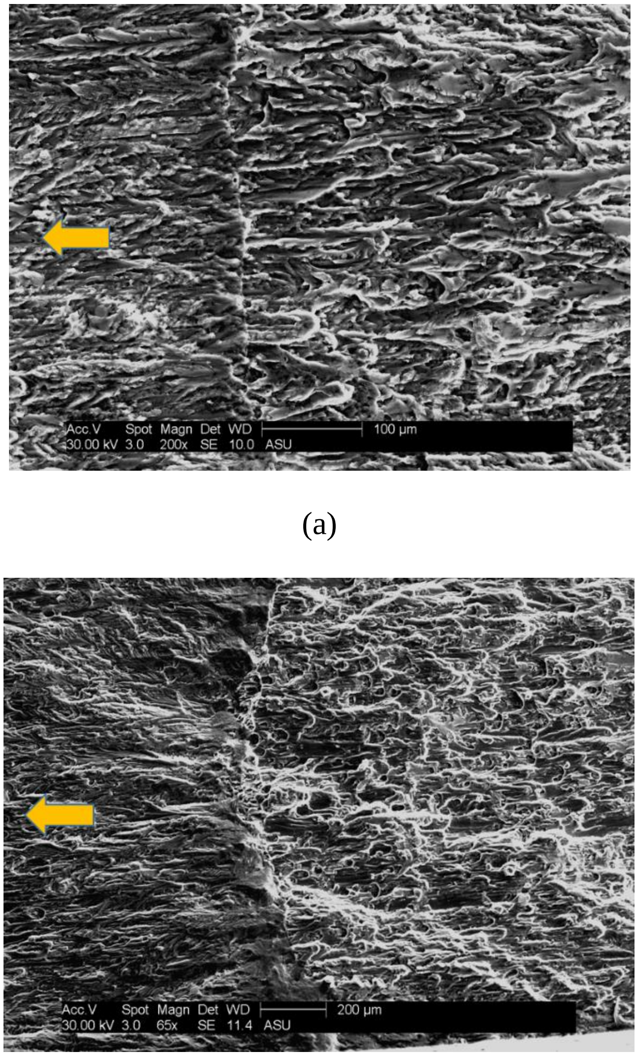

(a)

(b)

Figure 2.6: Overload lines formed on the fracture surface of OL_T1 due to: (a) first overload at 3.77 mm crack (b) second overload at 16.3 mm crack

It can be observed from Figure 2.6, that there is a noticeable difference in the overload line formed at the two different crack lengths. The overload line formed at a smaller crack length of 3.77 mm (Figure 2.6a) was relatively finer and had lesser height than the one formed at a larger crack length of 16.3 mm (Figure 2.6b). There is no noticeable difference in the fracture features before and after the occurrence of the first overload; however, after the second overload the fracture surface becomes highly torturous which indicates a much slower crack growth. In Figure 2.6b, slight dimple formation can be seen along the overload line formed at the second overload indicating high ΔK that arises due to the overload occurring at a larger crack length. From Figures 2.6a and 2.6b, it can be summarized that crack-tip blunting due to plasticity induced crack closure is more pronounced when the overload occurs at a larger crack length, resulting in a larger R_d and prolonged retardation effects. Fatigue striations on the fracture surface, immediately before and after the first overload, are shown in Figures 2.7a and 2.7b, respectively. It can be observed that the spacing between the striations decreases noticeably after the occurrence of the first overload, indicating significant decrease in crack growth rate.

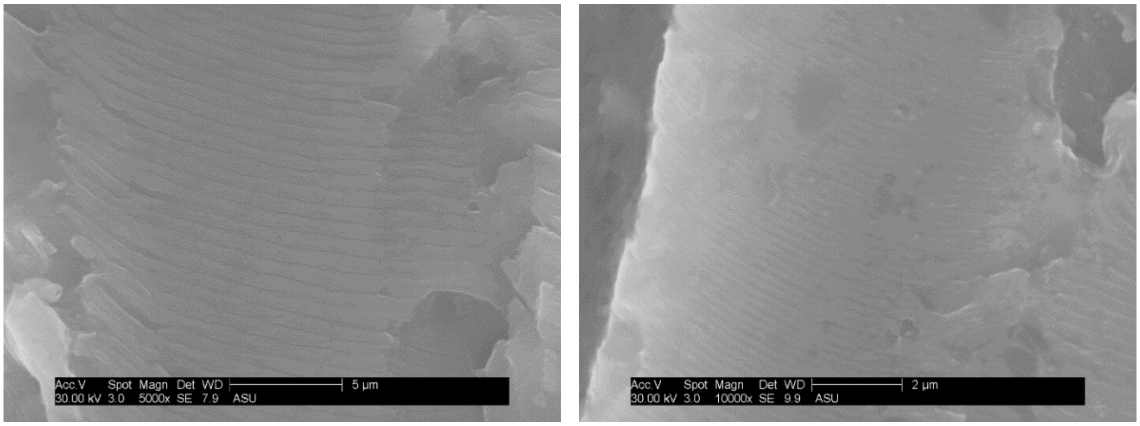

(a) (b)

Figure 2.7: Fatigue striations formed on the fracture surface for OL_T1: (a) before first overload (b) after first overload

The average striation spacing immediately before the first overload was found to be 0.71 μm. The corresponding values, obtained at increasing crack increments after the first overload line on the fracture surface, are presented in Table 2.5. Immediately after the first overload, the striation spacing was reduced by a factor of 9; however, the crack growth rate reduced by a factor of 3.85. For the second overload that occurred at 16.3 mm crack length, the average striation spacing just before the overload occurred was found to be 0.63 μm. The striation spacing dropped to 0.13 μm immediately after the second overload. Hence the average striation spacing was reduced by a factor of 4.84, whereas the crack growth reduced by a factor of 14.82 in the case of the second overload. It can be noted that reduction in striation spacing is much more evident when overload occurs at a smaller crack length, however the reduction in crack growth rate is more severe when overload occurs at a larger crack length and the R_d is significantly larger (see Table 2.4).

Table 2.5: Average striation spacing after first overload

Crack increment after 1st overload (mm)	**Average striation spacing (μm)**
0.07	0.08
0.30	0.14
0.60	0.17

1.00	0.27
1.30	0.34
1.50	0.54

Some noteworthy differences in fracture features before and after the second overload can be observed from Figure 2.8a. A higher magnification SEM image (Figure 2.8b) of the region immediately after the overload line shows signs of mixed mode fracture, with abrasion and sliding marks along the direction of crack growth indicating the presence of mode-II crack driving forces. Since plasticity induced crack closure is much higher at the second overload due to a larger overload plastic zone, this causes pronounced crack-tip blunting, resulting in deflection of the crack-tip at the microscale. As the crack-tip is deflected, mode-II crack driving forces occur, leading to sliding of the crack flanks in the near crack-tip region that manifests itself in the form of wear/abrasion marks along the direction of the crack propagation.

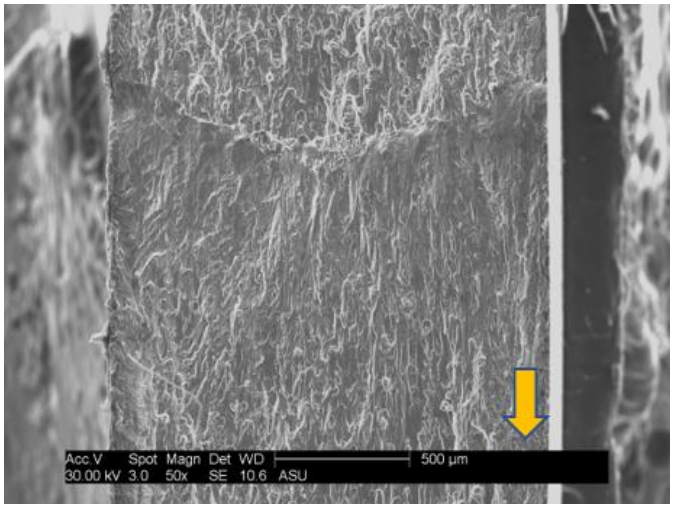

(a)

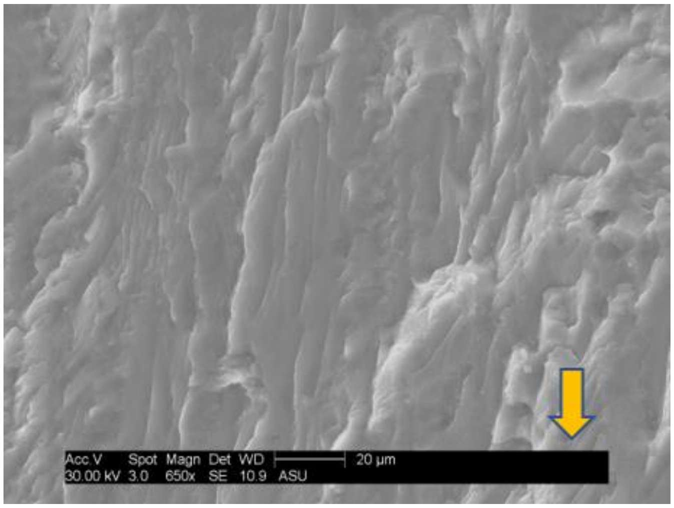

(b)

Figure 2.8: (a) Low magnification image of overload line in OL_T1 due to second overload (b) abrasion marks on fracture surface after second overload

The results for tests conducted with single overloads of R_{OL}=2.0 are summarized in Table 2.6, in the order of increasing a_{OL}. It can be noted from Table 2.6 that the size of the experimentally observed transient region (R_d) is significantly larger than was observed in the case of R_{OL}=1.75 for similar a_{OL} values. The crack growth rates as function of crack length for specimens OL_T10 and OL_T11 are shown in Figure 2.9. The retardation trends following the overload excursions were found to be similar to specimens tested with R_{OL}=1.75; however, the retardation effects were observed to last longer in the case of R_{OL}=2.0, even for comparable plastic zone sizes (see Table 2.4 and 2.6).

Table 2.6: Overload Ratio 2.0

Spec. ID	a_{OL}(mm)	ΔK (MPa√m)	K_{OL} (MPa√m)	$r_{p,CA}$ (μm)	$r_{p,OL}$ (μm)	R_d (μm)	$\left(\frac{da}{dN}\right)_{CA}$	$\left(\frac{da}{dN}\right)_{OL}$
OL_T10	6.77	5.75	12.78	14.94	295.1	810	$5.78\text{x}10^{-4}$	$4.23\text{x}10^{-5}$
OL_T11	9.33	6.31	14.02	17.97	355.06	900	$5.83\text{x}10^{-4}$	$3.6\text{x}10^{-5}$

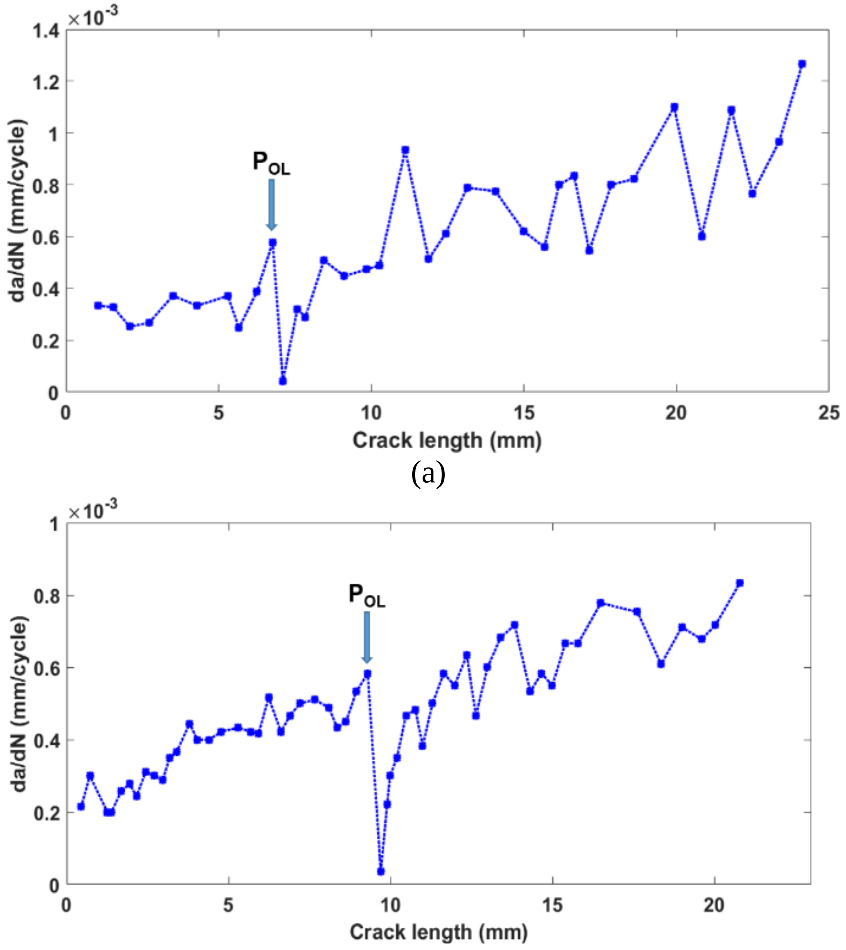

(a)

(b)

Figure 2.9: Crack growth rate as function of crack length for specimens tested with single overloads of R_{OL}=2.0

To investigate the cause of significantly larger values of R_d compared to $r_{p,OL}$, quantitative fractography was performed on the fracture surfaces in the overload affected regions to study the micromechanisms governing fatigue crack growth immediately following an overload excursion. Figure 2.10 shows the overload affected region on the fracture surface of specimen OL_T1 at a_{OL} of 16.3 mm. The $r_{p,OL}$ was calculated to be 359.8 µm and the R_d was experimentally determined to be 660 µm. The red arrow in Figure 2.10 indicates the overload line formed on the fracture surface at a_{OL}=16.3 mm and also points in the direction of crack propagation. Figure 2.10a shows a zoomed-in image of the transient region following the overload line (at a_{OL}=16.3 mm) and a ligament of approximately 600 µm can be seen to have formed along the crack propagation direction. Figure 2.10b shows a lower magnification image of the transient zone, showing formation of ligaments along the crack propagation direction. The length of the ligaments was observed to be approximately equal to the R_d (=660 µm) suggesting their significant contribution to the crack retardation that follows an overload excursion. The quantitative fractography results provide some insight into the micromechanisms influencing the post-overload fatigue crack growth.

The following important observations can be made. Due to the formation of a large plastic zone ahead of the overload line, the crack-tip splits parallel to the fracture surface resulting in the formation of ligaments in the wake of the crack-tip. The lateral splitting of the crack-tip may be attributed to the strain hardening of the region around the crack-tip in the overload plastic zone. The strain hardened region, $r_{p,OL}$, can act as a temporary barrier to the propagating crack tip causing it to split and in turn lead to the formation of the observed ligaments. These ligaments in the wake of the crack cause significant crack closure, reducing the effective ΔK and, ultimately, significantly reducing the crack growth rate. The ligaments are seen to extend past the calculated overload plastic zone size $r_{p,OL}$ = 359.8 μm ending at a distance approximately equal to R_d.

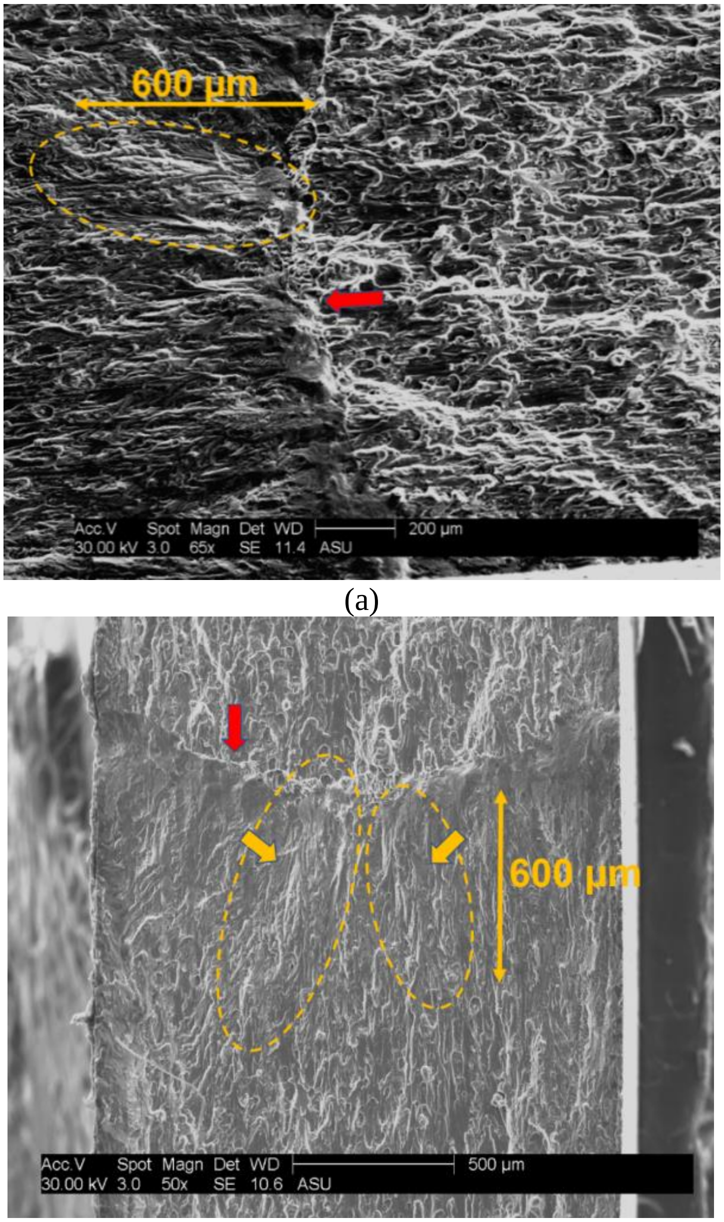

(a)

(b)

Figure 2.10: Specimen OL_T1 fracture surface (a) zoomed in image at the second overload line (b) low magnification image showing ligament formation after 2nd overload

2.3.2 Overload Ratio of 2.25

The highest magnitude overload case investigated in this work (R_{OL}=2.25) showed some interesting crack growth trends. The results are summarized in Table 2.7 and shows more prominent retardation effects, with increasing $a_{OL,}$ compared to the cases of R_{OL} 1.75 and 2.0.

Table 2.7: Biaxial fatigue tests with overloads of R_{OL} = 2.25

Spec. ID	**a_{OL}(mm)**	**ΔK (MPa√m)**	**K_{OL} (MPa√m)**	**$r_{p,CA}$ (μm)**	**$r_{p,OL}$ (μm)**	**R_d**	$\left(\frac{da}{dN}\right)_{CA}$	$\left(\frac{da}{dN}\right)_{OL}$
OL_T12	3	4.66	11.67	9.83	245.98	460	$2.08\text{x}10^{-4}$	$1.23\text{x}10^{-5}$
OL_T4	4.9	5.34	13.35	12.87	321.84	420	$3.17\text{x}10^{-4}$	$1.08\text{x}10^{-5}$
OL_T4	6	5.58	13.95	14.05	351.37	1100	$5.83\text{x}10^{-4}$	$8.7\text{x}10^{-6}$
OL_T12	10.73	6.6	16.5	19.66	491.61	840	$3.92\text{x}10^{-4}$	$1.08\text{x}10^{-5}$
OL_T4	11.8	6.8	17.01	20.89	522.40	-	$7.58\text{x}10^{-4}$	0
OL_T12	27.45	8.95	22.38	36.19	904.86	-	$7.89\text{x}10^{-4}$	0

The load spectrum applied to the specimen OL_T4 is shown in Figure 2.11a. Three single overloads of R_{OL}=2.25 were considered in the load spectrum, inserted after 25,000, 45,000 and 126,000 fatigue cycles. The crack length as a function of fatigue cycles for OL_T4 is depicted in Figure 2.11b.

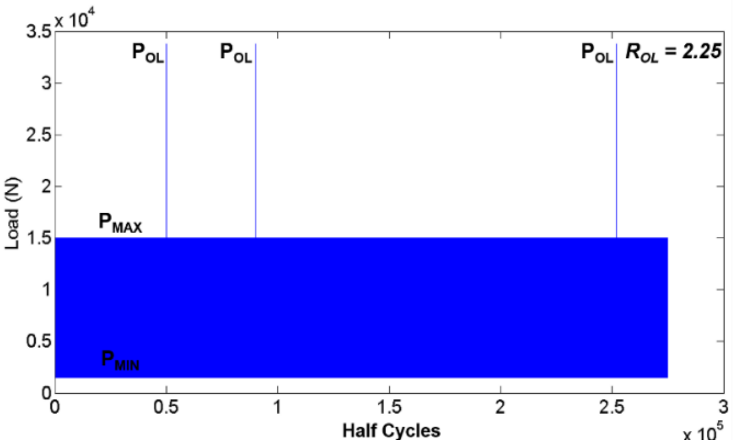
x 10^4
3.5
3
2.5
2
1.5
1
0.5
0
Load (N)
P_OL
P_OL
P_OL
R_OL = 2.25
P_MAX
P_MIN
0
0.5
1
1.5
2
2.5
3
Half Cycles
x 10^5

(a)

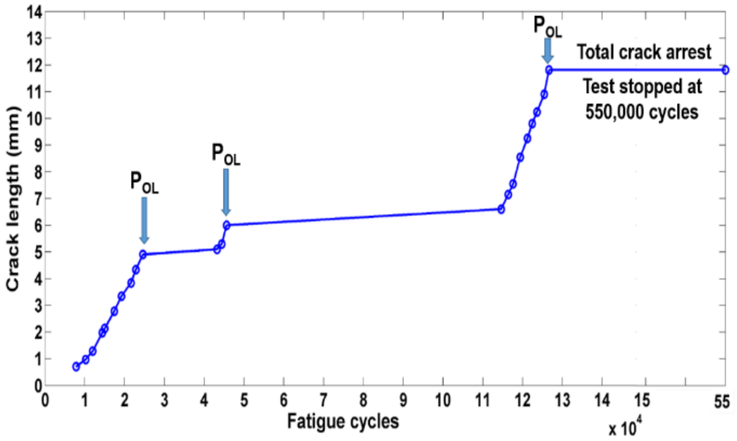
14
13
12
11
10
9
8
7
6
5
4
3
2
1
0
Crack length (mm)
P_OL
P_OL
P_OL
Total crack arrest
Test stopped at
550,000 cycles
0
1
2
3
4
5
6
7
8
9
10
11
12
13
14
15
55
Fatigue cycles
x 10^4

(b)

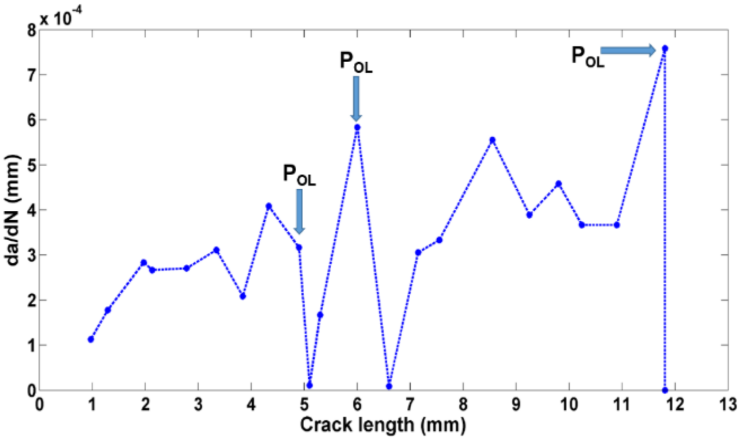
x 10^-4
8
7
6
5
4
3
2
1
0
da/dN (mm)
P_OL
P_OL
P_OL
0
1
2
3
4
5
6
7
8
9
10
11
12
13
Crack length (mm)

(c)

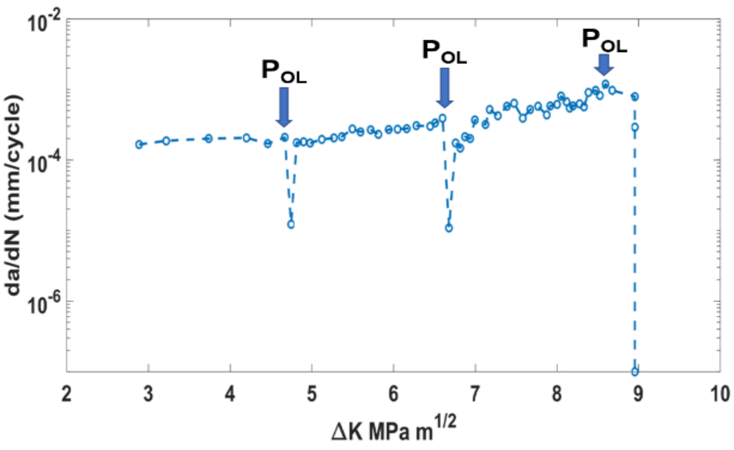

(d)

Figure 2.11: (a) Load spectrum of OL_T4 with single overloads of ROL = 2.25; (b) Crack length vs fatigue cycles for OL_T4; (c) Crack growth rate vs crack length for OL_T4; (d) Crack growth rate vs ΔK for OL_T12

For OL_T4, when the first overload occurs after 25,000 cycles, at a crack length of 4.9 mm, the crack growth approaches zero and the crack temporarily gets arrested for the next 19,000 cycles. This crack retardation for R_{OL}=2.25 is considerably more significant when compared to the crack retardation observed for R_{OL}=1.75. The retarded crack completely recovers its crack growth rate after an increment of 0.5 mm in crack length (see Figure 2.11c). This is a longer recovery distance as compared to the case of R_{OL} of 1.75 and 2.0. The R_{OL} of 2.25 results in a much larger plastic zone size that influences the crack growth rate for a longer crack increment. The second overload after 45,000 cycles, at a crack length of 6 mm, results in more severe retardation in crack growth as compared to the first overload, followed by crack arrest over the next 69,000 cycles. Figure 2.11c shows that after the second overload, the crack-tip propagates approximately 1.2 mm before the crack growth rate can fully recover from the retardation effect caused by the second overload. This can be attributed to the severe plasticity-induced crack closure caused by the large plastic zone size from the overload applied at 6 mm crack. The last overload occurs at 126,000 cycles, at a crack length of 11.8 mm, and complete crack arrest can be seen in Figure 2.11c. The specimen was fatigued till 550,000 cycles but the crack remained arrested and the test was stopped. The results from these experiments indicate that crack retardation becomes more severe as the overload ratio is increased and also if the overloads occur at a larger crack length.

Figure 2.12a shows the image of the crack just before the third overload and Figure 2.12b shows the image of the crack at the end of the test showing the arrested crack-tip. The crack length does not increase after the third overload and the crack-tip becomes blunt due to the very high plasticity induced crack closure effect from the third overload since the crack length at this instance was larger than it was at the first two overloads.

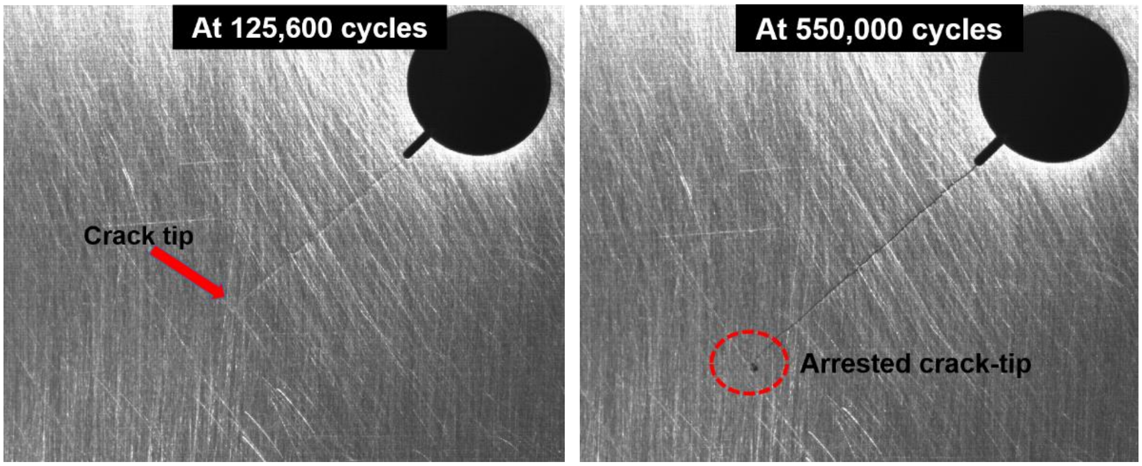

Figure 2.12: Fatigue crack images of specimen OL_T4 subjected to single overloads with R_{OL} of 2.25

Severe crack retardation was observed for the first two overloads that occurred at 25,000 cycles (4.9 mm crack) and 45,000 cycles (6 mm crack), whereas total crack arrest occurred at the third overload which occurred at 126,000 cycles (11.8 mm crack). Figure 2.13a shows the influence of overloads on the crack tip path. Due to blunting of the crack tip from severe plasticity induced crack closure, the crack tip splits and the crack path no longer stays along the direction that maximizes mode-I stresses at the crack tip. This change in crack path mitigates the mode-I crack driving force and gives rise to a mixed mode stress state at the crack tip. The fracture surface in the region affected by the first overload is shown in Figure 2.13b. Since the overload ratio applied in this case was 2.25, a prominent overload line is visible. Figure 2.13c shows the highly uneven fracture surface formed after the overload at a_{OL}=6mm, indicating the deflection and splitting of the crack tip. Formation of dimples along the overload line, as seen in Figure 2.13c, is indicative of extremely high ΔK that arises due to the high overload ratio[40]. Dimple formation on the fracture surface was not observed for the lower overload ratios of 1.75 and 2.0. Fractographic evidence collected from fatigued specimens tested with single overloads of R_{OL}=2.25 suggests that mode-II stresses arise after the occurrence of an overload, since crack tip tends to deflect and split, leading to change in crack propagation direction at the microscale. Figures 2.13d and 2.13e show the region of the fracture surface immediately after the overload at 6 mm crack length. In Figure 2.13d, shearing marks along the crack propagation direction are indicative of the presence of mode-II driving forces. Figure 2.13e shows abrasion marks that form due to sliding of crank flanks under the influence of mode-II stresses at the crack tip. The sliding of the crack flanks due to mode-mixity further retards crack growth due to the roughness induced crack closure that is a consequence of interlocking of crack asperities in the wake of the crack.

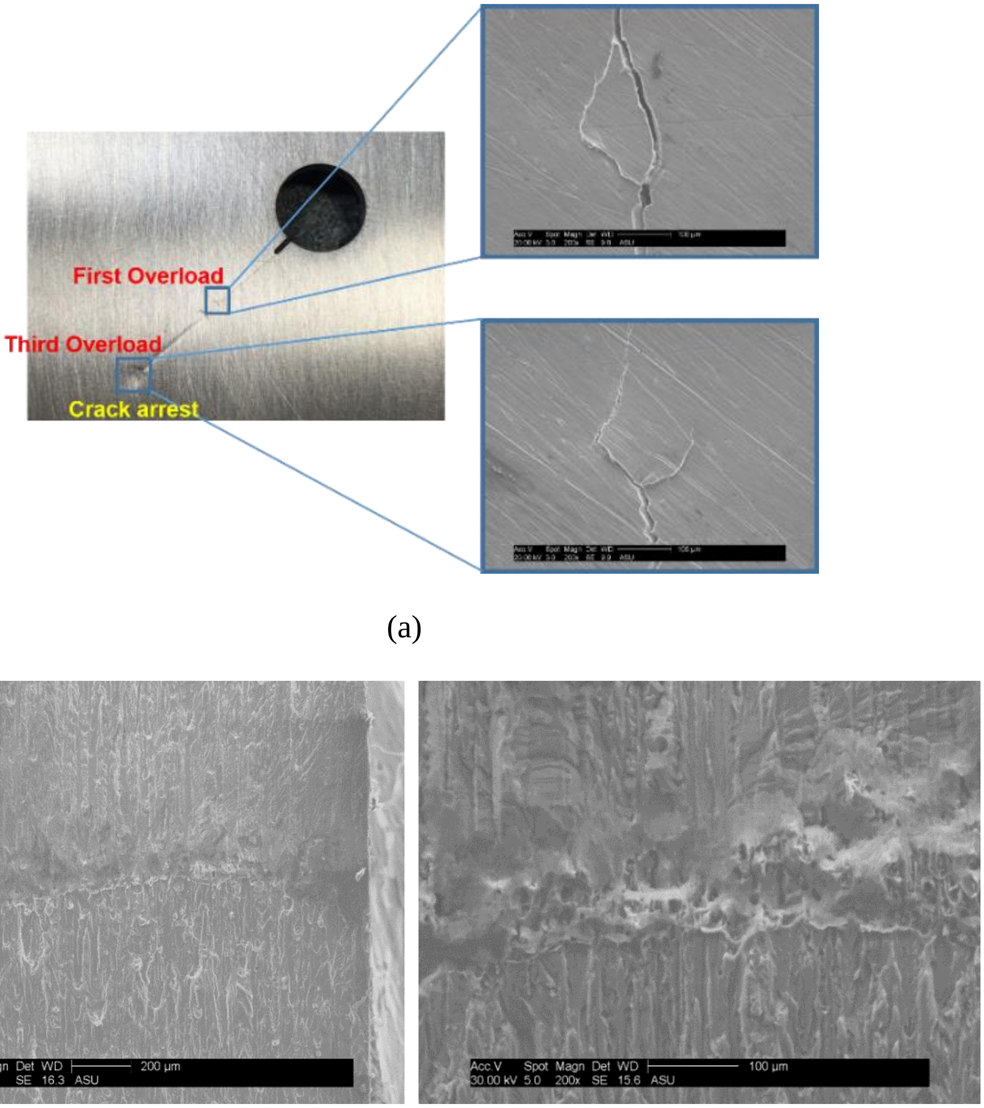

(a)

(b)

(c)

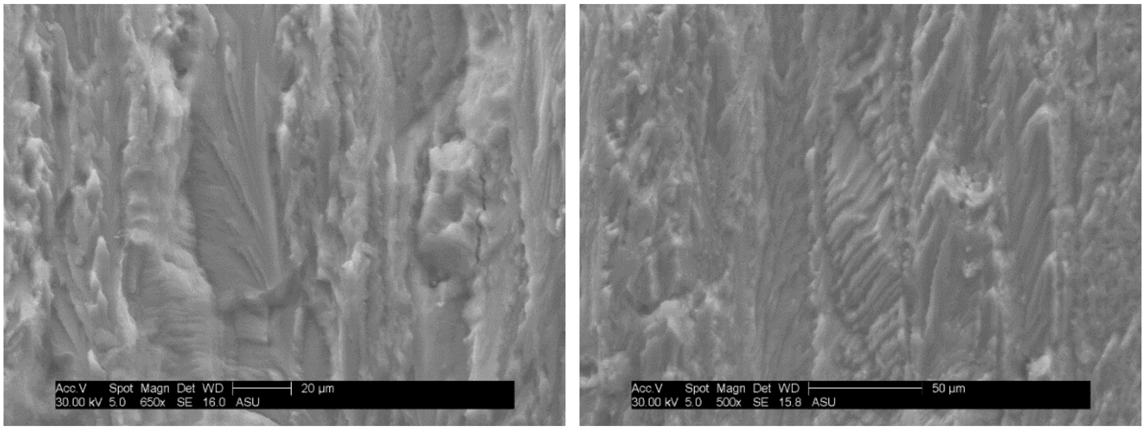

(d) (e)

Figure 2.13 (a) Fatigue crack path in specimen OL_T4; (b) low magnification image of overload line at aOL = 6 mm; (c) higher magnification image of overload line at aOL = 6 mm; Fracture surface after overload at aOL = 6 mm showing: (d) shearing marks; (e) abrasion marks

At a_{OL}=4.9 mm the $r_{p,OL}$ was calculated to be 321.84 µm and the R_d was experimentally determined to be 420 µm. Figure 2.14a shows the fracture surface in the transient region following the overload at a_{OL}=4.9 mm. Fracture features similar to the case of specimens tested with R_{OL}=1.75 were observed, showing the formation of ligaments of length 500 µm, which approximately equal to the experimentally observed R_d value (420 µm). When the overload of R_{OL}=2.25 occurred at a_{OL}=6 mm, $r_{p,OL}$ was calculated to be 351.37 µm and R_d was found to be 1100 µm. This significantly high value of R_d may be attributed to the relatively smaller gap between the overloads that occurred in this specimen at a_{OL} of 4.9 mm and 6 mm. The noteworthy increment in R_d from 420 µm to 1100 µm with a difference in a_{OL} of only 1.1 mm suggests that the retardation effect of first overload at a_{OL}= 4.9 mm contributes to the severity of retardation caused by the 2nd overload that occurs soon after, at a_{OL}= 6 mm[19]. Figure 2.14b shows the electron micrograph of fracture surface in the transient region following the overload at a_{OL}= 6 mm. The length of the ligament formed following the overload excursion can be seen to be approximately 915 µm, which is close to the experimentally determined R_d value of 1100 µm. Hence, deflection of the crack-tip that gives rise to mode-mixity, formation of ligaments in the wake of the crack (irregular crack front) and crack-tip blunting due to plasticity induced crack closure were seen to be active micromechanisms governing crack retardation in the case of single overloads with R_{OL}=2.25.

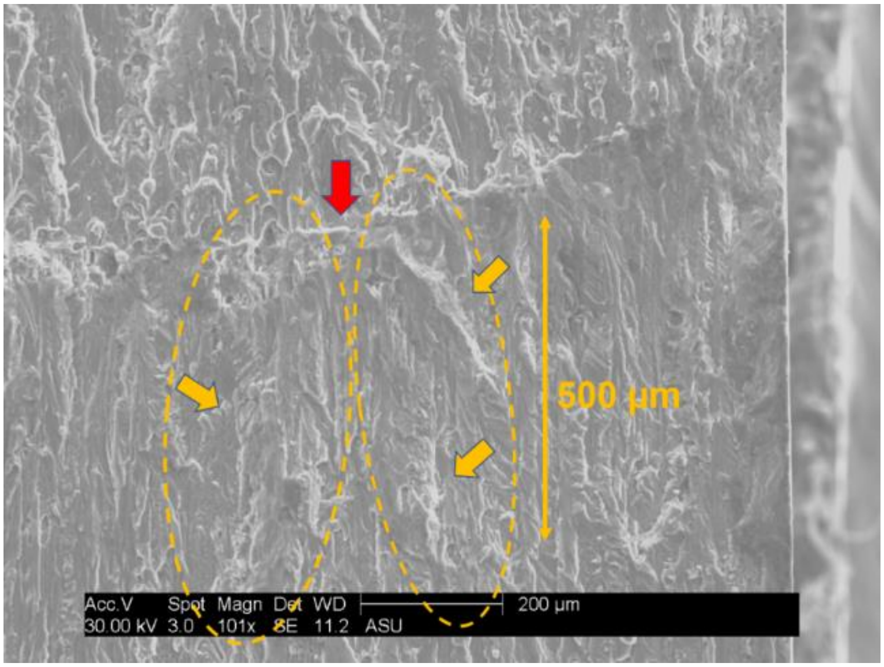

(a)

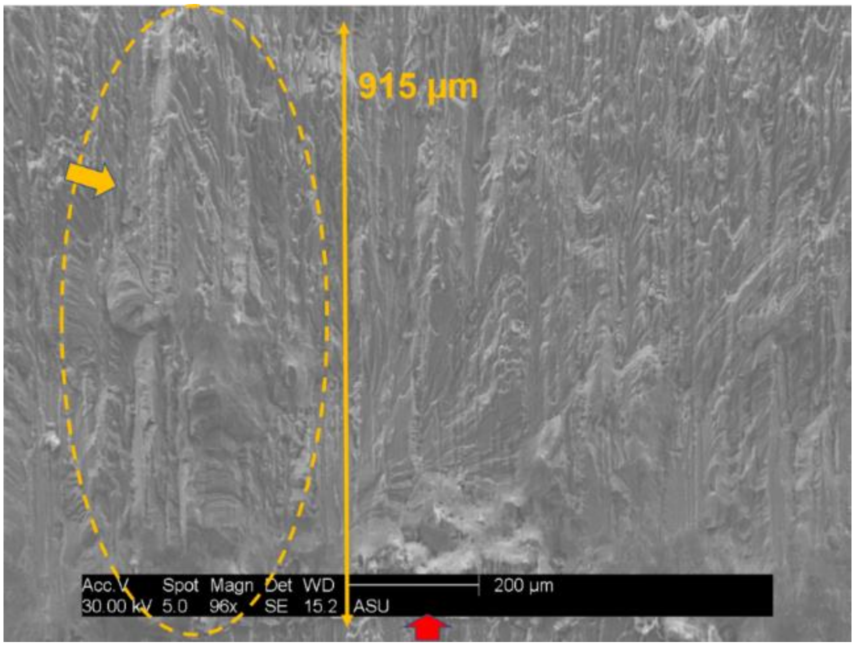

(b)

Figure 2.14: Fractographs of specimen OL_T4 showing ligament formation in the regions affected by overload at (a) a_{OL}= 4.9 mm and; (b) a_{OL}= 6 mm

Figure 2.15 shows the trend of R* as a function of overload crack length for different overload ratio cases. It is noteworthy to analyze the trend of R* with respect to different overload crack lengths and overload ratios to understand the dependence of crack retardation behavior in the short crack regime as well as the long crack regime. It can be noted from Figure 2.15 that the retardation distance for all the different overload cases shows a similar trend with respect to the overload crack length (a_{OL}). The respective retardation distance values show a drastic increase when the a_{OL} shifts from 0-5 mm range to >5mm, following which they increase steadily with increasing a_{OL}. This indicates that the retardation effects become more severe as soon as the crack enters the long crack regime and the different retardation mechanisms observed in this regime contribute significantly to the crack retardation. Fractography results confirmed that for $a_{OL} < \approx$5mm, plasticity induced crack closure was the primary mechanism governing the retardation. Whereas for a_{OL} > ≈5mm, mechanisms such as crack deflection, crack splitting and ligament formation contributed significantly to the crack retardation, in addition to the plasticity induced closure.

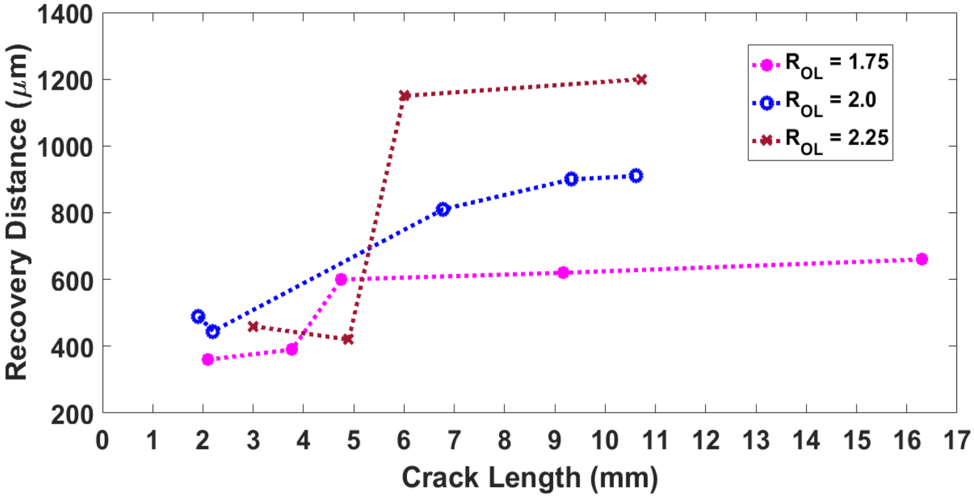

Figure 2.15 Recovery distance as a function of overload crack length

2.3.3 Underloads and Overload/Underload Combinations

For the specimen UL_T1, the load spectrum with 1.5-15 kN loading was applied to this specimen and two single underloads with R_{UL}=-0.5 were inserted in the load spectrum after 30,000 and 65,000 fatigue cycles. Figure 2.16a shows the load spectrum with the single underloads. The crack length as a function of cycles and the crack growth rates as a function of crack length are presented in Figure 2.16b and 2.16c. No significant change in the crack growth behavior was observed after the underload occurred at 65,000 cycles. After the underload, the crack continued to propagate at nearly the same rate as it was propagating before the underload. Zhao et al. (2008) reported similar findings regarding effect of underloads on crack growth. They found that the effect of underloads was insignificant at lower loading amplitude. However, when they increased the loading amplitude, the effect of underload on crack growth became noticeable but was still insignificant.

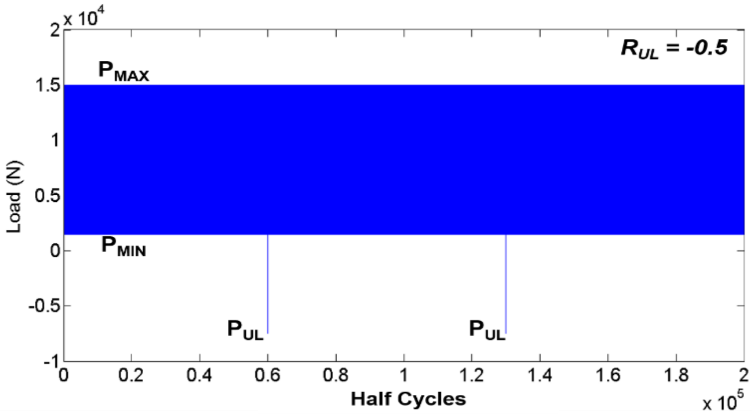

(a)

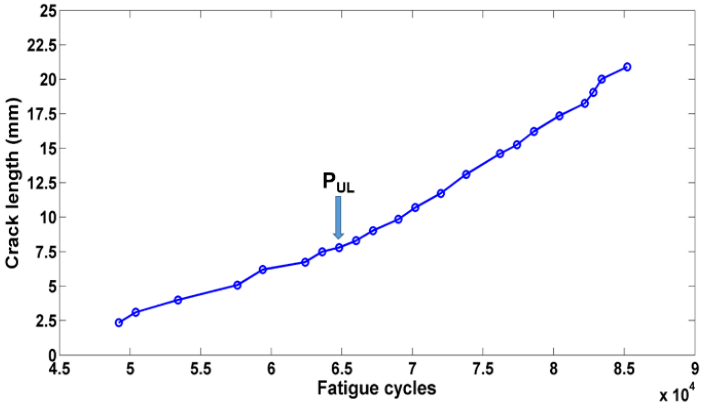

(b)

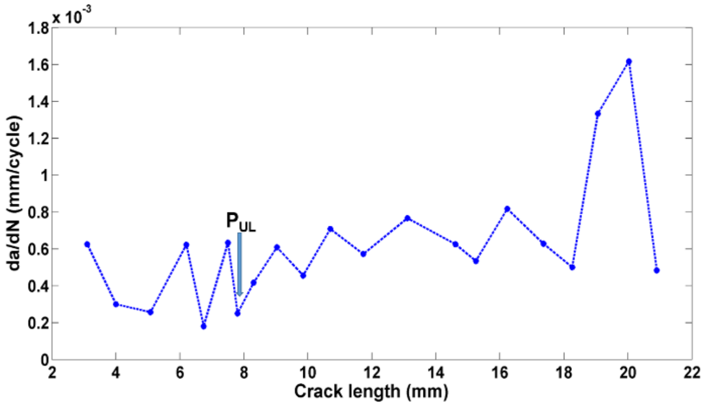

(c)

Figure 2.16: Specimen UL_T1 (a) Load spectrum with underloads; (b) crack length vs cycles; (c) crack growth rate vs crack length

Hence, for test UL_T2, the 2-20 kN load spectrum was used with single underloads of R_{UL}=-0.5. The crack growth data for the specimen tested under 2-20 kN load spectrum with single underloads is presented in Figure 2.17. As can be noticed from these data plots, following the occurrence of the underload, there is slight increase in the crack growth rate. This increase is not substantial but however it is noticeable.

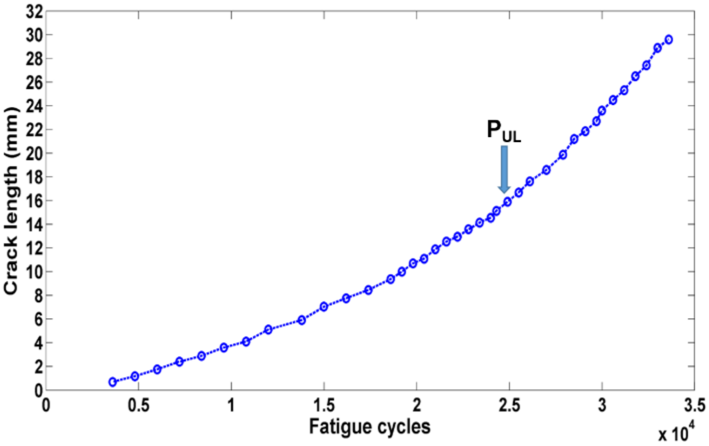

(a)

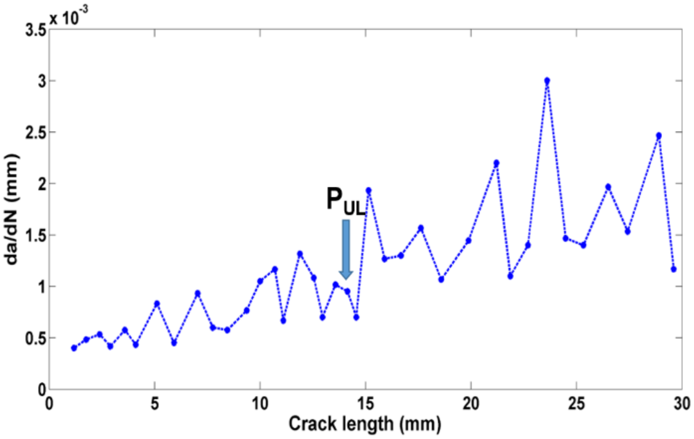

(b)

Figure 2.17: Crack growth data for UL_T2; (a) Crack length as a function of fatigue cycles; (b) crack growth rate as a function of crack length

The effect of underload was not distinctly noticeable on the fracture surface as shown in Figure 2.18. However, shear lips can be seen to form in Figure 2.18a, when the underload occurs at 25,000 cycles at a crack length of 14.56 mm. Figure 2.18b shows the abraded region and annihilated striations on the fracture surface caused due to the compressive underload. The abrasion marks and annihilation of striations is caused due to the crack flanks coming in contact during the underload cycle. The insignificant changes in fracture surface morphology also indicates the negligible change in macroscale crack growth rate observed after the occurrence of underload.

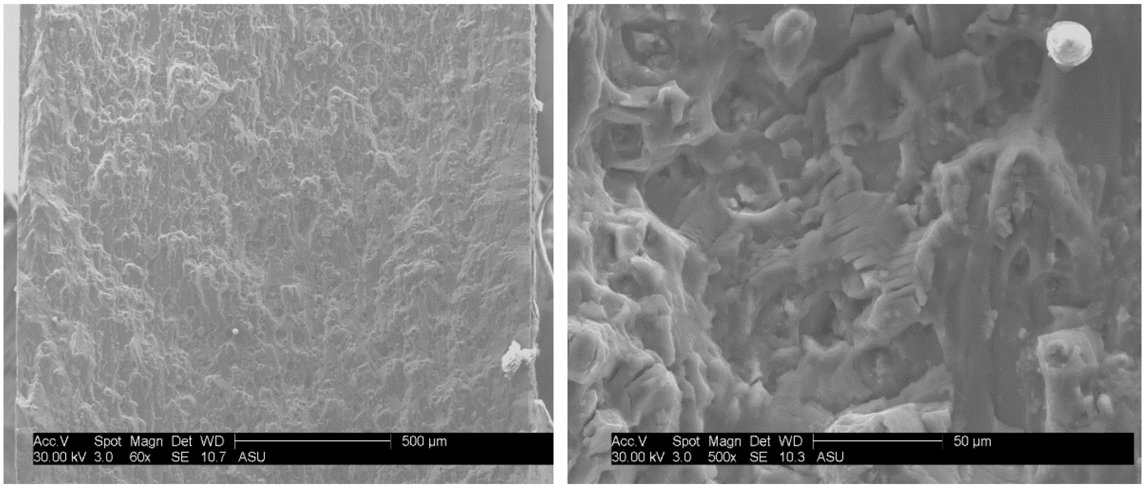

Figure 2.18: Fracture surface of specimen tested with single underloads: (a) low magnification SEM image of underload affected region; (b) abraded fracture surface with annihilated striations

The load spectrum with 1.5-15 kN loading was applied to specimens OL_13 and OL_15 and single overload of R_{OL}=1.75 immediately followed by an underload of R_{UL}=-0.5 were inserted in the load spectrum after 30,000 CA fatigue cycles. Figure 2.19 shows the load spectrum with the overload and underload combination occurring at 30,000 cycles.

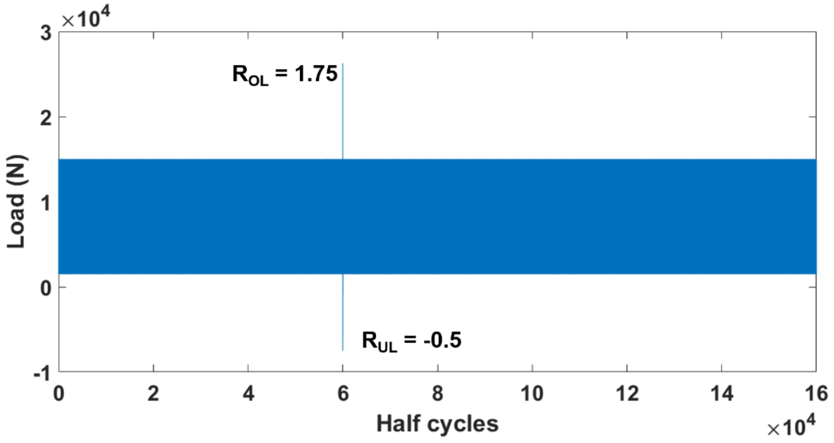

Figure 2.19: 1.5-15 kN load spectrum with single overload (R_{OL} = 1.75) and single underload (R_{UL} = -0.5) combination at 30,000 cycles

The crack length as a function of cycles for OL_T13 is depicted in Figure 2.20a. It can be seen that a 0.25 mm crack was formed after 7200 cycles and the crack propagated at a relatively consistent rate up till 30,000 fatigue cycles where an overload (R_{OL} = 1.75) immediately followed by underload (R_{UL} = -0.5) were applied. This OL+UL event occurs at 5.37 mm crack length, and there is a noteworthy drop in the crack growth rate. The crack growth rate recovers over the next 260 µm crack increment (see Figure 2.20b). This recovery distance (R_d) of 0.26 mm is significantly shorter compared to the cases where only a single overload of R_{OL}=1.75 (no underload) was applied at a similar crack length. For reference, Table 2.3 presents the R_d values for the case of single overloads without underloads. For single overload of R_{OL}=1.75 at a crack length of 4.75 mm, the R_d was found to be 600 µm. The significantly shorter R_d for the case of OL+UL can be attributed to the residual tensile stress caused by the underload that acts immediately after the overload, mitigating the plasticity induced crack closure effects of the overload. Previous tests with single underloads have revealed that underloads result in slight increase in crack growth rates since they cause residual tensile stresses around the crack-tip. The fracture surfaces also suggested sharpening of the crack-tip due to the single compressive underload. Hence, the residual tensile stress and re-sharpening of the crack-tip due to underload overcome the residual compressive stress and crack blunting caused by the overload to some extent in the case of specimens tested with OL+UL combinations (OL_T13 and OL_T15). This leads to a significantly shorter recovery distance.

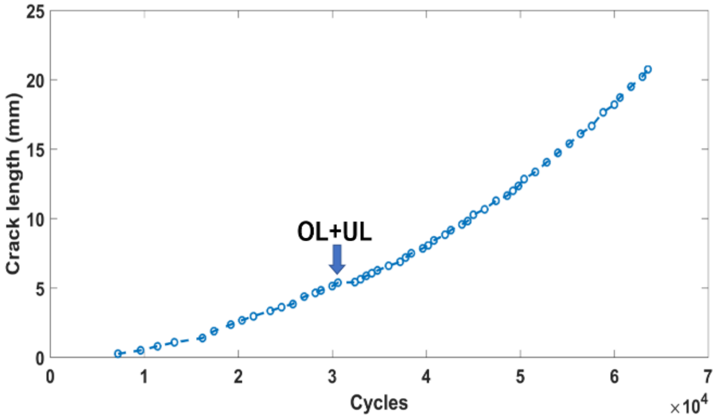

(a)

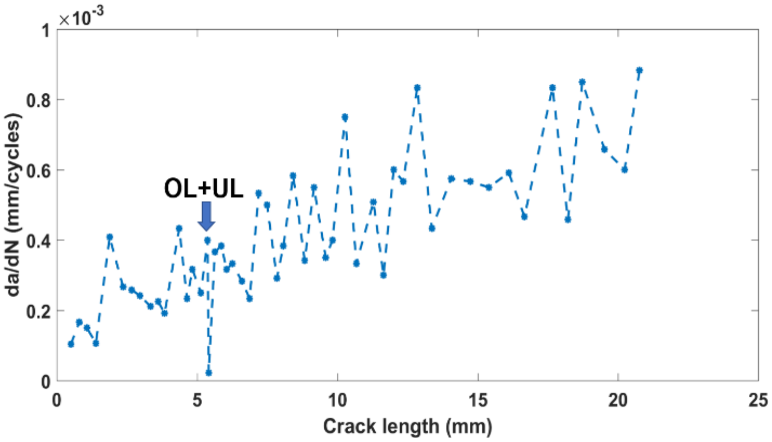

(b)

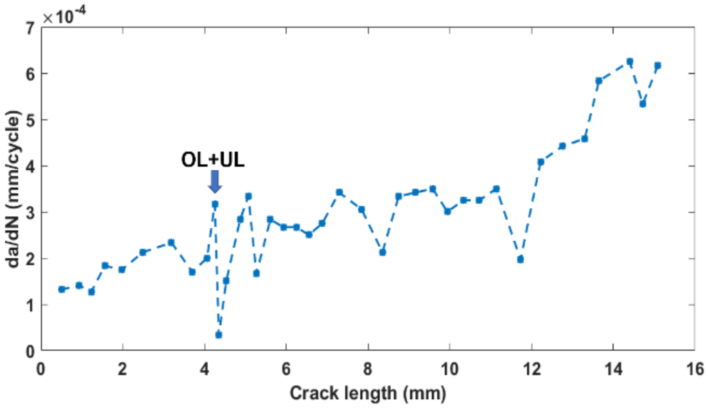

(c)

Figure 2.20: (a) Crack length as a function of fatigue cycles; for OL_T13; (b) crack growth rate as a function of crack length for OL_T13; (c) crack growth rate as a function of crack length for OL_T15

Figure 2.21 shows the region of fracture surface where the OL+UL combination occurs at 5.37 mm crack length. Figures 2.21a and 2.21b show the overload line formed by the overload of R_{OL} = 1.75. The overload line can be seen to be discontinuous and flattened due to the underload of R_{UL}= -0.5 that followed immediately. The occurrence of underload immediately after the overload mitigates the crack-tip blunting and the overload line is observed to be significantly finer than in the case with single overload without underload.

The fracture surface region ahead of the overload line is depicted in Figure 2.21c. Flatter regions and sheared grains can be observed to form ahead of the overload line indicating an abrupt increase in crack growth after the overload induced crack retardation. These features can be attributed to the occurrence of underload, which leads to residual tensile stresses around the crack-tip, that in turn increase the crack growth rate. Figure 2.21d shows the fracture surface region just before the overload line. Annihilated striations can be seen before the overload line, in the wake of the crack, due to the crack faces sliding under the influence of compressive underload. This further reduces the crack closure by flattening the fracture region in the wake of the propagating crack-tip. Hence, the reduced recovery distance can be attributed to the fracture mechanisms can be travelled by the crack-tip to resume normal crack growth rates comparable to growth rates before the overload occurrence.

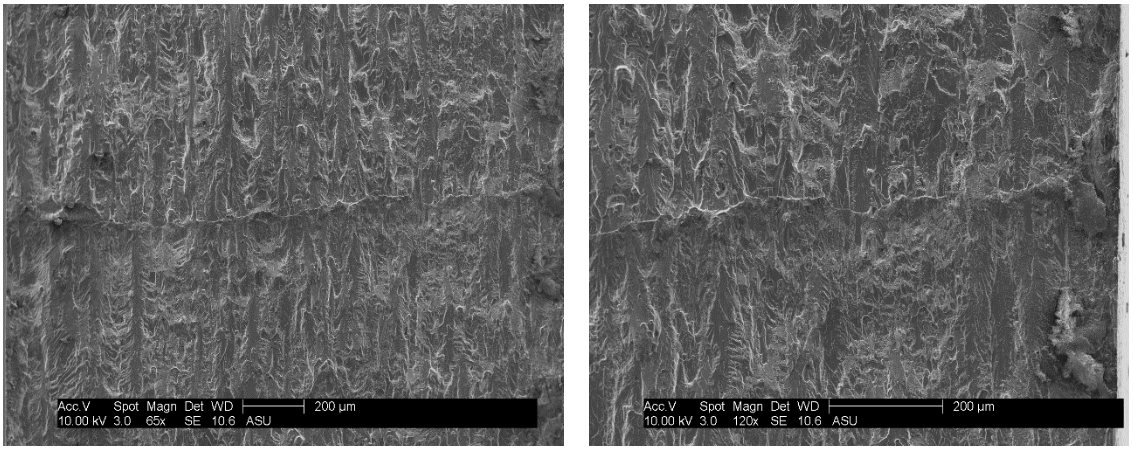

(a) (b)

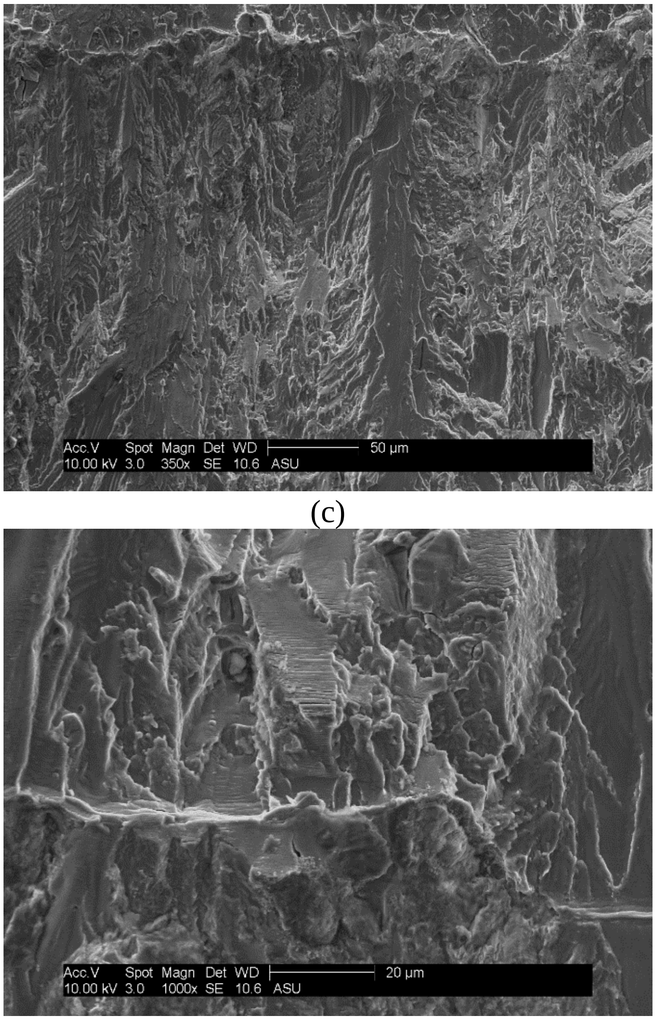

(c)

(d)

Figure 2.21: Fractography scans of sample OL_13 tested with OL+UL combination at 5.37 mm crack length

The load spectrum with 1.5-15 kN loading was applied to specimens OL_14 and OL_16 and single overload of R_{OL}=1.75 immediately followed by an underload of R_{UL}=-0.5 were inserted in the load spectrum after 50,000 CA fatigue cycles. Figure 2.22 shows the load spectrum with the overload and underload combination occurring at 50,000 cycles.

The crack length as a function of cycles for OL_T14 is depicted in Figure 2.23a. It can be seen that a 0.26 mm crack was formed after 8200 cycles and the crack growth rate increases relatively consistently up to 50,000 fatigue cycles where an overload ($R_{OL} = 1.75$) immediately followed by underload ($R_{UL} = -0.5$) were applied. This OL+UL event occurs at 13.31 mm crack length, and there is a noteworthy drop in the crack growth rate. The crack growth rate recovers gradually over the next 600 µm crack increment (see Figure 2.23b). This recovery distance (R_d) of 0.6 mm is comparable to the cases where only a single overload of R_{OL}=1.75 (no underload) was applied at similar crack lengths. This crack retardation behavior is different from the case when OL+UL combination is applied at smaller crack lengths.

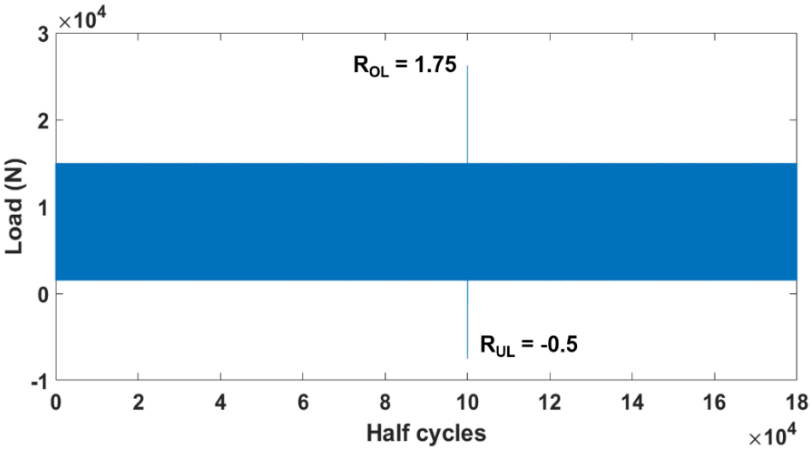

Figure 2.22: 1.5-15 kN load spectrum with single overload ($R_{OL} = 1.75$) and single underload ($R_{UL} = -0.5$) combination at 50,000 cycles

Since R_d for the case of OL+UL at larger crack lengths is comparable to that of the case of single overloads, it can be concluded that underloads do not have significant influence on the retardation effects caused by overloads at larger crack lengths. This can be attributed to severe crack-tip blunting that occurs due to plasticity induced crack closure at larger crack lengths. Also, the crack closure due to residual compressive stresses in the wake of the crack-tip is high for longer cracks. Hence, the effect of underloads on crack growth rate at larger crack lengths can be said to be insignificant.

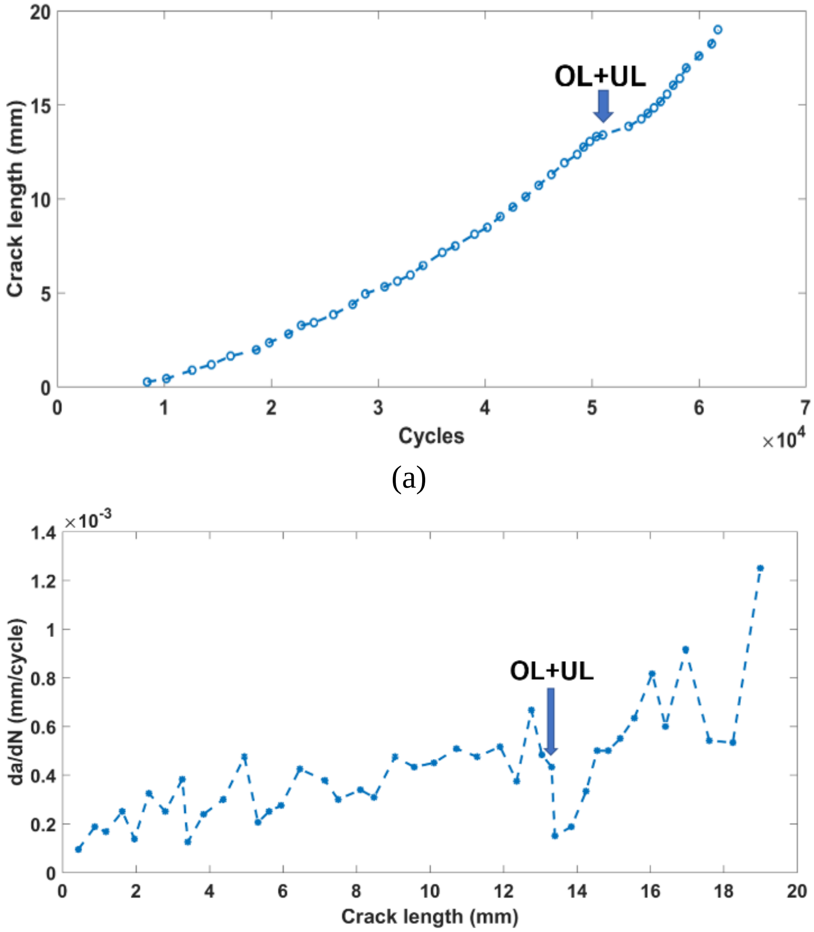

(a)

(b)

Figure 2.23: Crack growth data for OL_14; (a) Crack length as a function of fatigue cycles; (b) crack growth rate as a function of crack length

2.4 Summary

In this chapter, an in-plane biaxial study of Al 7075-T651, subjected to single overloads of different magnitudes occurring at increasing crack lengths has been presented. Detailed fractography has been conducted to characterize the crack retardation behavior due to the influence of single overloads. The following are some important observations from this study. The micromechanisms associated with crack retardation were governed by the magnitude of overload and the crack length at which the overload occurred. The recovery distance following an overload was found to be directly proportional to overload magnitude as well as the crack length at overload. Crack retardation due to lower overload ratios was found to be governed by plasticity induced crack closure in the form of crack-tip blunting. At higher overload ratios, the crack retardation was a result of the combined influence of crack-tip deflection, roughness induced crack closure, crack-tip blunting (plasticity induced crack closure) and crack-tip splitting (irregular crack front). The effects of residual stresses that arise due to overloads will be investigated in future work. Total crack arrest was observed in case of high overload excursions with overload ratio of 2.25 at larger crack lengths. The observations from this study provide some important insight into the distinct micromechanisms that govern the crack growth behavior due to the presence of overloads in biaxial fatigue loading.

In the case of single underload of $R_{UL} = -0.5$, no significant change in crack growth rate was observed when the underload was applied between CA cycles of 1.5-15 kN. However, when the amplitude of CA cycles was increased to 2-20 kN, the occurrence of underload caused a slight increase in crack growth rate, attributed to the residual tensile stresses caused by the underload. When an underload was applied immediately after an overload, the retardation effects from the overload were seen to get mitigated, and the crack growth rate recovered faster since the underload caused re-sharpening of the crack-tip that was blunted by the overload.

Some important characteristics of biaxial fatigue crack growth behavior under the influence of single overloads of different magnitudes are presented below:

- The *transient region* (R_d) was experimentally determined to be greater than the calculated overload plastic zone size ($r_{p,OL}$) by a factor of 2 to 3.
- Quantitative fractography of fatigue specimens tested with R_{OL}=1.75 showed the formation of ligaments along the crack propagation direction, immediately after an overload excursion. The length of these ligaments was found to be approximately equal to the size of transient region (R_d).
- Ligament formation and splitting/branching of the crack-tip after the occurrence of overload were found to be the dominant micromechanisms governing crack growth retardation.
- The size of the transient zone (R_d) was found to increase with increasing R_{OL} and a_{OL} values.
- At higher overload ratio (R_{OL}=2.25), the crack growth retardation was found to occur due to the combined effect of lateral crack-tip splitting and deflection of the crack-tip that caused mode-II induced crack closure.

- When a single overload occurred at higher a_{OL} values in the case of R_{OL}=2.25, total crack arrest was observed. This phenomenon was not observed in the case of R_{OL} of 1.75 and 2.0.

3 BIAXIAL FATIGUE CRACK GROWTH IN AL 7075 T651 ALLOY UNDER MIXED-MODE OVERLOADS

3.1 Introduction

Service loads in metallic aircraft structures often consist of multiaxial fatigue loading having variable amplitude (VA), mixed-mode fatigue cycles. Hence, the service loads are essentially in the form of a series of overload and/or underload fatigue cycles with varying mode-mixities, resulting in highly complex crack growth behavior in aerospace alloys. As mentioned in Chapter 1, a multitude of fatigue studies have been conducted on investigating the crack growth acceleration and retardation behavior under mixed-mode overloads through the application of uniaxial loads using specialized load-distribution fixtures. This induces a multiaxial stress-state at the crack-tip and allows for the investigation of crack propagation behavior under more realistic mixed-mode loading conditions using uniaxial fatigue frames. However, a more effective way to capture crack growth behavior under realistic service loading conditions is through the use of a multiaxial fatigue frame that allows for the application of in-phase, out-of-phase and non-proportional loads, in addition to loadings with different biaxiality ratios (BR).

Several studies in literature have discussed the fatigue-fracture mechanisms such as roughness induces crack closure, plasticity induced crack closure, crack deflection and crack branching, that govern crack growth characteristics under mixed-mode overloads. However, there is lack of clear experimental evidence regarding the role played by the proposed crack growth micromechanisms in the case of different overload magnitudes and mode-mixities, and their direct dependence on the instantaneous fatigue crack length.

Hence, the focus of this chapter is to comprehensively investigate the micro- and macroscale crack growth behavior under the influence of individual mixed-mode overloads of different magnitudes and mode-mixities, applied in the form of biaxial fatigue loads of different BR. Special attention has been given to the analysis of crack retardation mechanisms that get activated due to the occurrence of mixed-mode overloads.

In this chapter, the effects of mixed-mode overloads caused due to BR≠1 is investigated for the aerospace grade Al 7075 T651 alloy. Pure mode-I crack growth was obtained using biaxial fatigue CA spectrum with BR = 1, and single overloads with BR ≠ 1 were inserted after pre-determined number of CA cycles. The unequal loads along x and y axes due to an overload of BR ≠ 1 lead to a combination of mode-I and II stress states on the propagating crack-tip and the mode-mixity varies with the applied BR. This allowed for the generation of a pure mode-I pre-crack of a certain length before the mixed-mode single overload occurs. The mixed-mode overloads investigated in this research had BR of 0.5 and 0.75 with R_{OL} of 1.75, 2.0 and 2.25. The influence of overload ratio, biaxiality ratio (mode-mixity) and instantaneous crack length at the time of overload are analyzed and correlated with the macro- and microscale crack retardation behavior through quantitative fractography. The crack propagation behavior and the governing micromechanisms are correlated with those of biaxial fatigue with pure mode-I overloads presented in Chapter 2.

3.2 Materials and Experimental Methods

3.2.1 Biaxial Fatigue Test Setup

The details on the biaxial fatigue test setup including specimen design and biaxial testframe specifications can be found in the Section 4.2.1.

3.2.2 Biaxial Fatigue Load Spectra with Mixed-Mode Overloads

To study the effects of a single overload having a certain BR and R_{OL}, fatigue load spectra were generated with single overload excursions in an otherwise CA baseline loading of BR = 1, P_{max} = 15kN, R = 0.1 and a frequency of 10Hz. The effects of single overloads of BR = 0.5 and 0.75 were investigated at different crack lengths and increasing overload magnitudes (R_{OL} of 1.75 and 2.0). The summary of the fatigue tests conducted in this research work is presented in Table 3.1. The mode-mixity induced during the overload cycle of a certain BR can be expressed in terms of the mode-mixity parameter given as,

$$M_{OL} = \tan^{-1}\left(\frac{K_{II}}{K_I}\right)$$

The mode-mixity (M_{OL}) for single overloads of BR = 0.5 and 0.75 was calculated to be π/8 and π/18, respectively. For reference, it can be noted that M_{OL}= π/2 corresponds to pure mode-II stress-state.

Table 3.1: Overload tests conducted with BR of 0.5 and 0.75 with R_{OL} of 1.75, 2 and 2.25 occurring at different crack lengths (a_{OL})

Test ID	**R-ratio**	**P_{max} (kN)**	**BR_{OL} ($P_{Y,OL}$/ $P_{X,OL}$)**	**$P_{Y,OL}$ (kN)**	**$P_{X,OL}$ (kN)**	**R_{OL} (P_{OL}/ P_{max})**	**N_{OL} (cycle)**
OL_T19	0.1	15	0.5	26.25	13.125	**1.75**	25,000
OL_T19	0.1	15	0.5	26.25	13.125	**1.75**	55,000
OL_T20	0.1	15	0.5	26.25	13.125	**1.75**	25,000
OL_T20	0.1	15	0.5	26.25	13.125	**1.75**	55,000
OL_T21	0.1	15	0.5	26.25	13.125	**1.75**	40,000

OL_T21	0.1	15	0.5	26.25	13.125	**1.75**	80,000
OL_T22	0.1	15	0.5	30	15	**2.0**	25,000
OL_T22	0.1	15	0.5	30	15	**2.0**	65,000
OL_T23	0.1	15	0.5	30	15	**2.0**	35,000
OL_T23	0.1	15	0.5	30	15	**2.0**	75,000
OL_T24	0.1	15	0.5	30	15	**2.0**	35,000
OL_T24	0.1	15	0.5	30	15	**2.0**	75,000
OL_T25	0.1	15	0.5	26.25	13.125	**1.75**	40,000
OL_T25	0.1	15	0.5	26.25	13.125	**1.75**	80,000
OL_T26	0.1	15	0.5	37.5	18.75	**2.5**	25,000
OL_T26	0.1	15	0.5	37.5	18.75	**2.5**	65,000
OL_T27	0.1	15	0.5	37.5	18.75	**2.5**	25,000
OL_T27	0.1	15	0.5	37.5	18.75	**2.5**	65,000
OL_T29	0.1	15	0.75	26.25	19.68	**1.75**	25,000
OL_T29	0.1	15	0.75	26.25	19.68	**1.75**	55,000
OL_T30	0.1	15	0.75	26.25	19.68	**1.75**	30,000
OL_T30	0.1	15	0.75	26.25	19.68	**1.75**	60,000
OL_T31	0.1	15	0.75	26.25	19.68	**1.75**	35,000
OL_T31	0.1	15	0.75	26.25	19.68	**1.75**	65,000
OL_T32	0.1	15	0.75	26.25	19.68	**1.75**	35,000
OL_T32	0.1	15	0.75	26.25	19.68	**1.75**	65,000

3.2.3 Quantitative Fractography

Following the fatigue tests, quantitative fractography was performed on the specimens using scanning electron microscopy (SEM). The microstructural crack growth features were obtained and correlated to the load history, crack growth rate, crack path and crack-tip plasticity. Fracture features corresponding to overloads of different BR and R_{OL} were identified and their influence on macro- and microscale crack growth was investigated. Specifically, the transient region, which is the overload affected region where crack retardation is observed, was scanned for fracture modes known to resist crack propagation. Although, micromechanisms such as crack-tip blunting due to plasticity, roughness induced crack closure due to mode-mixity, crack deflection and crack-tip splitting have been reported to reduce crack growth rate, it is crucial to determine their individual contributions with respect to different overload magnitudes and instantaneous crack length. Fracture surfaces were cut out from the fatigued cruciform specimens using a low-speed diamond saw, and then sonicated in acetone to remove debris and the cutting fluid. Cleaned fracture surfaces were dried using compressed air and then mounted onto metallic stubs for SEM analysis.

3.3 Results and Discussions

3.3.1 Overloads of Biaxiality Ratio 0.5

The load spectrum used for specimens OL_T19 and OL_T20, is shown in Fig. 3.1a. Single overloads with R_{OL}=1.75 having BR=0.5 (M_{OL}=π/8) were inserted in the load spectrum after 25,000 and 55,000 CA fatigue cycles of BR=1. The crack length as a function of fatigue cycles for specimen OL_T19 and OL_T20 are shown in Fig. 3.1b and

3.1c. It can be observed from Fig. 3.1b and 3.1c that crack retardation occurs immediately after the occurrence of overloads and the retardation effect lasts longer for the overload at 25,000 cycles as compared to the overload at 55,000 cycles. The slope can be seen to recover after approximately 8000 fatigue cycles in the case of overload at 25,000 cycles, whereas after the overload at 55,000 cycles the slope recovers within the next 4000 cycles. Figure 3.2a and 3.2b show the crack growth rates as a function of crack length for specimens OL_19 and OL_20, respectively. For comparison, Fig. 3.2c shows crack growth rate as a function of crack length for a specimen tested with overloads of same overload ratio (R_{OL}=1.75) but with a BR=1.

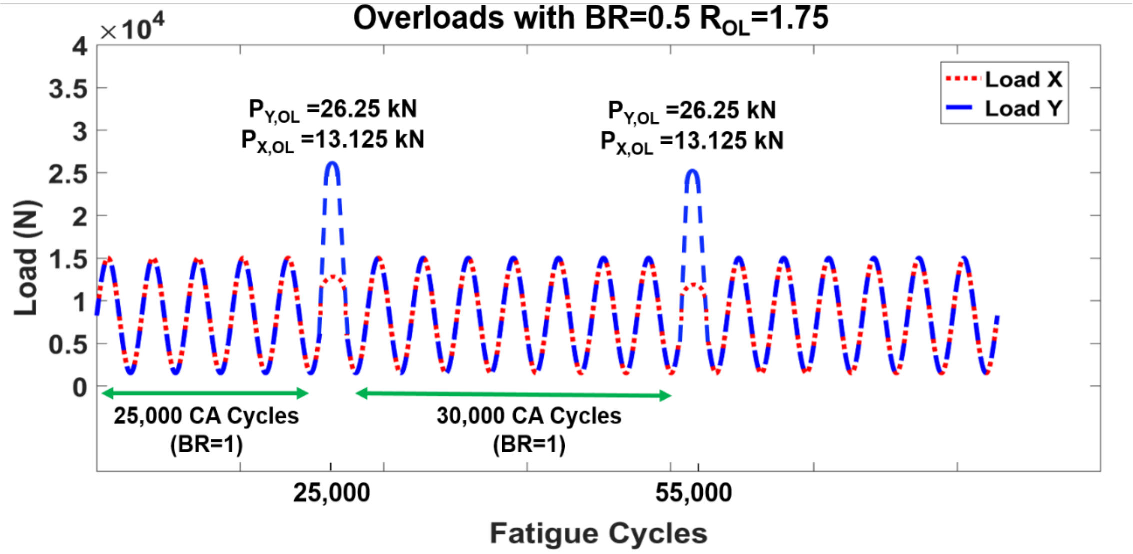

(a)

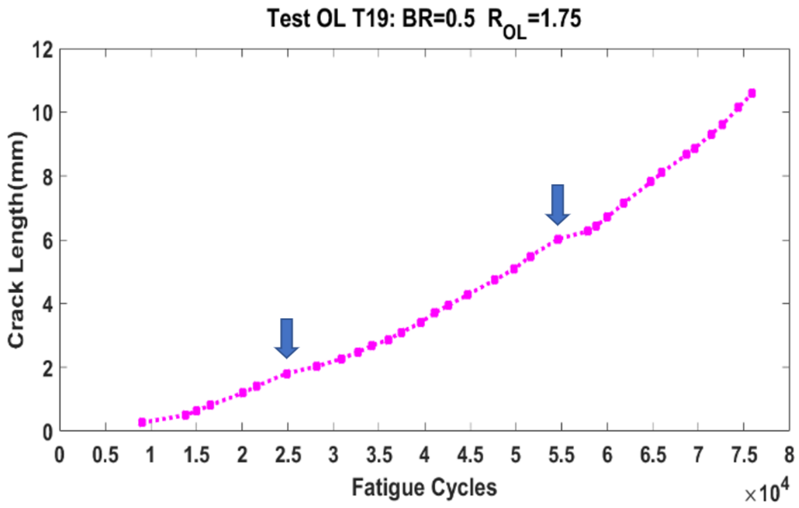

(b)

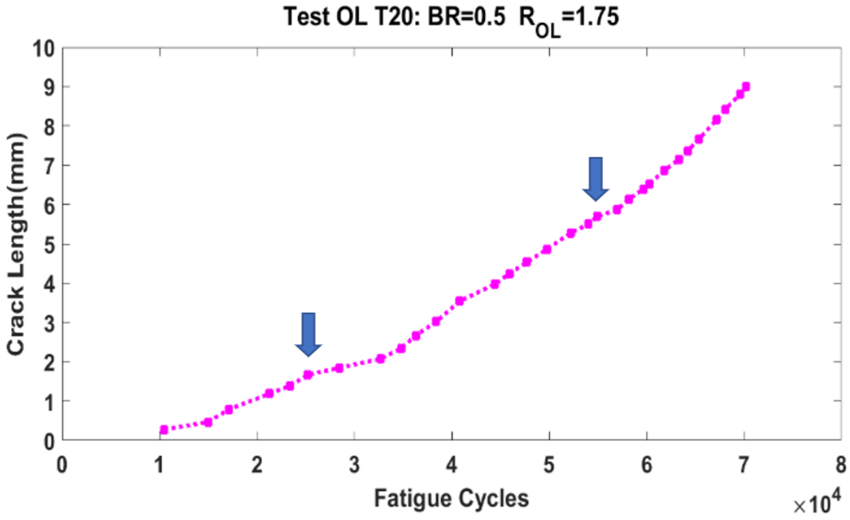

(c)

Figure 3.1: (a) Load spectrum with single overloads of ROL=1.75 and BR=0.5 at 25,000 and 55,000 fatigue cycles; (b) Crack length vs cycles for specimen OL_19; (c) Crack length vs cycles for specimen OL_T20

Figure 3.2a. and 3.2b show that an immediate reduction in the crack growth rate (da/dN) occurs after the excursion of individual overloads of BR=0.5. For the specimen

OL_19, the first overload occurred at a crack length (a_{OL}) of 1.81 mm and the second overload occurred at an a_{OL} of 6.02 mm. However, the recovery distance (R_d) propagated by the crack-tip for crack growth rate to recover after the overload was 670 µm for the a_{OL}=1.81 mm and 470 µm for the a_{OL}=6.02. Hence, R_d was found to be inversely proportional to the crack length at the time of overload. Similar trend was observed in the specimen OL_20, as shown in Figure. 3.2b, where the R_d for a_{OL}= 1.67 mm was 670 µm, whereas for a_{OL}= 5.7 mm it was 437 µm. This trend of decreasing R_d with increasing a_{OL} is the exact opposite of what is observed for cases with overloads of same R_{OL} (=1.75) but a BR=1 (Figure. 3.2c). From Fig 3.2c it can be seen that when an overload of BR=1 occurs at an a_{OL}= 3.77 mm, the R_d= 390 µm, whereas when the a_{OL}= 16.3 mm, the R_d= 660 µm. The crack propagation trends exhibited by the specimens tested with overloads of BR=0.5 show attributes of mode-mixity induced crack closure, since the contribution of mode-II stresses from the overload causes sliding of crack flanks, resulting in roughness induced crack closure. As the crack-tip opening displacement is lesser at smaller crack lengths, the roughness induced crack closure is much more pronounced since larger areas of the crack flanks come in contact due to the mixed-mode overload (BR≠1). The sliding of the crack flanks can cause tangential displacement of the crack asperities and can lead to interlocking of the crack faces in the regions that are in contact. This can explain the higher crack retardation effect and longer R_d for shorter cracks as compared to long cracks. This also points to an interesting phenomenon that smaller cracks experience higher retardation effects under mixed-mode overloads of M_{OL} even as low as π/8, than under pure mode-I overloads. Whereas longer cracks are less sensitive to mixed-mode overloads and highly sensitive to pure mode-I overloads. This shows that plasticity induced crack closure caused by the mode-I component of the loading contributes significantly in the retardation of longer cracks. For shorter cracks, roughness induced crack closure due to the mode-II component of the loading governs the crack retardation behavior. Table 3.2 shows the results from the fatigue tests with overloads of BR=0.5 and R_{OL}=1.75.

Table 3.2: Biaxial fatigue tests with R_{OL} =1.75 and BR=0.5

Test ID	**a_{OL} (mm)**	**P_{max} (kN)**	**BR_{OL} ($P_{Y,OL}$/ $P_{X,OL}$)**	**$P_{Y,OL}$ (kN)**	**$P_{X,OL}$ (kN)**	**R_{OL} (P_{OL}/ P_{max})**	**Rd (μm)**
OL_T20	1.67	15	0.5	26.25	13.125	**1.75**	670
OL_T19	1.81	15	0.5	26.25	13.125	**1.75**	670
OL_T21	3.86	15	0.5	26.25	13.125	**1.75**	634
OL_T20	5.7	15	0.5	26.25	13.125	**1.75**	437
OL_T19	6.02	15	0.5	26.25	13.125	**1.75**	410
OL_25	6.28	15	0.5	26.25	13.125	**1.75**	440
OL_33	10.31	15	0.5	26.25	13.125	**1.75**	355
OL_T21	16.84	15	0.5	26.25	13.125	**1.75**	294
OL_25	27.45	15	0.5	26.25	13.125	**1.75**	290

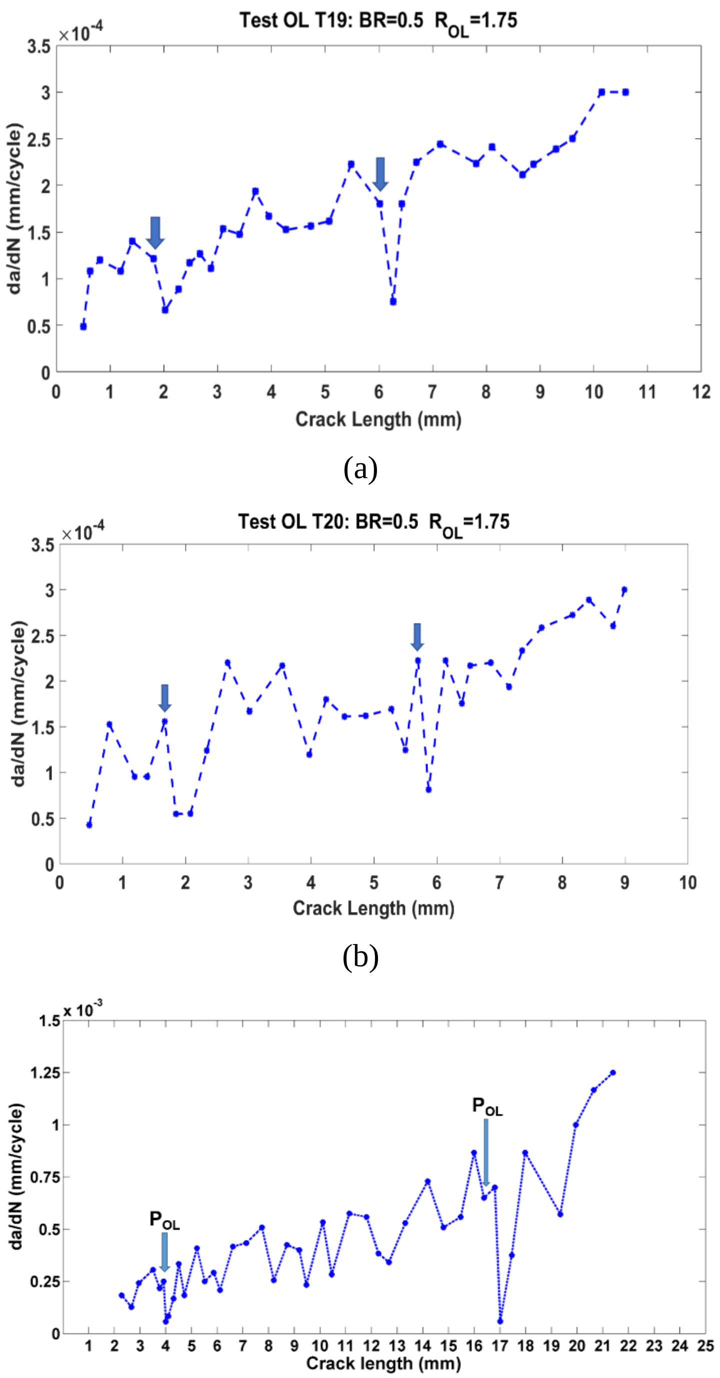

(a)

(b)

(c)

Figure 3.2: Crack growth rate vs crack length for: (a) specimen OL_19; (b) specimen OL_20 and; (c) specimen tested with overloads of ROL=1.75 with BR=1, for comparison

From Table 3.2 it can be noted that the R_d reduces consistently with increasing a_{OL}, indicating the reduced contributions of mode-mixity induced crack closure to crack retardation at higher crack lengths. To study the influence of magnitude of the mixed-mode overloads with BR=0.5, fatigue tests were conducted with R_{OL}=2.0 and 2.5 as summarized in Table 3.3. Figure 3.3a shows the load spectra used for OL_T22 tested with R_{OL}=2.0 and BR of 0.5. Figure 3.3b and 3.3c show the crack growth rate as function of crack length for OL_T22 and OL_T24.

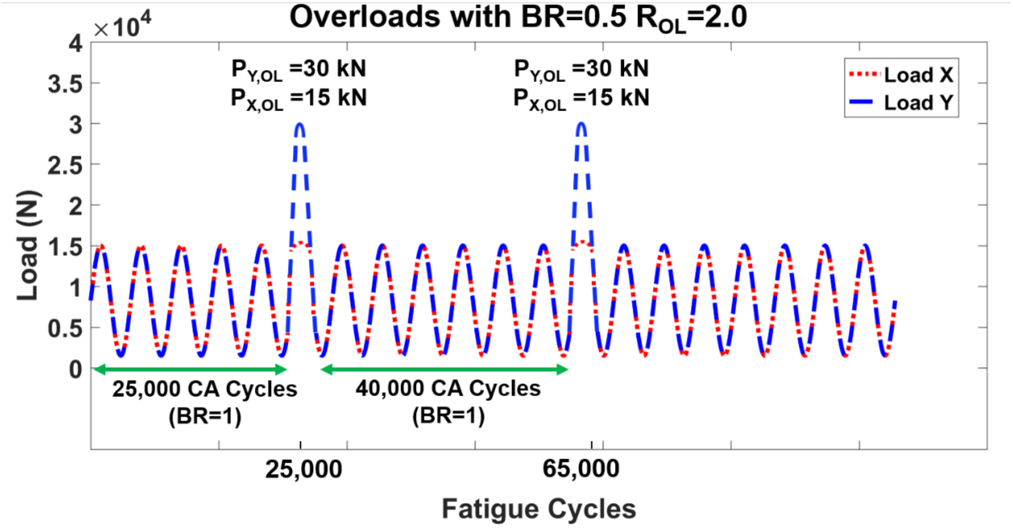

(a)

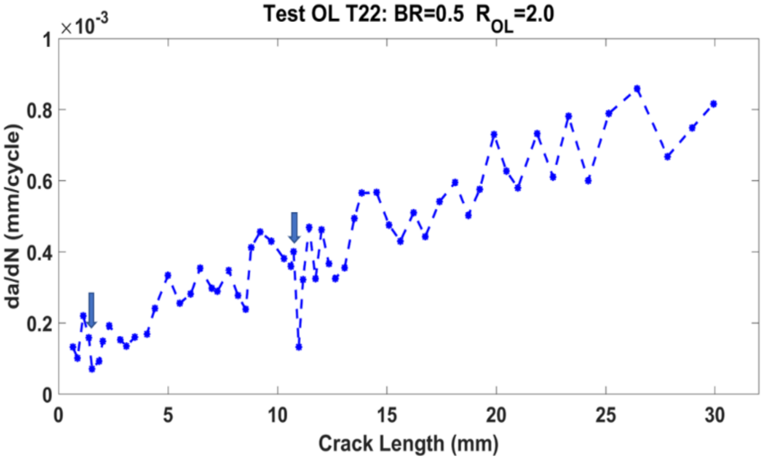

(b)

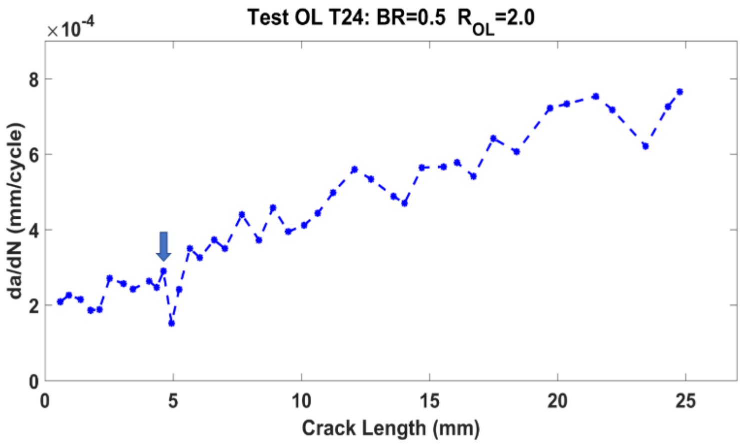

(c)

Figure 3.3: Crack growth rate vs crack length for specimens tested with ROL=2.0 with BRs of 0.5

Figure 3.4 shows the crack growth rate as a function of crack length for specimens tested with R_{OL}=2.5 with BR of 0.5.

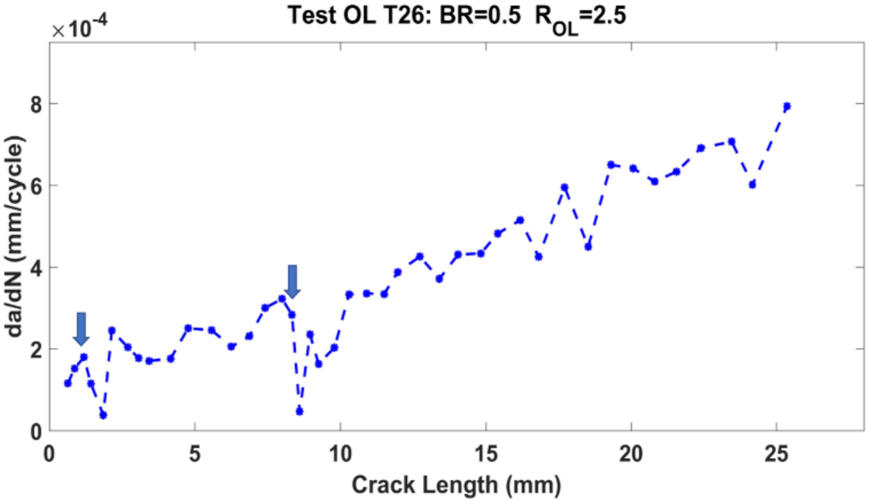

(a)

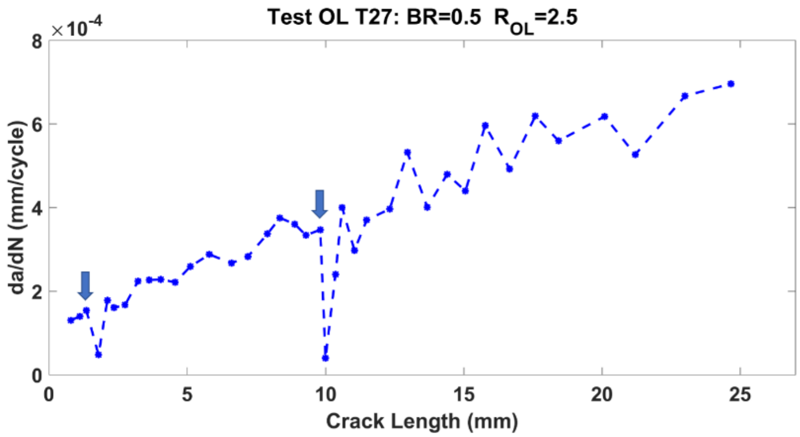

(b)

Figure 3.4: Crack growth rate vs crack length for specimens tested with R_{OL}=2.5 with BRs of 0.5

Table 3.3: Biaxial fatigue tests with R_{OL} =2.0 and 2.5 with BR=0.5

Test ID	**a_{OL} (mm)**	**P_{max} (kN)**	**BR_{OL} ($P_{Y,OL}$/ $P_{X,OL}$)**	**R_{OL} (P_{OL}/ P_{max})**	**$P_{Y,OL}$ (kN)**	**$P_{X,OL}$ (kN)**	**R_d (μm)**
OL_22	1.385	15	**0.5**	2.0	30	15	696
OL_23	4.22	15	**0.5**	2.0	30	15	650
OL_24	4.62	15	**0.5**	2.0	30	15	610
OL_22	10.74	15	**0.5**	2.0	30	15	430
OL_T27	1.35	15	**0.5**	2.5	37.5	18.75	760
OL_T26	1.43	15	**0.5**	2.5	37.5	18.75	770
OL_T32	4.12	15	**0.5**	2.5	37.5	18.75	710
OL_T26	8.34	15	**0.5**	2.5	37.5	18.75	619
OL_T27	9.81	15	**0.5**	2.5	37.5	18.75	550

From Table 3.3 and Figure 3.5, it can be observed that the retardation effects increase with the overload magnitude indicating that the mode-mixity induced crack closure increases with overload ratio, however it decreases with a_{OL}.

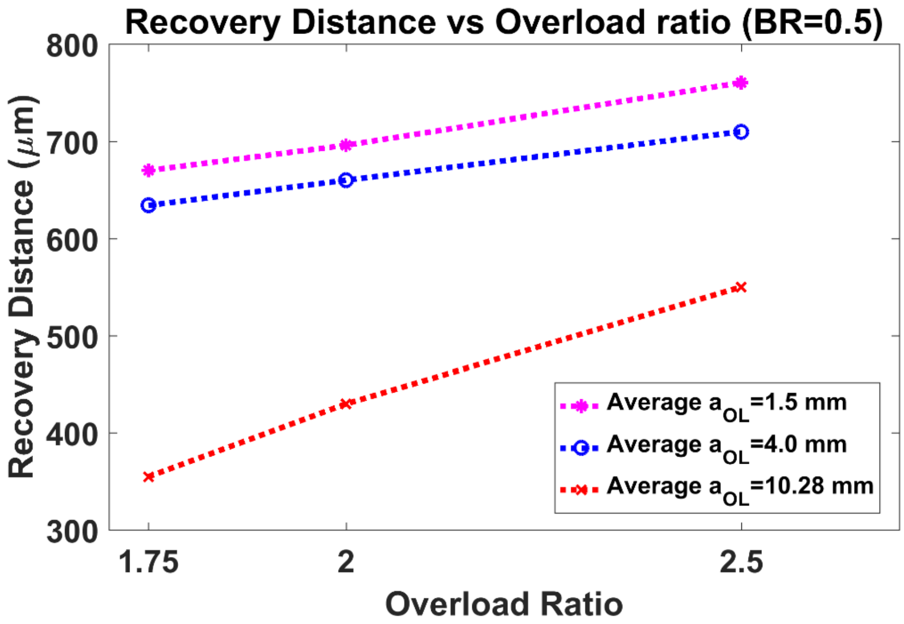

Figure 3.5: Influence of overload ratio on recovery distance at different a_{OL}

Quantitative fractography was conducted on specimens tested with mixed-mode overloads and the macro- and microscale crack growth behavior was investigated in detail. Crack retardation was observed to be higher in the case of smaller crack lengths (< 4mm) along with longer recovery distances as compared to larger crack lengths for the same R_{OL} and BR (when BR≠1). This trend is found to be the opposite of what is observed in the cases with overloads of BR=1. This phenomenon can be attributed to the mode-II induced crack closure mechanisms that arise due to the mixed-mode overload. Due to the mode-II stresses, crack flank sliding and interlocking of crack asperities can take place in the wake of the crack, giving rise to roughness induced crack closure. This results in higher retardation for smaller crack lengths since their crack-tip opening displacements (CTOD) are lesser than those for longer crack lengths. Lesser CTOD allows for higher roughness induced mode-II crack closure effects leading to higher crack retardation.

Figure 3.6 shows the fracture surface morphology at the occurrence of mixed-mode overloads of R_{OL}=2.0 and BR=0.5 in specimen OL_T22. In Figure 3.6a, the yellow arrow indicates the overload line formed on the fracture surface when the first overload occurred at a crack length of 1.385 mm and the corresponding R_d= 696μm. The encircled region shows fracture morphology that indicates interlocking of the crack asperities of the crack flanks in the wake of the crack-tip, due to the mode-II component of the overload. Wear debris, abrasion marks and tangentially displaced crack asperities can be observed in the wake of the crack-tip in Figure 3.6b and 3.6c, indicating severe roughness induced crack closure. Figure 3.6d shows annihilated striations in the wake of the crack-tip caused due to crack flank sliding under the influence of mode-II component of the overload. Significant change in the shape of the crack front can be seen to occur due to the occurrence of the overload (see Figure 3.6e and 3.6f). Shearing marks and crack asperities can be observed to extend ahead of the overload line, and the jagged morphology points towards continued roughness induced crack closure effects in the retardation region. The length of the zone with roughness induced closure morphology ahead of the overload line was found to be approximately equal to the recovery distance (695μm) as shown in Figure 9e. Hence, the crack retardation behavior for short cracks under the influence of mixed-mode overloads of M_{OL}=π/8 (BR=0.5) is dominated by roughness induced crack closure and change in the shape of the crack front.

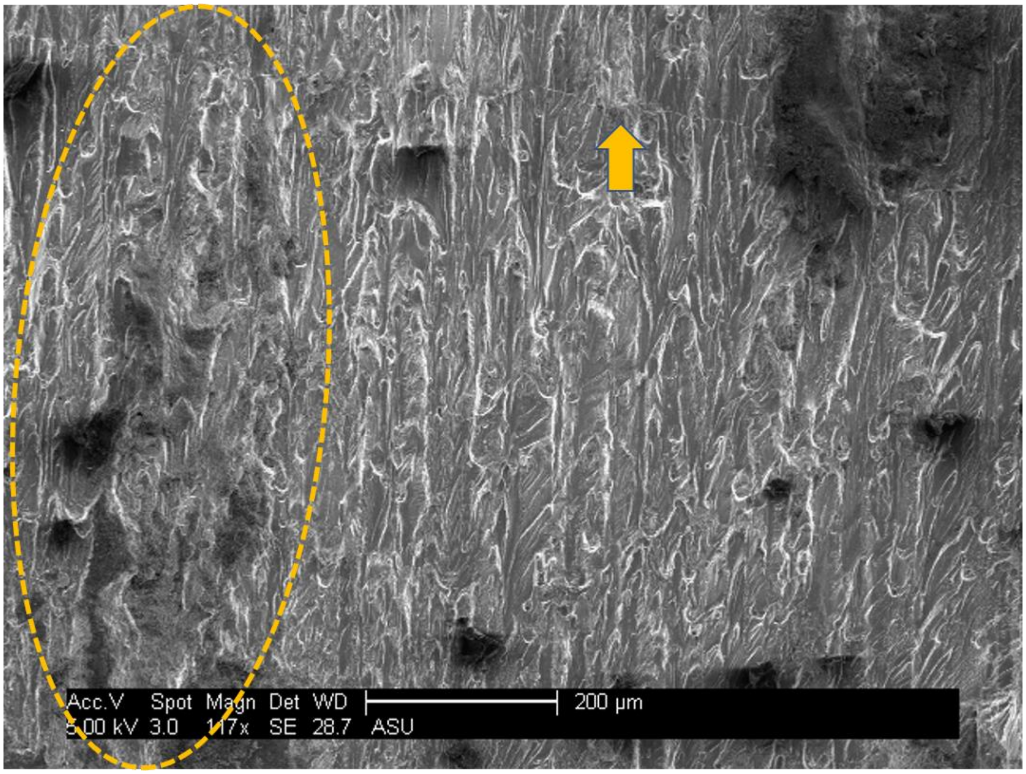
Acc.V Spot Magn Det WD 200 µm
5.00 kV 3.0 117x SE 28.7 ASU

(a)

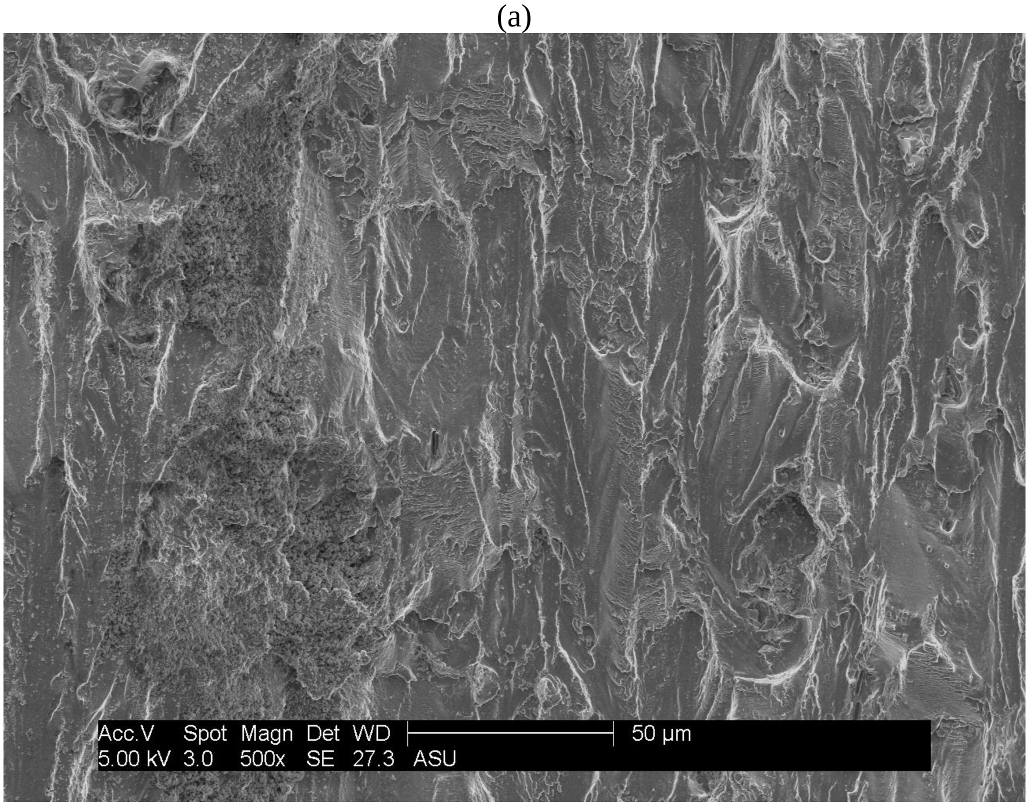
Acc.V Spot Magn Det WD 50 µm
5.00 kV 3.0 500x SE 27.3 ASU

(b)

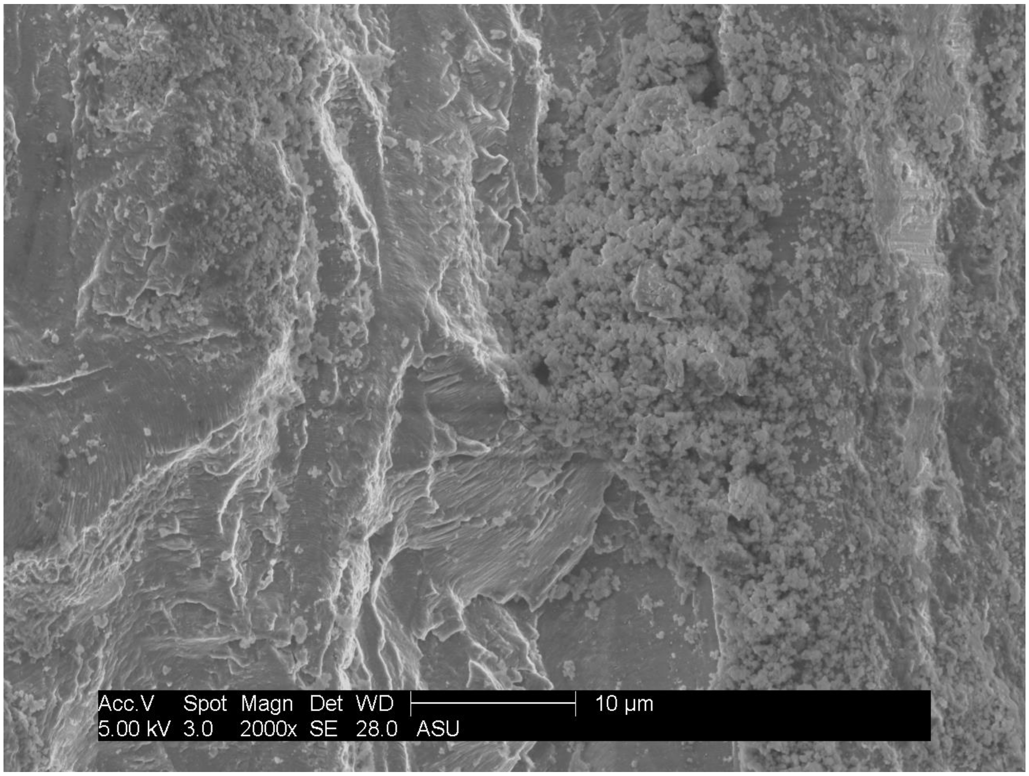
Acc.V Spot Magn Det WD
10 µm
5.00 kV 3.0 2000x SE 28.0 ASU

(c)

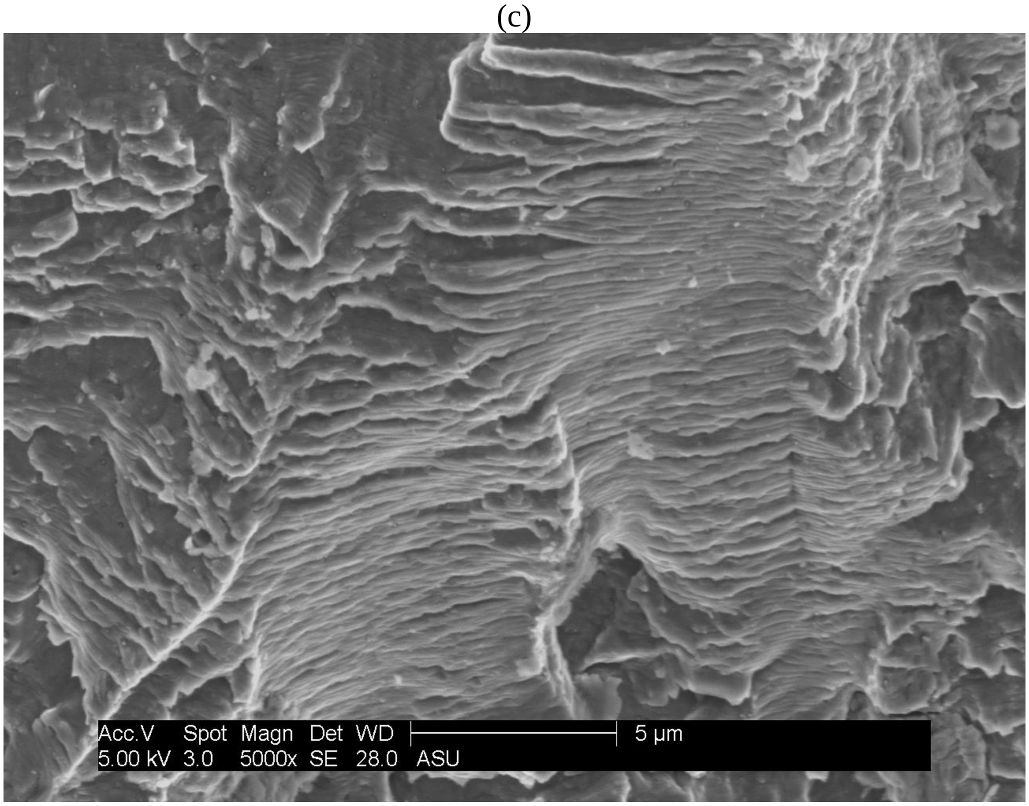
Acc.V Spot Magn Det WD
5 µm
5.00 kV 3.0 5000x SE 28.0 ASU

(d)

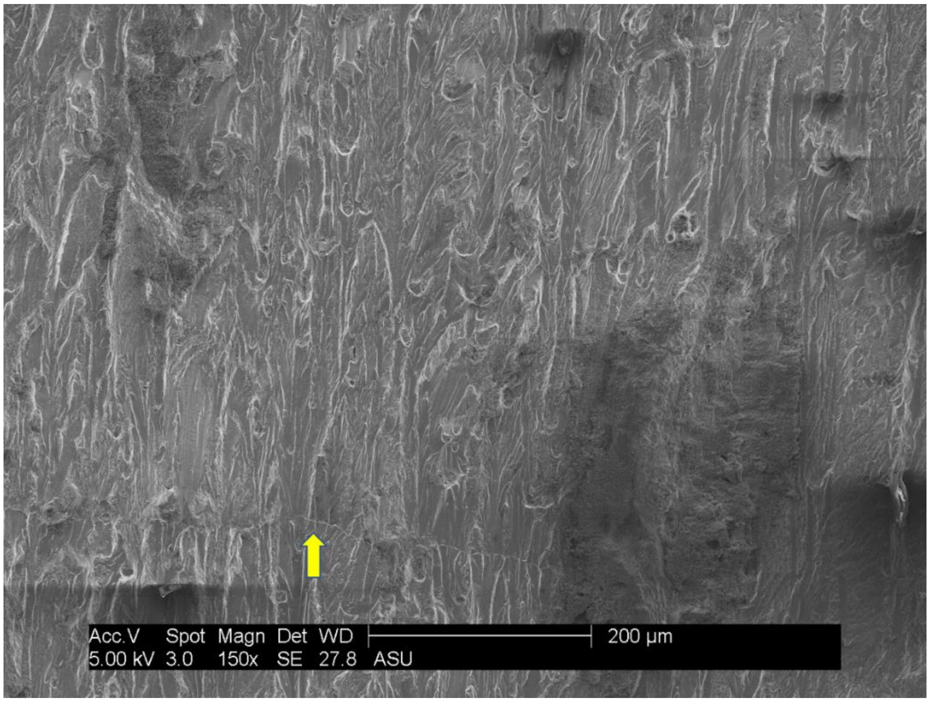

(e)

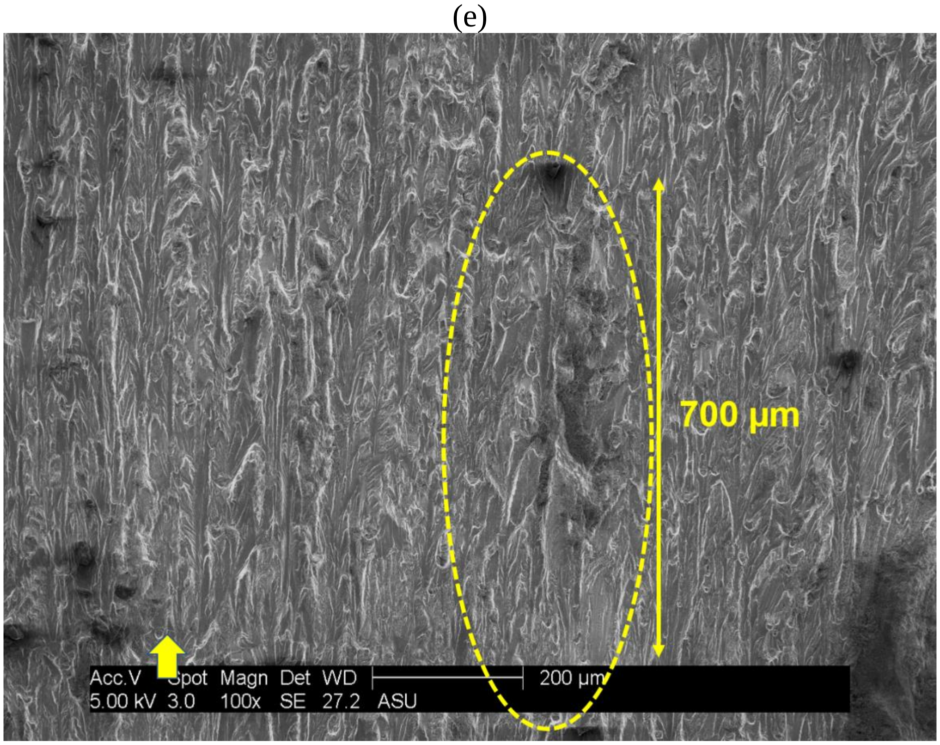

(f)

Figure 3.6. Fracture surface morphology of specimen OL_T22 in region of first overload at a_{OL}=1.38 mm

3.3.2 Overloads of Biaxiality Ratio 0.75

Load spectrum containing two single overloads of R_{OL}=1.75 and BR=0.75 (M_{OL}=π/18) after 35000 and 65000 fatigue cycles is shown in Figure 3.7. The crack length as a function of fatigue cycles for two specimens (OL_T31 and OL_T32) tested with this load spectrum is presented in Figure 3.8. The crack growth rate after the first overload at 35000 cycles was seen to reduce drastically, and gradually recovered over the next 6400 cycles for specimen OL_31 and 5700 cycles for OL_32. For the crack retardation observed after second overload at 65000 fatigue cycles, the crack growth rate recovered in 3100 cycles for specimen OL_31, and 4200 cycles for specimen OL_32. This indicates that the retardation effects caused by single overloads of BR=0.75 recover relatively faster for longer cracks, as compared to shorter cracks. This trend is consistent with the specimens tested with overloads of BR=0.5 but is opposite of what is observed in the case of overloads of BR=1.

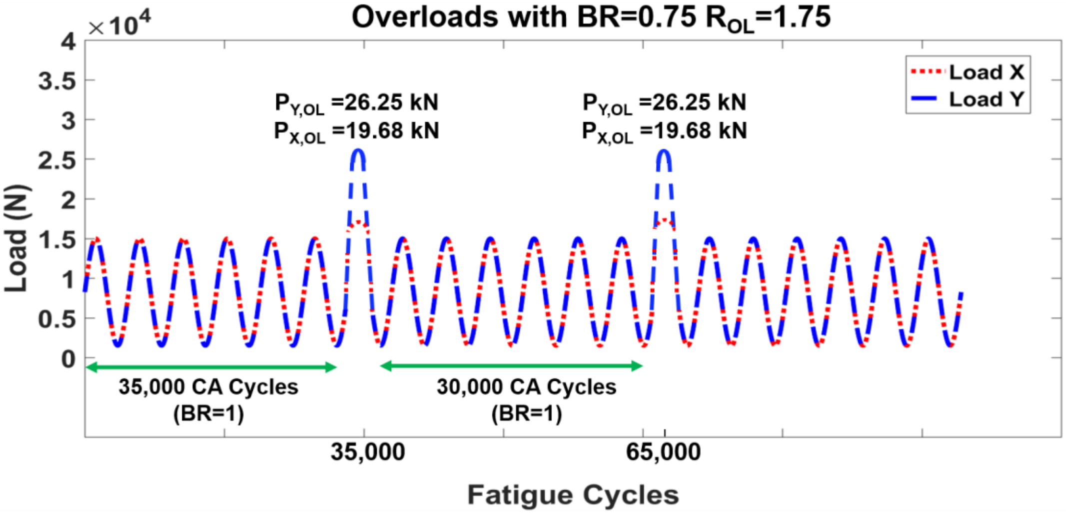

Figure 3.7: Load spectrum with single overloads of ROL=1.75 and BR=0.75 at 35,000 and 65,000 fatigue cycles

Figure 3.9a and 3.9b show the crack growth rates as a function of crack length for specimens OL_31 and OL_32, respectively. From Figure 3.9, it can be seen that an immediate reduction in the crack growth rate occurs after the excursion of individual overloads of BR=0.75. As representative of the tests conducted with overloads of BR=0.75, specimens OL_T29 and OL_T32 are further discussed in detail, since experimental data for comparison with BR=0.5 and 1.0 is available for approximately the same overload crack lengths. For the specimen OL_29, the first overload occurred at a crack length (a_{OL}) of 1.81 mm and the second overload occurred at an a_{OL} of 5.45 mm. The R_d propagated by the crack-tip for crack growth rate to recover after the overload was 540 µm for the a_{OL}=1.81 mm and 480 µm for the a_{OL}=5.45 mm. Hence, R_d was found to be inversely proportional to the crack length at the time of overload. Similar trend was observed in the specimen OL_32, as shown in Figure. 3.2b, where the R_d for a_{OL}= 3.49 mm was 500 µm, whereas for a_{OL}= 10.98 mm it was 360 µm.

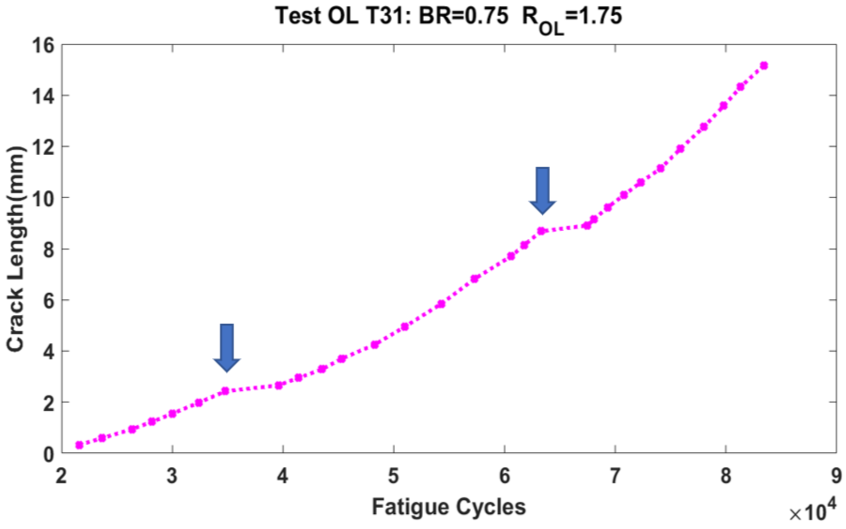

(a)

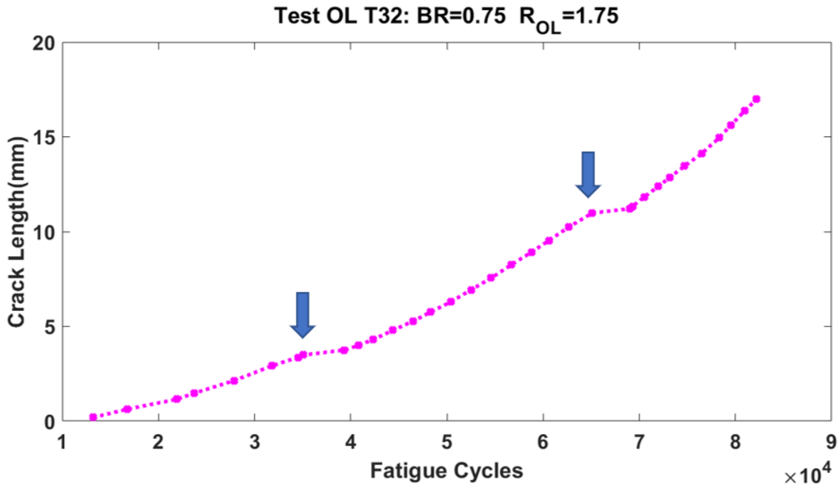

(b)

Figure 3.8: Crack length vs fatigue cycles for (a) specimen OL_31; (b) specimen OL_T32

The crack propagation trends exhibited by the specimens tested with overloads of BR=0.75 also show attributes of mode-mixity induced crack closure, since overloads at shorter crack lengths resulted in larger R_d values. However, the R_d in the case of overloads of BR=0.75 were lesser than those for BR=0.5 for shorter cracks, but approximately the same for longer cracks (compare Table 3.2 and 3.4).

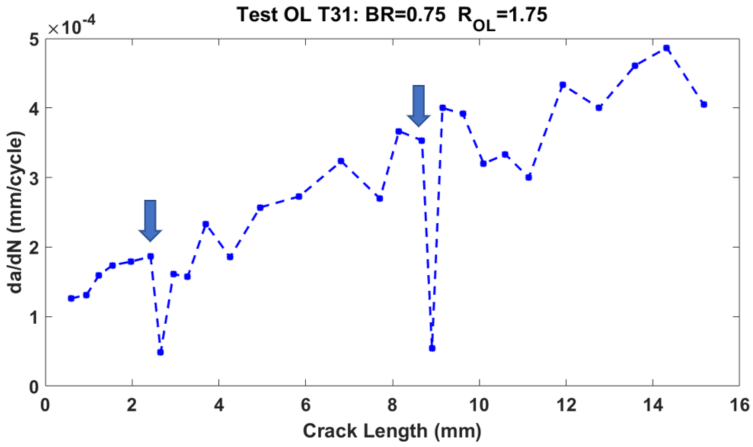

(a)

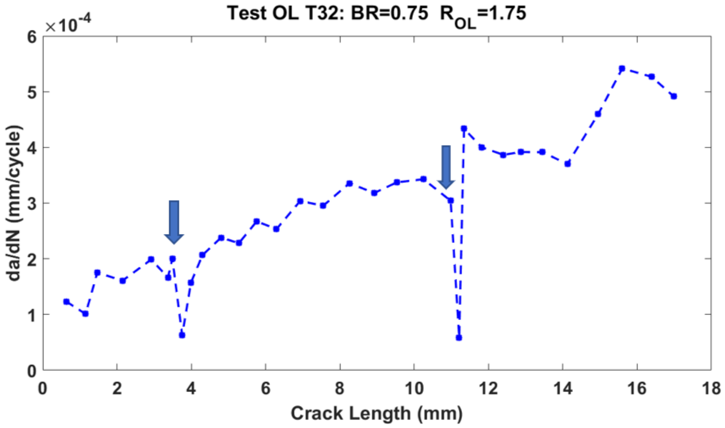

(b)

Figure 3.9: Fatigue crack growth rate vs crack length for (a) specimen OL_T31 and (b) specimen OL_T32

Table 3.4 presents the test results for specimens tested with overloads of BR=0.75. The trends for recovery distance as a function of instantaneous crack length at overload (a_{OL}) is presented in Figure 3.10 for overloads of R_{OL}=1.75 with BRs of 0.5, 0.75 and 1, for a direct comparison.

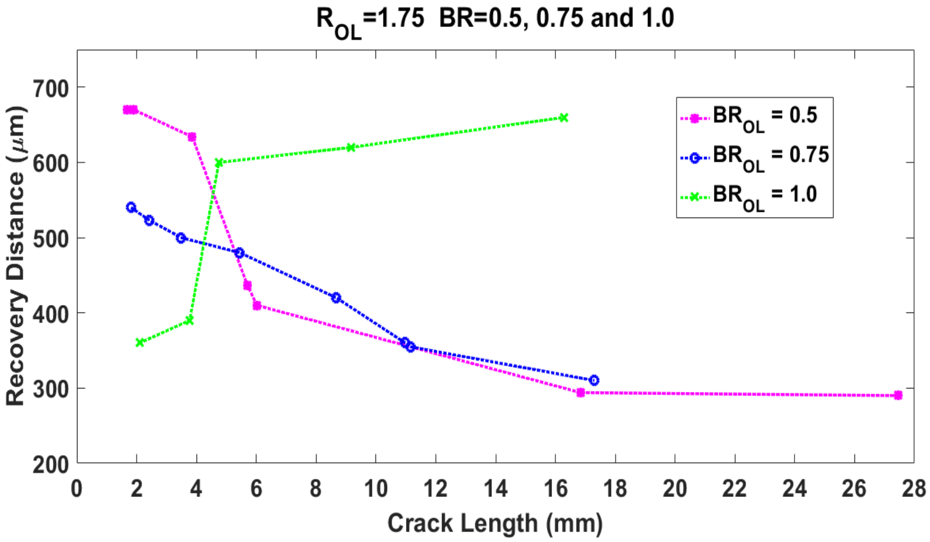

Figure 3.10: Recovery distance as function of overload crack length for overloads of BR=0.5, 0.75 and 1.0

For cracks longer than approximately 4 mm, the overloads of BR=0.5 exhibit an abrupt decrease in retardation effects, whereas for BR=1.0, there is an abrupt increase in the retardation effects. This indicates that the overload mode-mixity $M_{OL}=\pi/8$ causes significant roughness induced crack closure in the short-crack regime, and the pure mode-I overloads cause noticeable plasticity induced crack closure in the long-crack regime. It is interesting to note that, for overloads of BR=0.75 ($M_{OL}=\pi/18$), the retardation is lesser than in the case of BR=0.5 ($M_{OL}=\pi/8$) for shorter cracks (a_{OL}<4mm). This can be attributed to higher mode-II component in overloads of BR=0.5, that dominates crack growth for a_{OL}<4mm. However, for higher crack lengths (a_{OL}>4mm), the retardation effects of BR=0.75 and BR=0.5 last for approximately the same R_d, indicating that the plasticity induced crack closure due to mode-I component of the BR=0.75 overloads starts to increasingly contribute to the retardation effects as the crack length increases, since $K_{I,OL}$ is higher for BR=0.75 than BR=0.5. Another important observation to note is that the retardation effects for overloads of BR=0.75 reduce gradually with increasing a_{OL}, unlike the abrupt drop in R_d seen in the case of BR=0.5 and 1.0. This can be attributed to the gradually decreasing contribution of mode-II induced crack closure and steadily increasing contribution of mode-I plasticity induced crack closure as the a_{OL} increases.

Table 3.4: Biaxial fatigue tests with single overloads of R_{OL}=1.75 and BR=0.75

Test ID	**a_{OL} (mm)**	**P_{max} (kN)**	**BR_{OL} ($P_{Y,OL}$/ $P_{X,OL}$)**	**R_{OL} (P_{OL}/ P_{max})**	**$P_{Y,OL}$ (kN)**	**$P_{X,OL}$ (kN)**	**R_d (μm)**
OL_T29	**1.81**	15	**0.75**	1.75	26.25	19.68	**540**
OL_T31	**2.43**	15	**0.75**	1.75	26.25	19.68	**523**

OL_T32	**3.49**	15	**0.75**	1.75	26.25	19.68	**500**
OL_T29	**5.45**	15	**0.75**	1.75	26.25	19.68	**480**
OL_T31	**8.68**	15	**0.75**	1.75	26.25	19.68	**420**
OL_T32	**10.98**	15	**0.75**	1.75	26.25	19.68	**360**
OL_T30	**11.15**	15	**0.75**	1.75	26.25	19.68	**355**
OL_T33	**17.3**	15	**0.75**	1.75	26.25	19.68	**310**

3.4 Summary

Biaxial fatigue tests with single mixed-mode overloads of BR = 0.5 and 0.75 were conducted and their influence on crack retardation behavior at different overload crack lengths was investigated in detail. The mode-mixity parameter (M_{OL}) was calculated to be π/8 and π/18 for BR=0.5 and 0.75 respectively. The crack growth data showed immediate reduction in the crack growth rate following the occurrence of a mixed-mode overload, with gradual recovery as the crack-tip propagated out of the overload affected region. Even though the M_{OL} for overloads of BR=0.5 and 0.75 were significantly lower than for the case of pure mode-II (M_{OL}=π/2), mode-II induced crack closure effects on crack growth were noticeable. The shorter cracks when subjected to a single mixed-mode overload exhibited higher crack retardation compared to longer cracks, indicating the roughness induced crack closure phenomenon caused by the mode-II component of the mixed-mode overload.

The R_d as a function of a_{OL} for tests with single overloads of BR=0.5 showed a drastic decrease in R_d for a_{OL} > 4mm, indicating that the retardation effects induced by mode-II component of the overloads were highly dominant for short cracks but not as significant once the crack length reached and extended past approximately 4mm. This also suggests that mode-I plasticity induced crack closure did not play a significant role in the case of BR=0.5 since the R_d continues to decrease with increasing a_{OL}. For the case of BR=0.75, the decrease in R_d with increasing a_{OL} was found to be more gradual, as the contribution of mode-I plasticity induced crack closure steadily increased with a_{OL} as the mode-II induced closure effects gradually decreased.

4 FABRICATION AND CHARACTERIZATION OF SIZABLE BUCKYPAPER MEMBRANES

4.1 Introduction

The efficient fabrication of large CNT buckypapers is essential to the development of multifunctional composite materials for structural scale aerospace applications. As discussed in Chapter 1, the challenges associated with fabrication of buckypapers using the conventional methods such as vacuum filtration lead to unreasonably long processing times, CNT dispersion issues and smaller buckypaper membranes. Hence, preparing suitably sized buckypaper-embedded FRPs for fatigue investigations and development of *in-situ* damage quantification methodologies has not been feasible thus far. A rapid and cost-effective method for manufacturing buckypapers can provide the opportunity to effectively research and develop superior multifunctional composite materials.

In this chapter, a novel fabrication method is presented that facilitates the production of significantly larger CNT buckypapers than what is possible with most current manufacturing techniques. The thickness of the membranes can be controlled ranging from 70 µm to 1300 µm. This method does not require the use of surfactant-assisted dispersion, chemical functionalization or the use of any filtration technique. Hence processing time could be reduced by approximately 6-8 times depending upon the size of buckypaper membrane being fabricated. Unlike the current technique where some fraction of CNTs passed through the filtration membrane, there is negligible wastage of CNTs in the proposed method. This technique provides the potential to advance buckypaper from laboratory scale demonstrations to structural scale applications since there is no size limitation on the buckypaper membrane. Various properties of the buckypaper membranes such as microstructure, structural homogeneity, electrical conductivity, Brunauer Emmett and Teller (BET) specific surface area (SSA) and pore size distribution were investigated. Furthermore, epoxy infused buckypaper nanocomposites were fabricated and the through-thickness resin penetration and CNT wettability were qualitatively characterized using SEM. Good resin impregnation is important for strong interfacial adhesion between CNTs and host matrix, ensuring efficient load transfer to the multifunctional nano-reinforcement. Stronger interaction between constituent CNTs of the buckypaper and host matrix also leads to higher piezoresistive sensitivity, enabling real-time strain sensing.

This chapter is organized as follows. First, the fabrication process and processing parameters for CNT buckypapers is explained in detail. Detailed characterization of the nanostructure of as-fabricated buckypaper, along with the electrical properties are presented next. Finally, the fabrication method and resin penetration quality for epoxy-infused buckypaper nanocomposite films is discussed, and their mechanical properties are compared with pure-epoxy and CNT-dispersed epoxy films.

4.2 Novel Slurry Compression Fabrication Process for Sizable Buckypapers

Multi-walled carbon nanotubes used in this research were obtained from US Research Nanomaterials Inc. produced using the Chemical Vapor Deposition (CVD) technique. Purity of the MWNTs was confirmed to be 90% as claimed by the supplier. The dimensions and properties of the MWNTs are summarized in Table 4.1.

Table 4.1: Properties of MWNTs used for manufacturing buckypapers

Outer diameter	10 – 30 nm
Average length	15 – 30 μm
Density	2.1 g/cc
Specific surface area	200 m^2/g
Conductivity	>10^4 S/m

Figure 4.1 shows the schematic steps of the proposed manufacturing technique. A volume of 5 ml of high concentration solution (25 mg/ml) of MWNTs in methanol required to fabricate a buckypaper of approximately 4.4 cm diameter with an average thickness of 200 μm. The high concentration solution was ultrasonicated with a tip-sonicator, leading to the evaporation of methanol solvent, until highly viscous slurry of MWNTs and methanol was obtained. This slurry was stirred with a glass rod to improve homogeneity and laid up for compression between two steel plates. Steel plates were covered with plastic sheets in order to avoid adhesion between the buckypaper and the compression plates. For a buckypaper of approximately 4.4 cm diameter, the slurry was laid down in a circular disc shape with a diameter of approximately 2.5 cm and thickness of approximately 3 mm. A 20-ton hydraulic press was used to compress the slurry into a thin membrane. Compressing the MWNT/methanol slurry into a thin membrane should be performed at a very slow rate to prevent the methanol from gushing out and creating cracks. The two plates sandwiching the membrane are then un-mounted from the press and placed into an oven at 60°C for 1 hour. After drying, the top plate was removed and the free standing MWNT buckypaper was degassed for 24 hours.

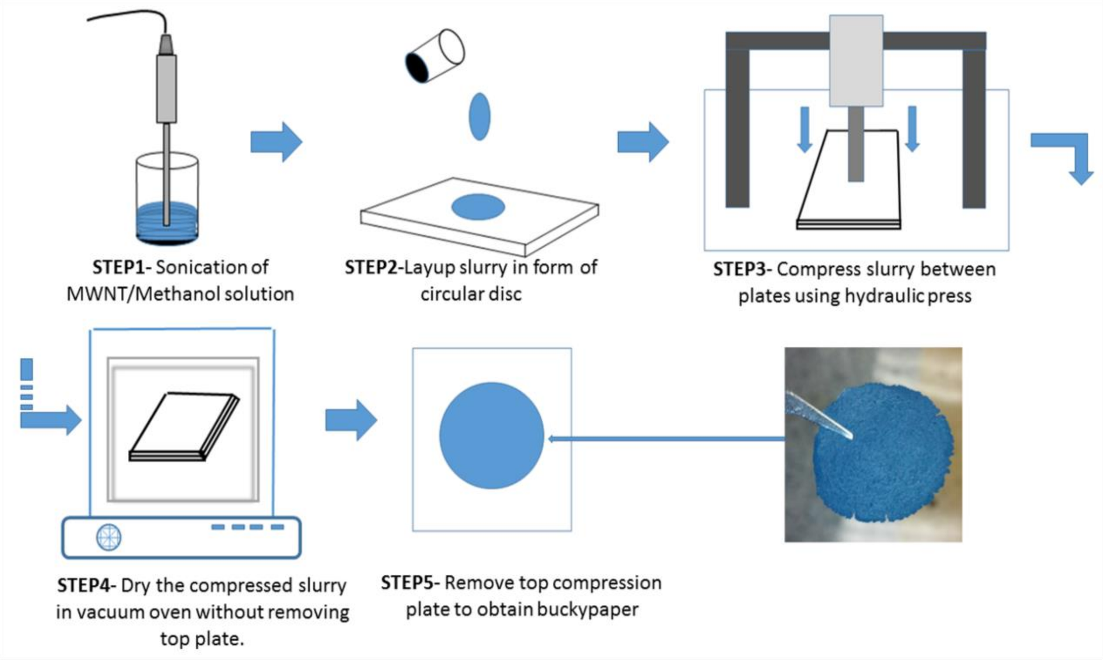

Figure 4.1: Schematic of buckypaper manufacturing process

Once the process was finalized, the capability of this novel fabrication procedure to make larger buckypapers was proven by using a greater quantity of MWNT/methanol slurry for a single buckypaper. The thickness of the buckypaper can be controlled by changing the wetness of the slurry and the load applied by the hydraulic press. Higher methanol content in the slurry reduces the required force for compression, and thinner buckypapers can be obtained with relatively lesser compressing force. The minimum thickness of buckypaper achieved through this fabrication process, with the hydraulic press loaded to full capacity, was approximately 70 μm. Figure 4.2 shows a large size (20 cm x 16 cm) free-standing buckypaper with stable structure and smooth surface finish fabricated by scaling up the quantity of MWNT/methanol during fabrication.

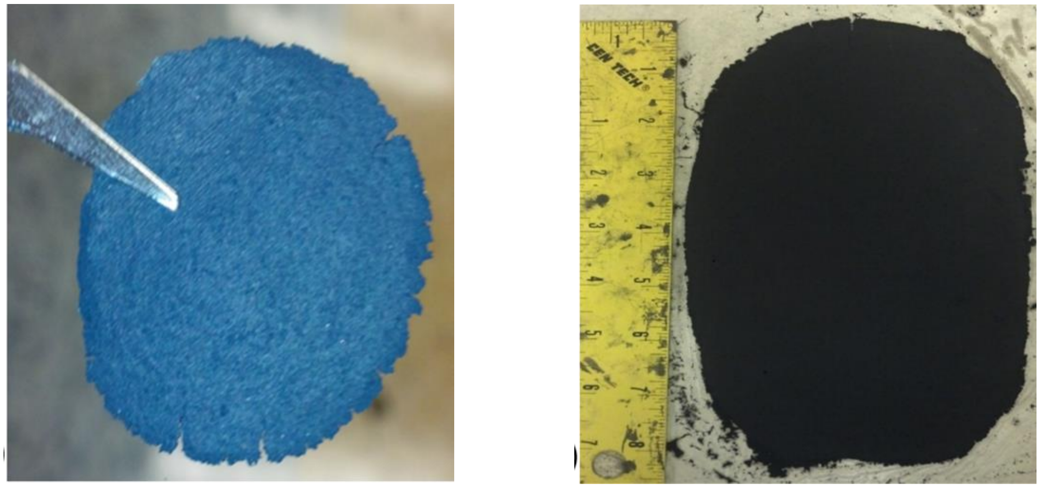

(a) (b)

Figure 4.2: (a) Free standing buckypaper lifted off the compression plate; (b) 20 cm x 16 cm buckypaper manufactured by scaling up quantity of methanol/MWNT slurry

4.3 Structure-Property Characterization of Buckypapers

Buckypapers fabricated from the slurry compression method showed uniform thickness and a robust structure with an average density of 0.42 g/cc which is close to density of buckypapers fabricated by vacuum filtration technique (Chih-Yen 2005; Zhang J., and Jiang D. 2012). Qualitative analysis of buckypapers made using this novel method was carried out using a JEOL XL-30 scanning electron microscope (SEM). Morphology and surface quality of the buckypapers were analyzed from SEM scans starting with low magnification and progressing to higher magnification levels. SEM micrographs of buckypaper cross-section were obtained at different locations along the width to determine the degree of uniformity in thickness.

Figure 4.3(a) is a low magnification SEM image (15000x) showing a uniform, crack free and stable structure composed of highly entangled MWNTs. Uniformly distributed and randomly oriented MWNT bundles and the absence of large voids (Figure 4.3a and 4.3b) suggest homogeneity in microstructure and isotropic material properties. Mainly two types of pores were observed in the SEM micrographs of buckypaper and are marked with black and white arrows in Figure 4.3c. The first type is the intra-bundle pores (marked with black arrows) that are present within a CNT bundle. The second type is of the inter-bundle pores (marked with white arrows) present between CNT bundles. The uniformity in thickness evaluated using SEM micrographs of buckypaper cross-section is depicted in Figure 4.4. Average and standard deviation of thickness of the membrane shown in Figure. 4.4 was found to be 242.06 µm and 7.86 µm, respectively.

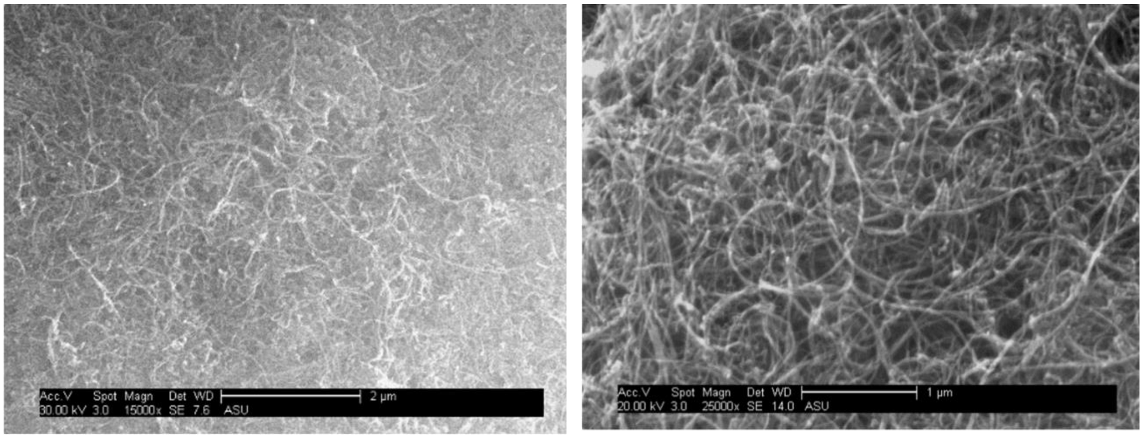

(a) (b)

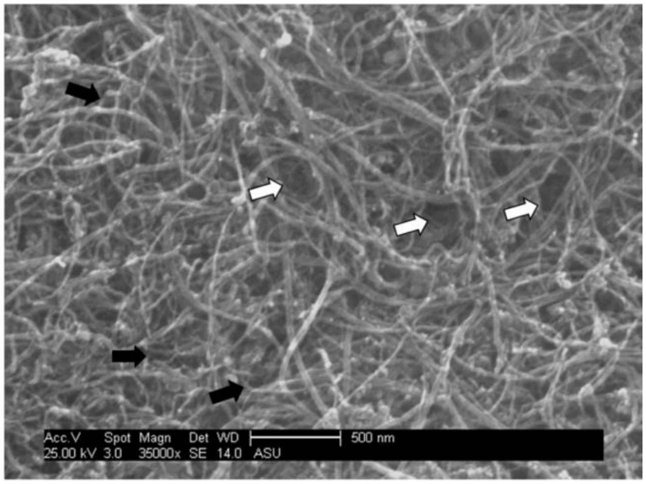

(c)

Figure 4.3: SEM micrographs for Buckypaper at (a) 15000×; (b) 25000×; and (c) 35000× showing inter-bundle and intra-bundle pores

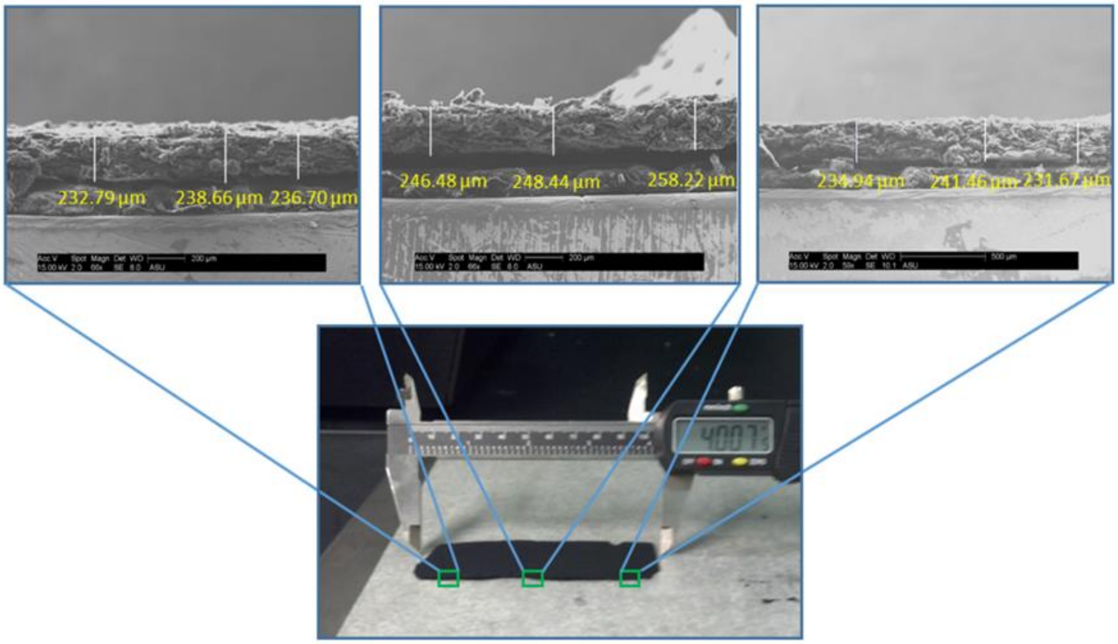

Figure 4.4: Uniformity in thickness across the width of 4-inch wide buckypaper specimen

N2 adsorption-desorption isotherms were collected at 77K using a Micrometrics Tristar II 3020 surface area and porosity analyzer. SSA was obtained by BET technique whereas the pore-size distribution and cumulative pore content were obtained by Barrett-Joyner-Halenda (BJH) method. The BET SSA as obtained from N2 adsorption isotherms of six different samples of buckypaper was found to be in the range of 94.62 - 107.20 m2/g with the average value of 102.60 m2/g. Bearing in mind that the SSA of CNTs in their original powder form was 200 m2/g, it can be observed that high SSA was retained in the buckypaper form. High SSA is a desirable property for a variety of applications such as fuel cell electrodes, gas/vapor sensing, catalyst, water purification and high weight fraction nanocomposites (Lopes et al. 2010). Pore size distribution obtained from BJH analysis for the buckypaper specimen with maximum SSA of 107.20 m2/g is presented in Figure 4.5.

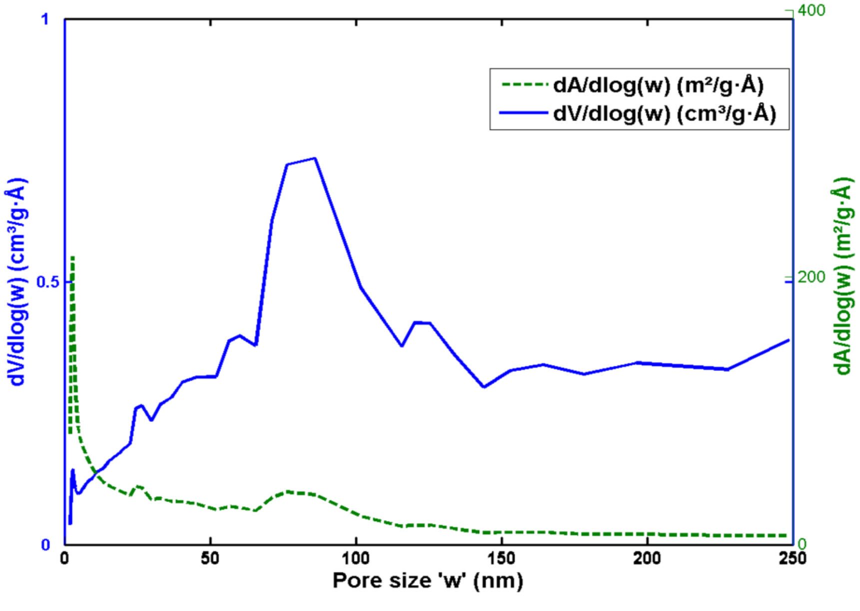

Figure 4.5: (Solid blue) Pore size distribution as derivative plot of pore volume with respect to pore width versus pore width, and (Dashed green) Surface area distribution as derivative plot of surface area with respect to pore width versus pore width

This plot is useful for comparing the relative pore volumes between pore size range as the apparent area under the curve is directly proportional to the real volume being occupied by pores in that size range. The plot of dV/dlog(W) versus W reveals that pores ranging from 70 nm - 120 nm in size occupy relatively larger volume than the micro- (≈ 1.7 nm - 4 nm), meso- (≈ 10 nm - 40 nm) and large size (120 nm - 250 nm) macropores. The peak observed in the size range of 70 nm - 120 nm represents pores between CNT bundles (i.e., inter-bundle pores). The very local sharp peak corresponding to pore size range of 20 nm - 30 nm is associated with the presence of intra-bundle pores since these pores generally have dimensions close to average CNT diameter (Zhang J., and Jiang D. 2012; Dieze-Pascual et al. 2012). A set of micropores at 1.7 nm - 4 nm were observed in pore volume plots due to inter-tube channels between adjacent MWNTs and smaller intra-bundle pores (Pham et al. 2008). Specific surface area distribution as a function of pore width is also presented in Figure. 4.5. It can be seen from this plot that while the pore volumes are mainly associated with mid-sized macropores, the SSA is dominated by micropores (inter-tube channels and smaller intra-bundle pores) of width 1.7 nm - 4 nm providing an indication of their higher concentration. The total porosity (φ) was calculated from relation (Zhang J., and Jiang D. 2012),

$$\Phi = 1 - \frac{\rho_{BP}}{\rho_{CNT}} \tag{4.1}$$

where ρ_{BP} is the bulk density of buckypaper and ρ_{CNT} is the density of MWNTs (2.1 g/cc). The total porosity was in the range of 76.3% - 84.4% with an average value of 81%.

DC electrical resistance of buckypaper was measured at room temperature with a digital multimeter (Fluke 189), using 2-probe method. 3 cm x 1 cm buckypaper strips were used for conductivity measurements and 0.5 cm at each end was painted with silver paint to form electrodes, leaving 2 cm of effective length in the middle. The DC conductivity (σ) of buckypapers and buckypaper/epoxy films were calculated at room temperature from the following relation (Dieze-Pascual A.M. et al. 2012),

$$\sigma = \frac{L}{AR} \tag{4.2}$$

where L is the effective length of specimen between electrodes, A is its cross-sectional area and R is the measured DC resistance value from the multimeter. The average electrical conductivity of buckypapers was found to be 1.32×10^4 S/m. After being impregnated with epoxy to form the nanocomposite films the conductivity value dropped to 2.12×10^{-4} S/m.

4.4 Fabrication and Mechanical Characterization of Buckypaper/Epoxy Films

Thermoset epoxy resin PRI2002-3-R-A and hardener PRI2000-5-HR-B with a 100/22 weight ratio, provided by PRI Inc. was used in the fabrication of nanocomposites films. For the fabrication of buckypaper/epoxy nanocomposite films with high MWNT content, buckypaper was sandwiched between two rectangular pieces of bleeder cloth and resin was poured over the bleeder cloth surface and spread using a hand layup tool. This layup technique forced the resin through the porous cloth, allowing it to permeate into the porous buckypaper. Both sides of the buckypaper were impregnated using this layup method and specimens were cured for 12 hours at 65°C. It is important to note that the process followed for resin impregnation was not vacuum assisted to avoid any alteration to the buckypaper's MWNT network, since resin penetration under higher pressure can lead to displacement of CNT bundles.

The average thickness for buckypaper/epoxy films was approximately 800 μm. The quality of resin impregnation in buckypaper/epoxy nanocomposites was determined by cross-sectional examination using SEM. Randomly dispersed CNT and pristine specimens were also fabricated for comparison of mechanical properties. A concentration of 1 wt% randomly dispersed MWNT/epoxy were fabricated by first sonicating MWNTs in epoxy using a tip sonicator for 1 hour and stopping at intervals of 10 minutes for manually stirring the mixture with glass rod. The mixture of randomly dispersed MWNTs and epoxy was cast into films by solution casting.

The average thickness of pristine epoxy and MWNT/epoxy films was approximately 500 μm. Tensile tests on the films were conducted using a desktop Test Resources load frame at a displacement rate of 0.0063 mm/s. The strain response of the films under tension was analyzed using DIC system. DIC has been widely used for studying strain fields in various engineering and material science problems (Yekani Fard et al. 2012a, 2012b, 2014a, 2014b; Moerman et al. 2009). As a result of the fabrication procedure, buckypaper/epoxy films with a high MWNT content of 26 - 30 wt% could be obtained. Figure 4.6 shows SEM micrographs of buckypaper/epoxy film cross-sections for the assessment of resin impregnation quality. For comparison, SEM micrographs of neat buckypaper cross-section are also shown in Figure 4.6 to facilitate the evaluation of resin impregnation quality. Areas for analysis were picked from the low magnification cross-sectional image (38x) and are represented by small green boxes.

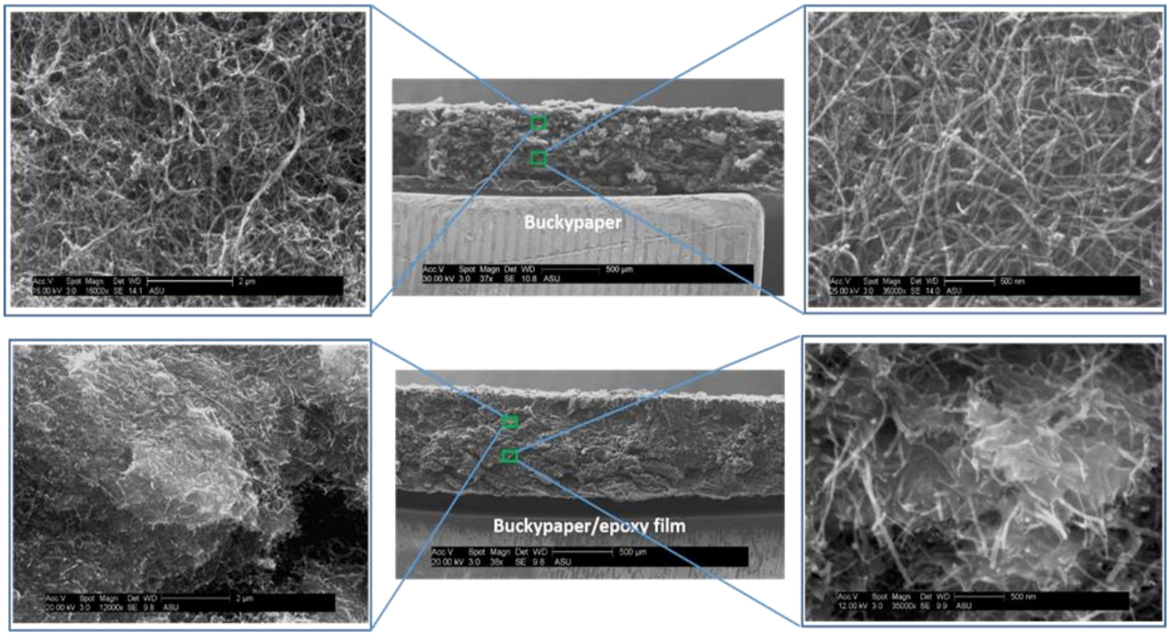

Figure 4.6: Evaluation of through-thickness resin impregnation quality using SEM

High magnification SEM images of buckypaper/epoxy films at different depths from the top surface reveal full penetration of the resin through the thickness of buckypaper and good impregnation quality (Cooper et al. 2003; Whitby et al. 2008). Stress-strain response of polymer films under tensile loading was analyzed in order to better understand the interfacial interaction/adhesion between epoxy resin and the embedded CNTs. Stress-strain curves of representative specimens for pristine and nano-filled epoxy films under tensile loading are shown in Figure 4.7. The average mechanical properties with standard deviations obtained from five specimens are presented in Table 4.2. Strains obtained from DIC were used to plot the stress strain curves in order to analyze mechanical properties accurately.

Buckypaper/epoxy films exhibited 20% greater Young’s modulus when compared to pristine epoxy films. This can be attributed to good resin penetration and strong interfacial interaction between resin and CNTs of the reinforcing buckypaper. Higher Young's modulus indicates that effective stress transfer takes place between epoxy matrix and buckypaper. Average tensile strength in the case of buckypaper/epoxy films was found to be 17% greater than pristine epoxy films suggesting homogeneous and consistent microstructure of buckypaper and good interfacial adhesion between constituent CNTs and resin. Lower modulus in the case of randomly dispersed 1wt% MWNT films can be attributed to non-homogeneous distribution of MWNTs and formation of agglomerations since the use of surfactants and surface functionalization was avoided during the dispersion phase. Regions with agglomerated MWNTs may lack resin and this can lead to decrease in elastic modulus of the films.

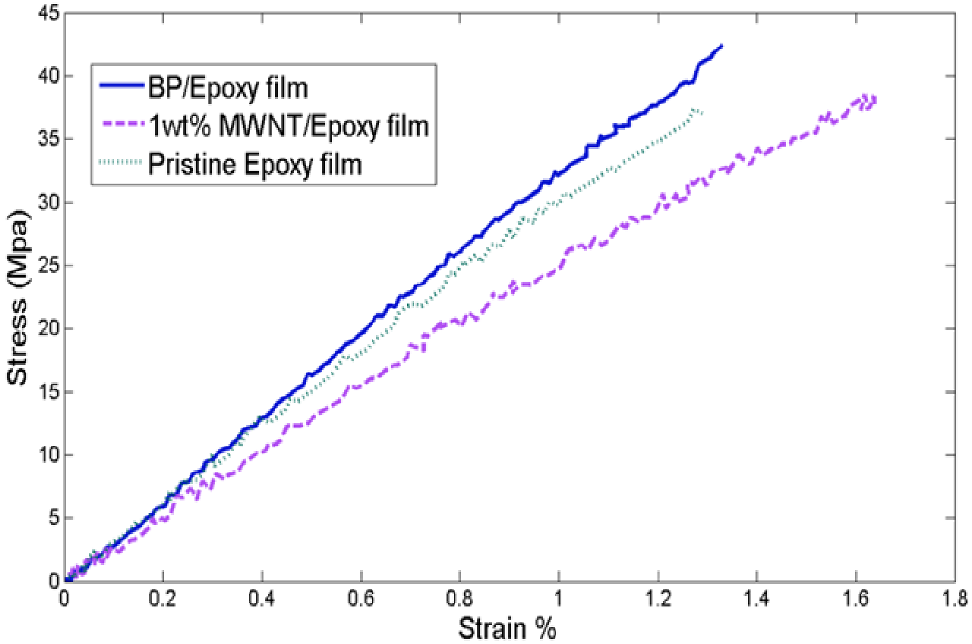

Figure 4.7: Stress-strain curves of polymer films with 0, 1 and 30 wt% MWNTs

Table 4.2: Mechanical properties of pristine, 1wt% MWNT and buckypaper epoxy films

Specimen Description	Wt% of MWNTs	Young's Modulus	Tensile strength
Neat Epoxy film	0	3.01 Gpa	37.08
MWNT/Epoxy film	1	2.72 Gpa	38.60
Buckypaper/Epoxy film	30	3.66 Gpa	45.42

4.5 Summary

The novel fabrication process presented in this chapter enabled the production of good quality, large buckypapers in considerably shorter processing time. Structural homogeneity and stability along with uniformity in thickness was confirmed by SEM analysis. The buckypapers also exhibited high porosity (81%) and SSA (102.6 m^2/g). The density of the buckypapers (0.42g/cc) produced from this manufacturing process was close to buckypapers produced by the vacuum filtration method found in literature. The developed fabrication process also offered control over the thickness of the fabricated buckypapers, and buckypapers ranging from 70 - 1300 µm thickness could be obtained. The nano-porous structure of the buckypapers having high porosity and SSA played a key role in facilitating strong interfacial interaction between the constituent CNTs and the host epoxy matrix when the buckypapers were infused with epoxy polymer. The buckypaper/epoxy nanocomposite exhibited high weight fraction of MWNTs (30 wt%) and complete through-thickness resin impregnation. These films showed an average increase of 20% in tensile modulus and 17% increase in tensile strength, as compared to pristine epoxy films. Thus, the capability to rapidly manufacture larger buckypapers with a high porosity nanostructure and good resin compatibility facilitates the implementation of multifunctional capabilities of CNTs at the industrial scale.

5 BUCKYPAPER EMBEDDED SELF-SENSING GLASS FIBER COMPOSITES FOR IN-SITU STRAIN AND FATIGUE DAMAGE SENSING

5.1 Introduction

Fiber reinforced polymer composites are extensively used in aerospace, automobile and civil applications due to their high specific strength, stiffness and fatigue resistance. Owing to their complex and heterogeneous composition and microstructure, these composite structures are designed to withstand a variety of different fatigue loading conditions. The fatigue damage mechanisms in FRPs are often intricate and can occur in the form of matrix cracking, matrix-fiber debonding, fiber breakage, delamination and fiber pull-out. Hence, monitoring deformation and damage evolution in FRPs has always been a challenging task. In the last two decades, several researchers have proposed structural health monitoring methods for composite structures such as the use of fiber Bragg grating (FBG), passive damage monitoring based on acoustic emission principle using PZT transducer and active damage monitoring and localization based on Lamb wave using at least two PZT transducers (one for actuation and one for sensing). In most of these monitoring methods the sensors are relatively larger than the size of the flaws, and sensor embedment can lead to stress concentrations and creation of potential damage initiation sites. Therefore, to tackle these issues, researchers have focused their attention to the use of CNTs as a multifunctional nanofiller that provides the opportunity for property enhancement, in addition to *in-situ* damage detection through piezoresistive self-sensing. Self-sensing refers to the ability of a structural material to sense its own condition (strain, stress, damage, temperature etc.) in real-time. As discussed in Chapter 1, CNTs have been applied in composite materials by either dispersing them in aligned or random orientations in the host matrix or in the form of membrane architectures such as buckypaper. Several research studies have shown *in-situ* piezoresistive strain and damage sensing using CNTs, however *in-situ* quantification of damage has not been demonstrated in literature. Additionally, these self-sensing composite materials often require complex fabrication methods and efficiently scaling up their size for structural scale applications continues to remain a challenge for researchers.

In this chapter, the development of a novel self-sensing buckypaper embedded glass fiber composite is presented, and the corresponding processing parameters used for the fabrication process are discussed. The buckypapers were embedded in the interlaminar regions of the GFRP laminate during fabrication, and strong interfacial interaction and through-thickness resin penetration was ensured. The piezoresistive response of the self-sensing GFRP (SGFRP) was characterized under monotonic and cyclic loading, and high sensitivity to strain was observed even at small strains. Furthermore, fatigue crack growth behavior of single-edge notched specimens of SGFRPs was investigated under tension-tension fatigue loading while recording the in-situ electrical resistance changes at every crack increment. A measurement model was developed for correlating the electrical resistance readings to instantaneous fatigue crack length, and accurate crack length quantification was accomplished.

This chapter is organized as follows. In Section 5.2.1, details about the materials and fabrication process used for fabricating the SGFRP are discussed in detail, along with relevant schematics. This is followed by detailed explanation of the experimental methods used to demonstrate the *in-situ* strain and damage sensing capability in the SGFRPs. Section 5.2.2 provides results of resistance-based *in-situ* strain and damage quantification, along with the comparison of fatigue crack growth behavior in SGFRP versus baseline-GFRP specimens.

5.2 Fabrication and Experimental Methods for Self-Sensing GFRP

5.2.1 Fabrication Process for Self-Sensing GFRP

The SGFRPs were fabricated using six layers of eight harness satin (8HS) weave of S2 glass fiber from Fibre Glast and thermoset epoxy resin Epon 863 with hardener EPI-CURE 3290 with a 100/27 weight ratio. A wet layup procedure was followed wherein buckypaper, spanning the gauge length of the specimen, was embedded in the center interlaminar layer (between the third and fourth glass fiber layer) of the laminate. The cross-section of the layup is shown in the schematic in Figure 5.1a. Silver adhesive tracks were painted on to the buckypaper surface prior to embedding to avoid the use of invasive electrodes that can often be in the form of embedded wires. Such invasive electrodes can act as hot-spots for damage initiation since they lead to local stress concentrations. The application of silver tracks directly onto the buckypaper also results in high conductivity in the SGFRPs since the contact resistance at the electrode-buckypaper interface is minimized. Following the wet layup procedure, the specimens were cured in a 24-ton hot-press at 150 ˚F for 6 hours. Since the as-formed embedded BP has a porous structure, it’s thickness reduces to approximately 60 – 80 µm after the curing process is complete. Good through thickness resin penetration and impregnation is essential to enable effective load transfer to the buckypaper and allow for efficient real-time strain sensing. The final laminate thickness after curing was approximately 1.5 mm and test specimens (Figure 3.1b) of size 200 mm x 25.4 mm were prepared for mechanical and piezoresistive characterization.

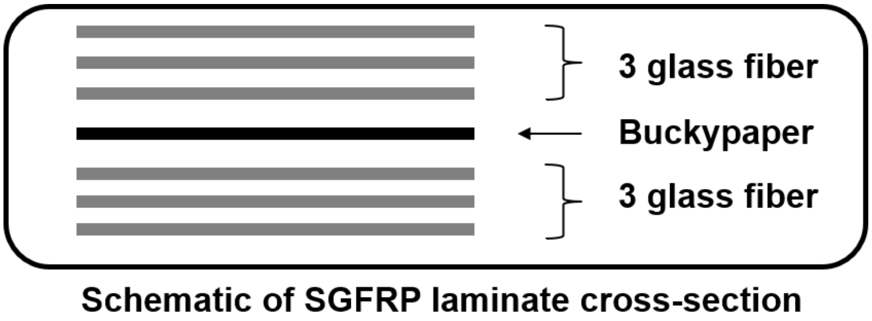

(a)

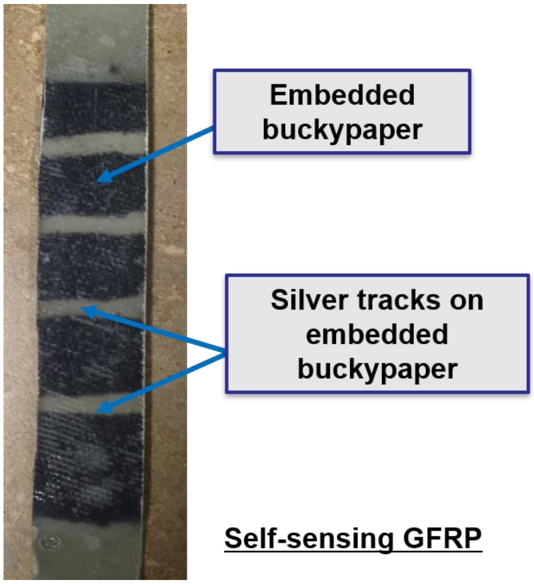

(b)

Figure 5.1: (a) Schematic of SGFRP cross-section; (b) SGFRP specimen for piezoresistive characterization

5.2.2 In-Situ Strain Sensing in SGFRP

Monotonic and Cyclic loading tests were conducted on self-sensing GFRP specimens to capture the piezoresistive response of the embedded buckypaper layer. Monotonic tests were conducted at a constant displacement rate of 0.5 mm/min on an MTS Bionix servo-hydraulic test system. Under monotonic tensile loading, the piezo-resistive response of buckypaper embedded GFRP laminates was recorded using Fluke 289 multimeter with a data logging feature and the strain fields on the specimen surface were analyzed using a Digital Image Correlation (DIC) Aramis 5M system (Aramis 2012). Sensitivity, also known as gauge factor, of the buckypaper sensors was calculated from the relation (Oliva-Aviles A.I. et al. 2011),

$$GF = \left(\frac{R - R_o}{R_o}\right)\left(\frac{1}{\varepsilon}\right) \tag{3}$$

where R is the electrical resistance at strained state, Ro is the original resistance and ε is the longitudinal strain increment. To analyze the piezoresistive response of the SGFRP under tension-tension cyclic loading, 8” x 1” specimens were tested with a strain range of 0.002 to 0.009 and the piezoresistive response was recorded in real time using the digital multimeter (Fluke 289).

5.2.3 In-Situ Fatigue Crack Quantification in SGFRP

The fatigue crack propagation in single edge notch SGFRP specimens (shown in Figure 5.2) was investigated next. The specimens were subjected to displacement-controlled tension-tension fatigue at a frequency of 5 Hz with strain range of 0.002 to 0.0065, and the load ratio was approximately 0.2. A measurement model was developed to correlate the fatigue crack length at any instant to the electrical resistance of the SGFRP specimen along the gauge length and in-situ resistance readings were recorded during the fatigue tests.

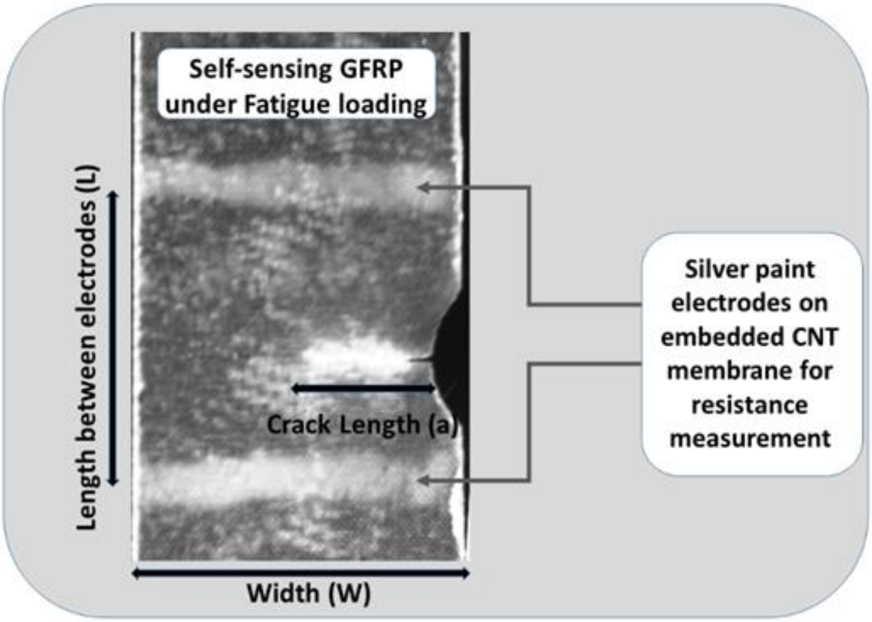

Figure 5.2. Schematic of the measurement model for fatigue damage quantification

Since the loading was uniaxial and pure mode-I, the crack growth was approximately perpendicular to the loading axis. As the crack length increases, a reduction in the effective conducting width of the SGFRP specimen is observed. Based on this, the measurement model is derived from the direct current (DC) resistivity equation, accommodating for the reduction in conducting width of the specimen due to increase in crack length, and is given as,

$$R = \frac{\rho L}{t(w-a)} \tag{5.3}$$

In Equation (5.3), a is the crack length and R is the measured electrical resistance of the specimen, L is the length of embedded buckypaper (measured between the electrodes), w is the initial average width of buckypaper in the region between electrodes, t is the thickness of the embedded buckypaper and ρ is the electrical resistivity of SGFRP specimen. Figure 5.2 shows the SGFRP specimen along with the schematic of the measurement model.

5.3 Results and Discussions

5.3.1 In-Situ Strain Sensing in SGFRP

Strain distribution in the buckypaper embedded region of the GFRP specimens, obtained from DIC, is shown in Figure 5.3a and 5.3b. Strains along the loading axis are shown at an intermediate and failure stages at Figure 5.3a and 5.3b, respectively. Reasonably uniform strain distribution was observed until approximately 1% average strain and the sensor data directly correlates with the average global strain until this point. At average strain values above 1%, the strain distribution starts to become non-uniform and sensor data cannot be considered to represent average strain in the region between electrodes.

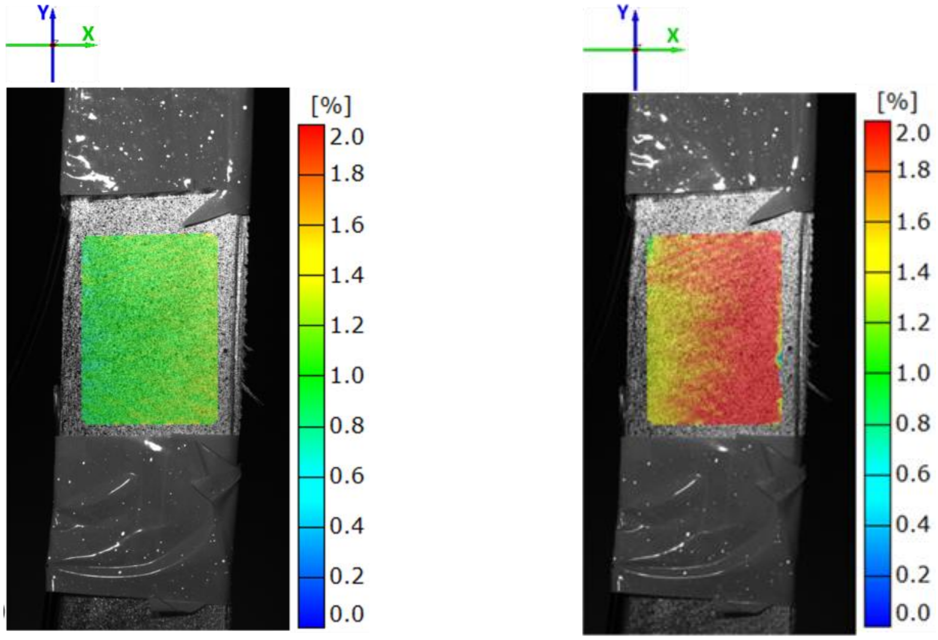

(a) **Average Y-strain = 1.0635%** (b) **Average Y-strain = 1.907%**

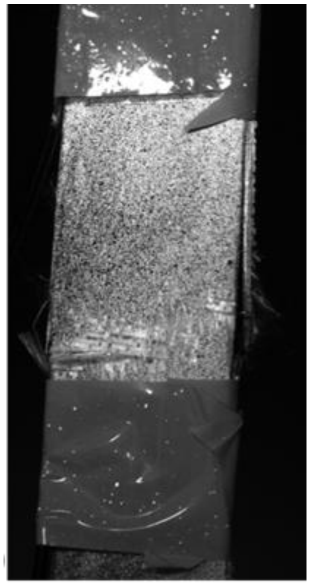

(c) **Failed specimen**

Figure 5.3: (a) Uniform strain distribution in buckypaper embedded region until 1% strain; (b) strain distribution on specimen surface just before failure; (c) failed specimen

Piezo-resistive response of the buckypaper embedded GFRP strips under tensile loading is presented in Figure 5.4. Figure 5.4a shows the normalized resistance change as the strain evolves until failure. Figure 5.4b shows stable sensitivity of the embedded buckypaper till 1.3% strain. The average sensitivity of five self-sensing GFRP specimens as calculated by a linear fit between 0.2% to 0.6% strain was found to be 4.21. This is significantly higher than sensitivity values reported in literature for many CNT based sensors (Rein et al. 2011; Meng et al. 2008; Bautista-Quijano 2010), also it is greater than the sensitivity for conventional strain gauges that are commercially available. Higher sensitivity is clearly desirable, allowing very low strains to be detected with a measurable resistance change.

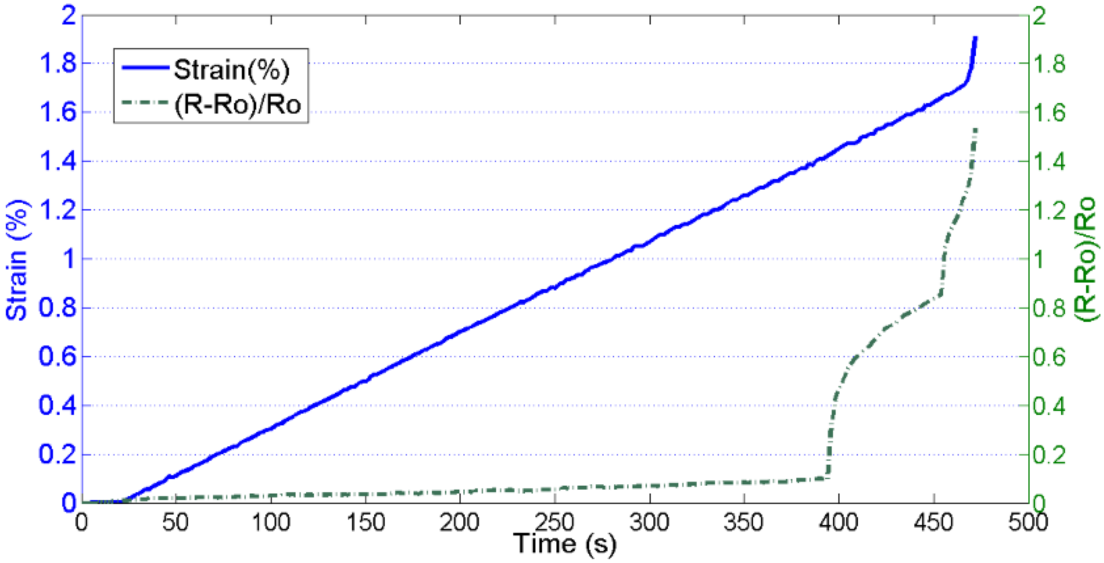

(a)

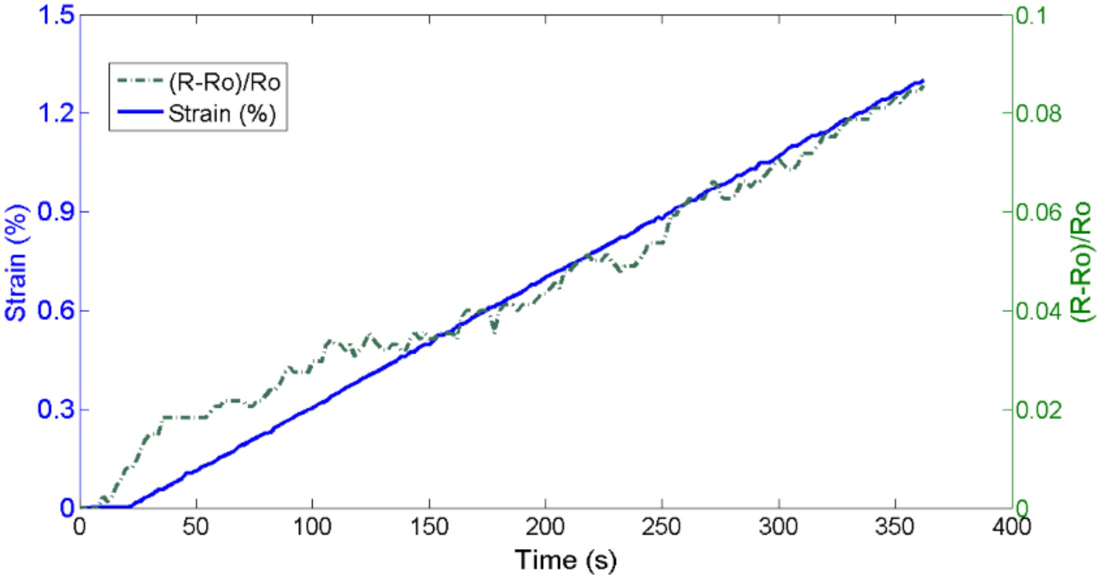

(b)

Figure 5.4: (a) Piezoresistive response of the buckypaper embedded GFRP until failure; and (b) until 1.3% strain showing stable sensitivity

Under cyclic loading, the SGFRP specimens showed stable and repeatable piezoresistive response and the resistance change with cyclic strain for a representative specimen is shown in Figure 5.5. The piezoresistive response shows negligible phase lag with strain, indicating strong adhesion and minimal slippage at the glass fiber/buckypaper interface. The gauge factor was found to be higher for the first loading cycle (9.34 for ascending and 5.08 for descending) as compared to the subsequent loading cycles, retaining a stable sensitivity over the next five cycles with an average value of 5.62 for ascending and 4.17 for descending segments of the cycles. The sensitivity values for each cycle for the representative specimen are presented in Table 5.1. Higher sensitivity in the first cycle can be attributed to additional interactions at the buckypaper/glass-fiber interface. The effect of this extra interaction diminishes after the first cycle, and the sensitivity reduces to a stable value. The sensitivity values are significantly higher than those obtained using commercially available conventional strain gauges as well several CNT based composite sensors reported in literature. The higher sensitivity is a promising feature, allowing very low strains to be detected with a measurable resistance change.

Delamination was observed at the buckypaper/glass-fiber interface of the composite after 80,000 cycles indicating end of functional life of the embedded sensor. The fatigue tests were terminated after 200,000 cycles and complete failure of the specimen was not observed. However, consistent load drop after 100,000 cycles could be an indicative of cyclic softening in the polymer matrix.

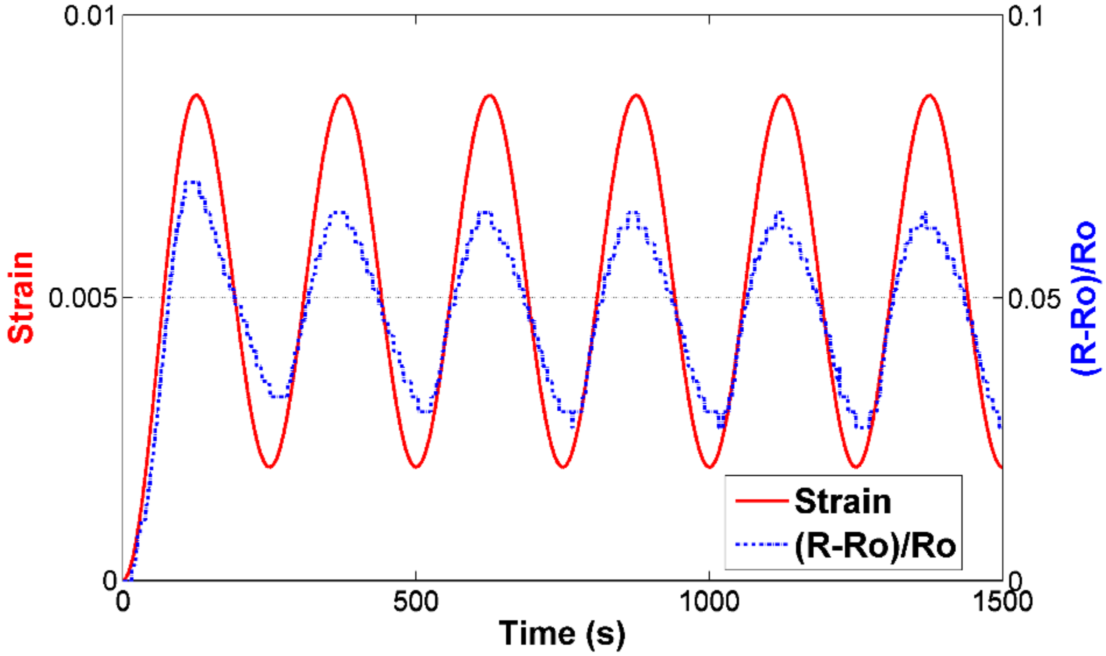

Figure 5.5: Piezoresistive response of SGFRP under cyclic loading

Table 5.1: Gauge factor of SGFRP when subjected to cyclic loading

Cycle	GF-ascending	GF-descending
1	9.34	5.08
2	5.76	4.01
3	5.81	4.34
4	5.50	4.21
5	5.52	4.17
6	5.49	4.10

5.3.2 In-Situ Fatigue Damage Quantification

Single-edge notched specimens of baseline-GFRP and SGFRP tested under fatigue loading are summarized in Table 5.2. The experimentally obtained values of electrical resistance at different crack lengths, normalized with respect to the maximum resistance from the measurement model, are presented in Figure 5.6 as a function of instantaneous crack lengths for three specimens. The resistance trends as a function of crack length were found to be in close agreement with the measurement model presented in Equation 5.3.

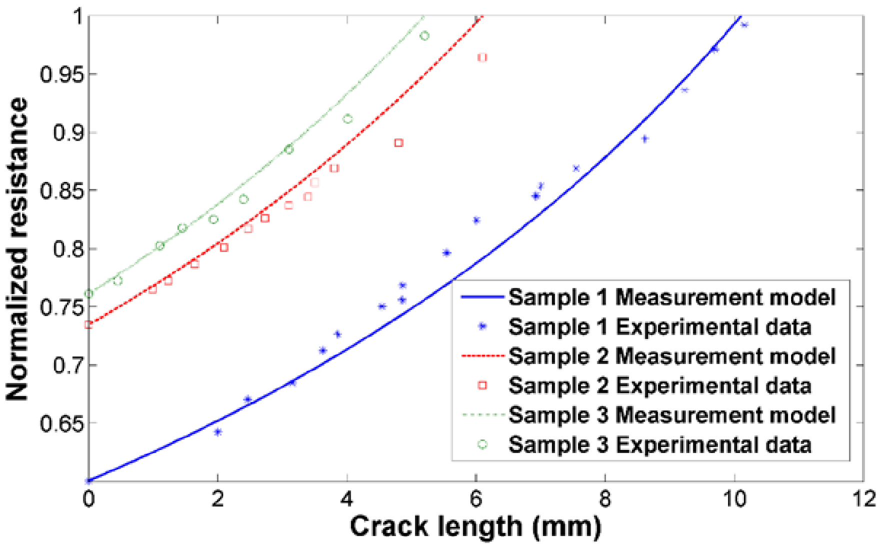

Figure 5.6: Normalized resistance trends with fatigue crack extension

Table 5.2: Single-edge notched baseline-GFRPs and SGFRPs tested under fatigue loading

Specimen ID	Fatigue life (cycles)	Average Crack growth rate (mm/cycle)
SGFRP 1	28620	5.58×10^{-4}
SGFRP 2	16780	4.83×10^{-4}
SGFRP 3	19560	5.97×10^{-4}
SGFRP 4	16200	4.98×10^{-4}
SGFRP 5	18345	5.56×10^{-4}
SGFRP 6	23655	5.28×10^{-4}
Baseline-GFRP 1	13840	1.02×10^{-3}
Baseline-GFRP 2	9050	1.61×10^{-3}
Baseline-GFRP 3	11240	1.42×10^{-3}

Baseline-GFRP 4	8425	1.98×10^{-3}
Baseline-GFRP 5	8890	1.45×10^{-3}
Baseline-GFRP 6	10460	1.67×10^{-3}

The resistance readings were successfully obtained during the fatigue crack growth prior to the occurrence of fast fracture. Figure 5.7 shows good agreement between the crack lengths quantified in SGFRPs using the in-situ electrical resistance measurements and those obtained using the high-resolution camera.

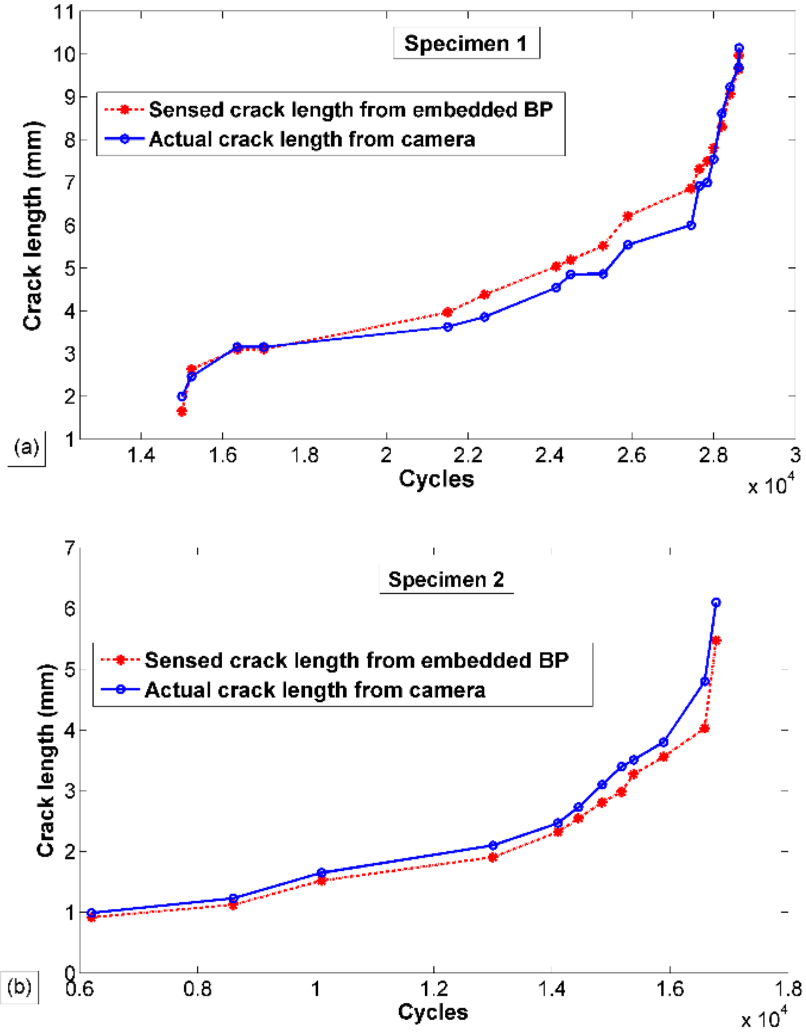

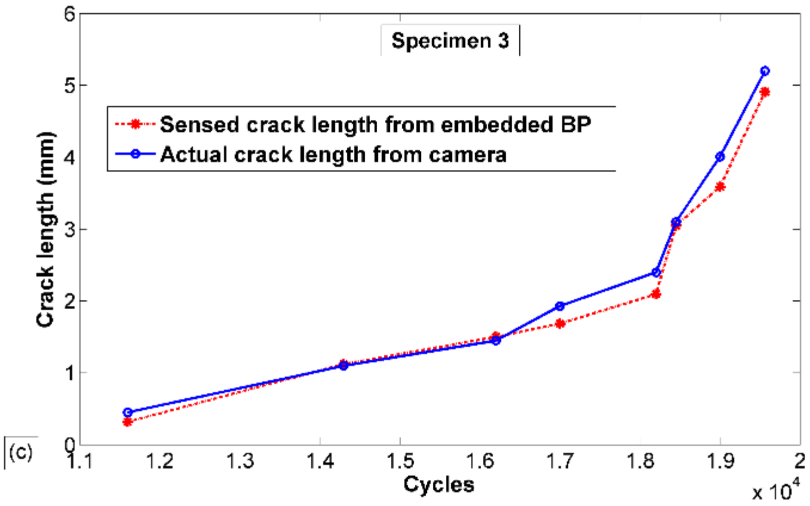

Figure 5.7: Actual crack lengths and sensed crack lengths as a function of fatigue cycles for three specimens

Series of images obtained for the SGRFP specimens at progressive stages of the fatigue test are presented in Figure 5.8a, where the trend in crack propagation is representative of six specimens tested under the same fatigue loading. The average crack growth rate from six specimens was found to be 5.36 x 10-4 mm/cycle over the stable crack propagation regime (between crack initiation and fast fracture regime). In comparison, the average crack growth rate in baseline GFRP specimens after crack initiation was found to be 1.53 x 10-3 mm/cycle, which is significantly higher than SGFRPs.

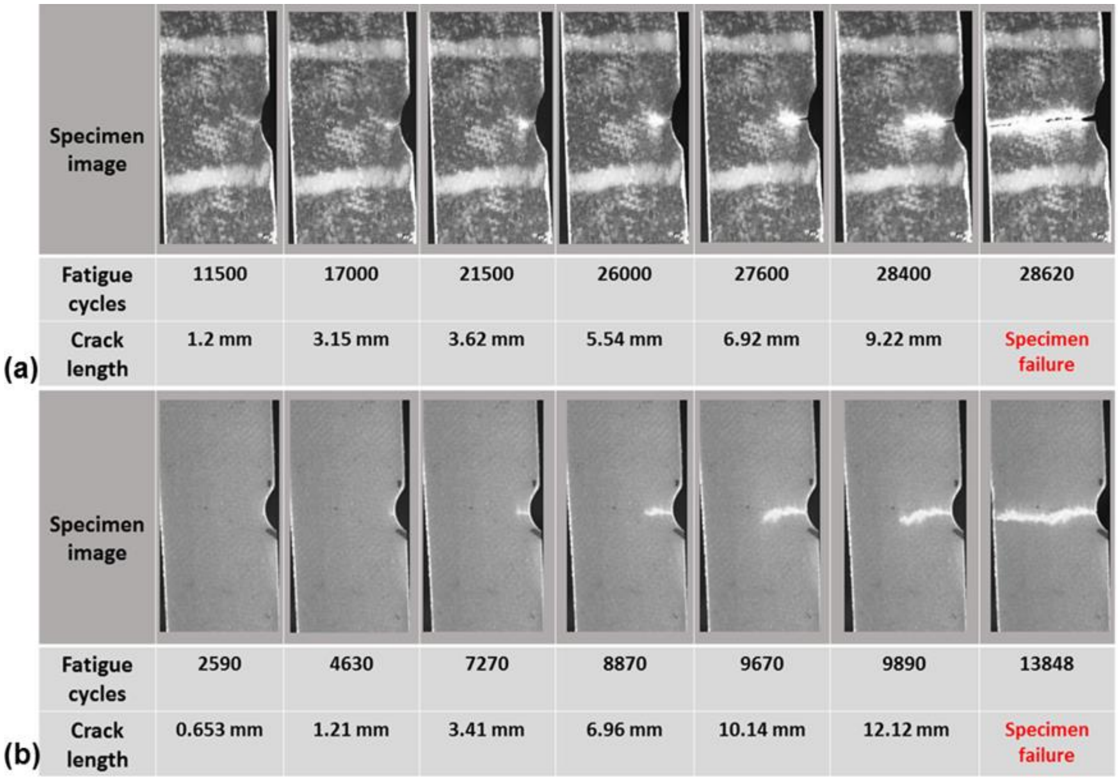

Figure 5.8: Fatigue crack propagation in: (a) SGFRP specimen; (b) baseline GFRP specimen

The significant reduction in the fatigue crack growth rate due to the introduction of buckypaper in the interlaminar region of the GFRP laminates can be explained as follows. The presence of the randomly oriented and densely entangled microstructure of the embedded buckypaper results in a highly torturous crack path leading to retardation in the fatigue crack growth rate and even crack arrest at various instances during crack propagation. As shown in Figure 5.8a, the crack path in SGFRPs was highly torturous and crack tip blunting is observed at various stages of the fatigue test. From Figure 5.8a it can be observed that during crack propagation from 15000 to 21500 fatigue cycles, the crack tip becomes blunt without noticeable increase in crack length. Figure 5.8b shows fatigue crack propagation trend in one of the baseline-GFRP specimens where a relatively sharp and defined crack tip can be observed and the trend is representative of six GFRP specimens tested under the same fatigue loading. Figure 5.9 shows the crack growth rate vs crack length for GFRP and SGFRP specimens for comparison. The baseline-GFRPs consistently showed shorter fatigue life as compared to the SGFRPs and this observation points to an additional crack deceleration type attribute of the SGFRP.

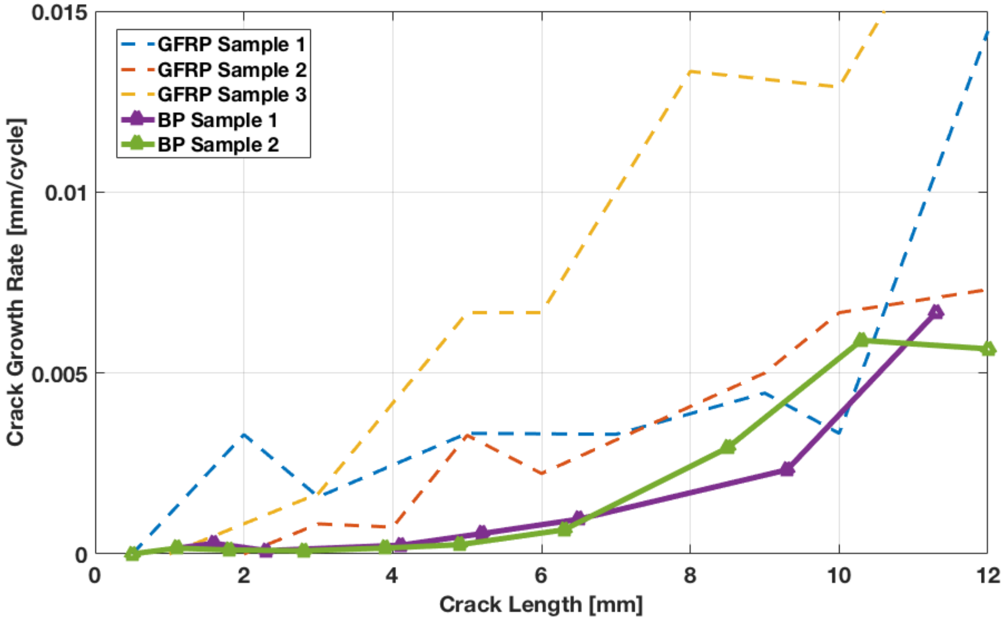

Figure 5.9: Crack growth rate vs crack length for GFRP and SGFRP specimens

Hence, buckypapers fabricated using the novel slurry compression method, when embedded in GFRPs, successfully induced self-sensing capabilities and improved the fatigue resistance in GFRP laminates.

5.4 Summary

Carbon nanotube buckypapers manufactured by a novel slurry compression process were used to develop self-sensing glass fiber reinforced polymer matrix laminates with improved resistance to fatigue crack growth. The buckypapers were embedded in the interlaminar region of the laminates through a wet-layup procedure and silver ink electrodes were applied onto the buckypapers prior to embedment. The silver ink forms a thin layer on the buckypaper surface and minimizes the contact resistance, enabling stable piezoresistive readings during mechanical loading. This configuration also helps in avoiding the use of any invasive electrodes or sensors that could create damage hot-spots with the composite laminate.

The SGFRP specimens tested under monotonic and cyclic loading showed high sensitivity to strain over a significant strain range. The resistance change with strain was found to be in-sync and the gauge factor was consistent over multiple loading cycles. Furthermore, fatigue crack growth experiments were performed on single-edge notched specimens of SGFRP and a measurement model was developed to quantify the instantaneous crack length with change in electrical resistance; close correlation was observed with experimentally obtained fatigue crack data. A comparison of fatigue crack propagation trends conducted on the test specimens at various stages of fatigue showed significantly lower crack growth rates for the SGFRP specimens. The improved fatigue crack growth resistance was attributed to the crack-tip blunting and crack arrest caused by the nano and micron sized, randomly oriented and entangled CNT bundles that act as obstructions to the propagating crack-tip. These results point to the multifunctional nature of the buckypaper embedded composites.

6 CONTRIBUTIONS AND FUTURE WORK

6.1 Contributions

The primary objective of the research presented in this dissertation was to gain comprehensive insight into the complex multiaxial fatigue crack growth behavior of heterogeneous aerospace materials such as Al 7075 T651 alloy and glass fiber reinforced polymer (GFRP) composite. Furthermore, a novel multifunctional CNT-based FRP nanocomposite was developed for accurate *in-situ* fatigue damage quantification and improved resistance to fatigue crack growth.

The variable amplitude complex multiaxial fatigue behavior of Al 7075 alloy was studied by exclusively capturing the effects of individual overloads and underloads of different magnitudes and mode-mixities on micro- and macroscale crack growth behavior. In addition, the interaction effects between overloads and underloads were also explored. Some of the key findings from the biaxial fatigue tests with pure mode-I overloads include: (i) the trends for crack growth retardation and recovery and their dependence on overload magnitude and instantaneous fatigue crack length at the time of overload; (ii) the role of different fatigue-fracture micromechanisms, such as plasticity induced crack closure, crack deflection, crack branching and roughness induced crack closure, on the crack retardation characteristics post-overload; and (iii) a numerical model to predict crack retardation behavior and fatigue life under the influence of overloads of different magnitudes. The acceleration effects of single underloads and the interaction of an overload with underload were also captured through carefully monitoring crack growth trends and conducting quantitative fractography on the fracture surfaces. From the biaxial fatigue tests with mixed-mode overloads, and the corresponding fracture surface analyses, interesting crack growth phenomenon were revealed. The crack retardation characteristics and fatigue-fracture mechanisms for short cracks and long cracks subjected to mixed-mode overloads were identified and correlated with their micro- and macroscale crack growth behavior. Hence, detailed insight into the fatigue crack growth behavior in aerospace grade Al 7075 alloy under complex VA biaxial loading conditions was established and the corresponding governing micromechanisms were experimentally confirmed through quantitative fractography.

For the GFRP composite, self-sensing capabilities such as strain sensing and fatigue damage quantification were successfully introduced by the embedment of CNT buckypapers. A novel fabrication process was developed for rapid manufacturing of sizable buckypaper membranes that were suitable for embedment in a polymer matrix. The piezoresistive property of the embedded buckypapers was effectively used to monitor strain in the host GFRP laminates in real-time under static and cyclic loads. A measurement model is also presented, which correlates the fatigue crack length at any instance to the electrical resistance measurement from the embedded buckypaper, allowing for *in-situ* crack length quantification. Furthermore, the resistance to fatigue crack growth in GFRPs was improved by embedding the buckypaper membrane and an order of magnitude reduction in the crack growth rate was obtained. The ease of fabrication of sizable multifunctional buckypaper membranes through the newly developed fabrication process allows for efficiently extending the applications of CNT based composites to the structural scale. This research represents substantial progress toward the understanding and prediction of fatigue damage progression in aerospace materials, and the development of more efficient multifunctional materials for aerospace applications.

6.2 Future Work

While the research presented in this dissertation serves to significantly improve the understanding of biaxial fatigue crack growth in aerospace-grade Al 7075 alloy under complex VA loads, and provides a novel methodology for producing a self-sensing composite material with improved fatigue resistance, further developments and advancements are necessary to maximize its applicability and effectiveness. Future work topics are essential to understand, predict and delay fatigue damage progression in aerospace materials:

- The biaxial fatigue study presented in Chapter 2 on micro- and macroscale fatigue-fracture behavior of Al 7075 subjected to single overloads and underloads of different magnitudes can be extended to: exploring the effects of biaxial overload and underload block loadings, in addition to flight spectrum loadings such as the Transport Wing Standard (TWIST) and Fighter Aircraft Loading Standard for Fatigue Evaluation (FALSTAFF). Quantitative fractography can be performed to thoroughly understand the governing micromechanisms and crack growth characteristics. Numerical models can be developed to predict crack retardation and acceleration behavior for overloads, underloads and variable amplitude flight spectra to accurately predict fatigue life. This will provide valuable insight into the biaxial fatigue behavior of aerospace alloys and enable more effective and accurate fatigue life prediction methodologies.

- The research work presented in Chapter 3 on biaxial fatigue of Al 7075 under the influence of mixed-mode (mode I+II) overloads was conducted with overloads of BR=0.5 and 0.75 and the mode-II component of the overloads was significantly lesser than that of mode-I. Hence to better understand the effects of higher mode-II stresses in an overload, or pure mode-II overloads, fatigue tests need to be conducted with overloads of BR=0.25, -0.5 and -1. These overloads will lead to increased mode-mixity and shed light on the fatigue-fracture characteristics and micromechanisms that govern crack growth under mode-II dominant fatigue cycles.
- For the novel buckypaper fabrication process discussed in Chapter 3, several parametric studies can be done using constituent CNTs of different lengths, diameters and functional groups. The geometric properties and functionalization-type of the CNTs can significantly affect the microstructure and bulk properties of the fabricated buckypaper. Functionalized CNTs have shown improved interfacial interaction with the host polymer matrix and improved mechanical properties. This could significantly improve multifunctional properties of the buckypaper and make it more suitable for embedment in composite laminates.
- The self-sensing GFRP developed as part of this research work showed promising results for *in-situ* strain sensing and fatigue damage quantification, in addition to improved fatigue resistance. The use of functionalized CNT buckypaper can further improve the fatigue resistance of the GFRPs and lead to increase in other properties such as thermal and electrical conductivity, piezoresistive sensitivity, and tensile

strength and modulus. Other multifunctional capabilities such as EMI shielding, fire retardance and radar wave absorption also need to be explored. By embedding several buckypaper layers at multiple interlaminar locations, further investigations into the fatigue behavior can be conducted to potentially further improve resistance to fatigue damage progression.

REFERENCES

Alexopoulos, N., Bartholome, C., Poulin, P., & Marioli-Riga, Z. (2010). Structural health monitoring of glass fiber reinforced composites using embedded carbon nanotube (CNT) fibers. Composites Science and Technology, 70(2), 260-271

Allaoui, A., Bai, S., Cheng, H., & Bai, J. (2002). Mechanical and electrical properties of a MWNT/epoxy composite. Composites Science and Technology, 62(15), 1993-1998

Aramis (2012), User's Manual for 3-D Image Photogrammetry, GOM mbH, mittelweg, Braunschweig, Germany.

Ashrafi B., Guan J., Mirjalili V., Hubert P., Simard B., and Johnston A. (2010). “Correlation between Young’s modulus and impregnation quality of epoxy-impregnated SWCNT buckypaper.” Comp. Part A, 41, 1184-1191.

Balageas, D., Fritzen, C., & Güemes, A. (2010). *Structural health monitoring* John Wiley & Sons.

Bautista-Quijano J.R., Avilés F., Aguilar J.O., and Tapia A. (2010). “Strain sensing capabilities of a piezoresistive MWCNT-polysulfone film.” *Sensors and Actuators A*, 159, 135-140.

Benlikaya R., Slobodian P., and Riha P. (2013). “Enhanced strain-dependent electrical resistance of polyurethane composites with embedded oxidized multiwalled carbon nanotube networks.” Journal of Nanomat., article ID 327597.

Böger, L., Wichmann, M. H., Meyer, L. O., & Schulte, K. (2008). Load and health monitoring in glass fibre reinforced composites with an electrically conductive nanocomposite epoxy matrix. *Composites Science and Technology*, *68*(7), 1886-1894.

Borrego, L. P., F. V. Antunes, J. M. Costa, and J. M. Ferreira. "Mixed-mode fatigue crack growth behaviour in aluminium alloy." *International Journal of Fatigue* 28, no. 5-6 (2006): 618-626.

Carpinteri A, Spagnoli A, Vantadori S. A multiaxial fatigue criterion for random loading. *Fatigue & Fracture of Engineering Materials & Structures*. 2003;26(6):515-522.

Chen X., Wang J., Lin M., Zhong W., Feng T., Chen X., Chen J., and Xue F. (2008). "Mechanical and thermal properties of epoxy nanocomposites reinforced with amino-functionalized multi-walled carbon nanotubes." Mater. Sci. and Engg. A, 492, 236–242.

Cheng Q., Bao J., Park J., Liang Z., Zhang C., and Wang B. (2009). "High mechanical performance composite conductor: multi-walled carbon nanotube sheet/bismaleimide nanocomposites." Adv. Funct. Mater. 19 3219-3225.

Cherng-Shii Y. (2004). "Characterization of nanotube buckypaper manufacturing process". Electronic Theses, Treatises and Dissertations. Paper 420.

Chih-Yen L. (2005). "Investigation and characterization of SWNT buckypaper manufacturing process" *Electronic Theses, Treatises and Dissertations,* Paper 1341.

Chu H., Zhang Z., Liu Y., and Leng J. (2014). "Self-heating fiber reinforced polymer composite using meso/macropore carbon nanotube paper and its application in deicing." Carbon, 66**,** 154-163.

Chu, H., Zhang, Z., Liu, Y., & Leng, J. (2014). Self-heating fiber reinforced polymer composite using meso/macropore carbon nanotube paper and its application in deicing. *Carbon, 66,* 154-163.

Coleman, J. N., Khan, U., Blau, W. J., & Gun'ko, Y. K. (2006). Small but strong: A review of the mechanical properties of carbon nanotube–polymer composites. *Carbon, 44*(9), 1624-1652.

Colin J, Fatemi A. Variable amplitude cyclic deformation and fatigue behaviour of stainless steel 304L including step, periodic, and random loadings. *Fatigue & Fracture of Engineering Materials & Structures*. 2010;33(4):205-220.

Cooper S.M., Chuang H.F., Cinke M., Cruden B.A., and Meyyappan M. (2003). "Gas permeability of a Buckypaper membrane." *Nano Lett.,* **3** (2), 189-192.

Corbly D, Packman P. On the influence of single and multiple peak overloads on fatigue crack propagation in 7075-T6511 aluminum. *Eng Fract Mech*. 1973;5(2):479-497.

Dahlin, Peter, and Mårten Olsson. "Fatigue crack growth–Mode I cycles with periodic Mode II loading." *International Journal of Fatigue* 30, no. 5 (2008): 931-941.

Dahlin, Peter, and Mårten Olsson. "Mode I fatigue crack growth reduction mechanisms after a single Mode II load cycle." *Engineering fracture mechanics* 73, no. 13 (2006): 1833-1848.

Dahlin, Peter, and Mårten Olsson. "Reduction of mode I fatigue crack growth rate due to occasional mode II loading." *International Journal of Fatigue* 26, no. 10 (2004): 1083-1093.

Datta, S., Fard, M. Y., & Chattopadhyay, A. (2015). High-speed surfactant-free fabrication of large carbon nanotube membranes for multifunctional composites. *Journal of Aerospace Engineering*, *29*(3), 04015060.

Datta, S., Fard, M. Y., & Chattopadhyay, A. (2016). Fatigue crack growth behavior of hybrid glass fiber laminates with embedded functionalized carbon nanotube membranes. *ASME 2016 International Mechanical Engineering Congress and Exposition,* V009T12A067-V009T12A067.

Datta, S., Fard, M. Y., Johnston, J.P., Quigley E. & Chattopadhyay, A. (2015). In-situ strain and damage sensing in glass fiber laminates using embedded CNT. *Structural Health Monitoring 2015.*

Datta S, Chattopadhyay A, Iyyer N and Phan N. (2018). Fatigue Crack Propagation Under Biaxial Fatigue Loading with Single Overloads. *International Journal of Fatigue*, 109, 103-113

Datta S, Neerukatti RK and Chattopadhyay A (2018) Buckypaper Embedded Self-Sensing Composite for Real-Time Fatigue Damage Diagnosis and Prognosis. *Carbon*, 139, 353-360

Datta, S & Chattopadhyay, A. (2018) Micromechanisms Governing Crack Propagation in Al 7075 Under in-Plane Biaxial Fatigue with Single Overloads. 2018 AIAA/ASCE/AHS/ASC Structures, Structural Dynamics, and Materials Conference, AIAA SciTech Forum, (AIAA 2018-2004)

Datta, S. & Chattopadhyay, A. (2016) Carbon Nanotube Membrane Systems and Methods of Synthesis. US Patent App. 15/154,754

Dharap P., Li Z., Nagarajaiah S., and Barrera E.V. (2004). "Nanotube film based on single-wall carbon nanotubes for strain sensing." Nanotechnology, 15, 379-382.

Dieze-Pascual A.M., Guan J., Simard B., and Gomez-Fatou M.A. (2012). "Poly(phenylene sulphide) and poly(ether ether ketone) composites reinforced with single-walled carbon nanotube buckypaper: II – Mechanical properties, electrical and thermal conductivity." Composites Part A, 43, 1007-1015

Dumée L.F., Sears K., Schütz J., Finn N., Huynh C., Hawkins S., Duke M., Gray S. (2010). "Characterization and evaluation of carbon nanotube bucky-Paper membranes for direct contact membrane distillation." J. of Memb. Sci., 351, 36-43.

Elber W. The significance of fatigue crack closure. In: *Damage tolerance in aircraft structures.* ASTM International; 1971.

Erdogan F, Sih G. On the crack extension in plates under planeloading and transverse shear. J Basic Eng. 1963;85:519-527

Fard, M. Y., Woodward, J. M., Datta, S., Raji, B., & Chattopadhyay, A. (2016). Characterization of interlaminar fracture properties of advanced polymer matrix composites interleaved with buckypaper. Paper presented at the ASME 2016 International Mechanical Engineering Congress and Exposition, V009T12A083-V009T12A083.

Ferrreira, A., Rocha, J., Ansón-Casaos, A., Martínez, M., Vaz, F., & Lanceros-Mendez, S. (2012). Electromechanical performance of poly (vinylidene fluoride)/carbon nanotube composites for strain sensor applications. *Sensors and Actuators A: Physical, 178*, 10-16.

Fu X., Zhang C., Liu T., Liang R., and Wang B. (2010). "Carbon nanotube buckypaper to improve fire retardancy of high-temperature/high-performance polymer composites." Nanotechnology, 21 (23), 235701 (8pp).

Fu, X., Zhang, C., Liu, T., Liang, R., & Wang, B. (2010). Carbon nanotube buckypaper to improve fire retardancy of high-temperature/high-performance polymer composites. *Nanotechnology, 21*(23), 235701.

Giurgiutiu, V., Zagrai, A., & Jing Bao, J. (2002). Piezoelectric wafer embedded active sensors for aging aircraft structural health monitoring. *Structural Health Monitoring, 1*(1), 41-61.

Gojny, F. H., Wichmann, M. H., Fiedler, B., & Schulte, K. (2005). Influence of different carbon nanotubes on the mechanical properties of epoxy matrix composites–a comparative study. *Composites Science and Technology, 65*(15), 2300-2313.

Gojny, F. H., Wichmann, M. H., Fiedler, B., Bauhofer, W., & Schulte, K. (2005). Influence of nano-modification on the mechanical and electrical properties of conventional fibre-reinforced composites. *Composites Part A: Applied Science and Manufacturing, 36*(11), 1525-1535.

Gojny, F., Wichmann, M., Köpke, U., Fiedler, B., & Schulte, K. (2004). Carbon nanotube-reinforced epoxy-composites: Enhanced stiffness and fracture toughness at low nanotube content. *Composites Science and Technology, 64*(15), 2363-2371.

Harmain G. A model for predicting the retardation effect following a single overload. *Theor Appl Fract Mech*. 2010;53(1):80-88.

Huang X, Torgeir M, Cui W. An engineering model of fatigue crack growth under variable amplitude loading. *Int J Fatigue*. 2008;30(1):2-10.

Iijima, S. (1991). "Helical microtubules of graphitic carbon." *Nature,* 354, 56-58.

Irwin GR. Analysis of stresses and strains near the end of a crack traversing a plate. *Journal of applied mechanics*. 1957;24(3):361-364.

Islam M.F., Rojas E., Bergey D.M., Johnson A.T., and Yodh A.G. (2003). “High weight fraction surfactant solubilization of single-wall carbon nanotubes in water.” Nano Letters 3 (2), 269-273.

Jiang Y. A fatigue criterion for general multiaxial loading. *Fatigue and fracture of engineering materials and structures*. 2000;23(1):19-32.

Kang I., Schulz M.J., Kim J.H., Shanov V., and Shi D. (2006). “A carbon nanotube strain sensor for structural health monitoring.” Smart Mater. Struct., 15, 737-748.

Kang, I., Schulz, M. J., Kim, J. H., Shanov, V., & Shi, D. (2006). A carbon nanotube strain sensor for structural health monitoring. *Smart Materials and Structures, 15*(3), 737.

Kim, K. J., Yu, W., Lee, J. S., Gao, L., Thostenson, E. T., Chou, T., & Byun, J. (2010). Damage characterization of 3D braided composites using carbon nanotube-based in situ sensing. *Composites Part A: Applied Science and Manufacturing, 41*(10), 1531-1537.

Lankford J, Davidson DL. The effect of overloads upon fatigue crack tip opening displacement and crack tip opening closing loads in aluminium alloys. 1981.

Lee E, Glinka G, Vasudevan A, Iyyer N, Phan N. Fatigue of 7075-T651 aluminum alloy under constant and variable amplitude loadings. *Int J Fatigue*. 2009;31(11):1858-1864.
Li, X., Levy, C., & Elaadil, L. (2008). Multiwalled carbon nanotube film for strain sensing. *Nanotechnology, 19*(4), 045501.

Liu A, Allison J, Dittmer D, Yamane J. Effect of biaxial stresses on crack growth. . 1979.
Liu Q., Li M., Wang Z., Gu Y., Li Y., and Zhang Z. (2013). “Improvement on the tensile performance of buckypaper using a novel dispersant and functionalized carbon nanotubes.” Composites: Part A, 55, 102-109.

Lopes P.E., Hattum F.V., Pereira C.M.C., Nóvoa P.J.R.O., Forero S., Hepp F., and Pambaguian L. (2010). “High CNT content composites with CNT Buckypaper and epoxy resin matrix: Impregnation behaviour composite production and characterization.” *Composite Structures*, **92,** 1291-1298.

Mall S, Perel V. Crack growth behavior under biaxial fatigue with phase difference. *Int J Fatigue*. 2015;74:166-172.

Meincke, O., Kaempfer, D., Weickmann, H., Friedrich, C., Vathauer, M., & Warth, H. (2004). Mechanical properties and electrical conductivity of carbon-nanotube filled polyamide-6 and its blends with acrylonitrile/butadiene/styrene. *Polymer, 45*(3), 739-748.

Meng C., Liu C., and Fan S. (2008). "Flexible carbon nanotube/polyaniline paper-like films and their enhanced electrochemical properties." *Electrochem. Comm.*, 11, 186-189.

Mikheevskiy S, Glinka G. Elastic–plastic fatigue crack growth analysis under variable amplitude loading spectra. *Int J Fatigue*. 2009;31(11):1828-1836.
Moerman K., Holt C., Evans S., and Simms C. (2009). "Digital image correlation and finite element modelling as a method to determine mechanical properties of human soft tissue in vivo." *J. of Biomech.*, 42, 1150-1153.

Nayeb-Hashemi, H., and M. E. Taslim. "Effects of the transient Mode II on the steady state crack growth in Mode I." *Engineering Fracture Mechanics* 26, no. 6 (1987): 789-807.

Neerukatti R, Datta S, Chattopadhyay A, Iyyer N, Phan N. (2017). Fatigue crack propagation under in-phase and out-of-phase biaxial loading. *Fatigue & Fracture of Engineering Materials & Structures*. 41 (2), 387-399.

Neerukatti R, Datta S, Chattopadhyay A, Iyyer N, Phan N. Characterization of Fatigue Crack Propagation Under Complex Biaxial Loading. ASME. ASME International Mechanical Engineering Congress and Exposition, Volume 9: Mechanics of Solids, Structures and Fluids; NDE, Diagnosis, and Prognosis: V009T12A041.

Nelson D. Review of fatigue crack-growth prediction under irregular loading. chicago, IL: Spring meet. *Society for Experimental Stress Analysis*. 1975:11-16.

Newman J. A crack-closure model for predicting fatigue crack growth under aircraft spectrum loading. In: *Methods and models for predicting fatigue crack growth under random loading.* ASTM International; 1981.

Oliva-Aviles A.I., Aviles F., and Sosa V. (2011). “Electrical and piezoresistive properties of multi-walled carbon nanotube/polymer composite films aligned by an electric field.” *Carbon*, 49, 2989-2997.

Ounnunkad S., Minett A.I., Misides M.D., Duffy N.W., Fleming B.D., Lee C.Y., Bond A.M., and Wallace G.G. (2011). “Comparison of the electrochemical behaviour of buckypaper and polymer-intercalated buckypaper electrodes.” J. of Electroanalytical Chem., 652, 52-59.

Park J.G., Louis J., Cheng Q., Bao J., Smithyman J., Liang R., Wang B., Zhang C., Brooks J.S., Kramer L., Fanchasis P., and Dorough D. (2009). “Electromagnetic interference shielding properties of carbon nanotube buckypaper composites.” Nanotechnology, 20, 415702 (7pp).

Pham G.T., Park Y.B., Wang S., Liang Z., Wang B., Zhang C., Funchess P., and Kramer L. (2008). “Mechanical and electrical properties of polycarbonate nanotube buckypaper composite sheets.” *Nanotechnology* 19 325705-708.

Pommier S. (2003) Cyclic plasticity and variable amplitude fatigue. *International Journal of Fatigue*; 25 (9): 983-997.

Qian, J., and A. Fatemi. "Mixed mode fatigue crack growth: a literature survey." *Engineering fracture mechanics* 55, no. 6 (1996): 969-990.

Quigley E., Datta S., & Chattopadhyay A. (2016). A Novel Methodology for Self-Healing at the Nanoscale in CNT/epoxy Composites: International Society for Optics and Photonics. Proceedings Volume 9806, Smart Materials and Nondestructive Evaluation for Energy Systems 2016; 98060M

Rai, A., Subramanian, N., & Chattopadhyay, A. (2016). Investigation of piezo-resistivity in CNT nano-composites under damage. *SPIE Smart Structures and Materials Nondestructive Evaluation and Health Monitoring, Anonymous International Society for Optics and Photonics.* 980017-980017.

Rai, A., Subramanian, N., Koo, B., & Chattopadhyay, A. (2017). Multiscale damage analysis of carbon nanotube nanocomposite using a continuum damage mechanics approach. *Journal of Composite Materials*, *51*(6), 847-858.

Rai A, Datta S, Chattopadhyay A and Lopez C. (2017). Reinforcement of Composite Joint Interface using Nanomaterials. American Society of Mechanical Engineers. ASME International Mechanical Engineering Congress and Exposition, Volume 9: Mechanics of Solids, Structures and Fluids; NDE, Structural Health Monitoring and Prognosis: V009T12A002

Ranganathan N, Aldroe H, Lacroix F, Chalon F, Leroy R, Tougui A. Fatigue crack initiation at a notch. *International Journal of Fatigue*. 2011;33(3):492-499.

Rein M.D., Breuer O., and Wagner H.D. (2011). “Sensors and sensitivity: carbon nanotube buckypaper films as strain sensing devices.” Comp. Sci. and Tech., 71, 373–381

Richard, H. A., B. Schramm, and N-H. Schirmeisen. "Cracks on mixed mode loading–theories, experiments, simulations." *International Journal of Fatigue* 62 (2014): 93-103.

Rushton PA, Taheri F. Prediction of crack growth in 350WT steel subjected to constant amplitude with over-and under-loads using a modified wheeler approach. *Mar Struct*. 2003;16(7):517-539.

Sander, M., and H. A. Richard. "Experimental and numerical investigations on the influence of the loading direction on the fatigue crack growth." *International Journal of Fatigue* 28, no. 5-6 (2006): 583-591.

Sander, M., and H. A. Richard. "Finite element analysis of fatigue crack growth with interspersed mode I and mixed mode overloads." *International Journal of Fatigue* 27, no. 8 (2005): 905-913.

Schijve J, Broek D. Crack propagation: The results of a test programme based on a gust spectrum with variable amplitude loading. *Aircraft Eng Aerospace Technol*. 1962;34(11):314-316.

Schijve J, Skorupa M, Skorupa A, Machniewicz T, Gruszczynski P. Fatigue crack growth in the aluminium alloy D16 under constant and variable amplitude loading. *Int J Fatigue*. 2004;26(1):1-15.

Schijve J, Skorupa M, Skorupa A, Machniewicz T, Gruszczynski P. Fatigue crack growth in the aluminium alloy D16 under constant and variable amplitude loading. *Int J Fatigue*. 2004;26(1):1-15.

Schijve J. The significance of fractography for investigations of fatigue crack growth under variable-amplitude loading. *Fatigue and Fracture of Engineering Materials and Structures*. 1999;22(2):87-100.

Schweizer C, Seifert T, Nieweg B, Von Hartrott P, Riedel H. Mechanisms and modelling of fatigue crack growth under combined low and high cycle fatigue loading. *Int J Fatigue*. 2011;33(2):194-202.

Sears K., Dumée L., Schütz J., She M., Huynh C., Hawkins S., Duke M., and Gray S. (2010). “Recent developments in carbon vanotube membranes for water purification and gas separation.” *Materials,* 3, 127-149.

Seifi R, Bahrami R. Numerical modeling the effects of overloading and underloading in fatigue crack growth. *Eng Failure Anal*. 2010;17(6):1475-1482.
Seifi, Rahman, and Mohammad Eshraghi. "Effects of mixed-mode overloading on the mixed-mode I+ II fatigue crack growth." *Archive of Applied Mechanics* 83, no. 7 (2013): 987-1000.

Shamsaei, Nima, and Ali Fatemi. "Small fatigue crack growth under multiaxial stresses." *International Journal of Fatigue* 58 (2014): 126-135.

Shanyavskiy A. Fatigue cracking simulation based on crack closure effects in al-based sheet materials subjected to biaxial cyclic loads. *Eng Fract Mech*. 2011;78(8):1516-1528.

Shlyannikov, V. N., A. V. Tumanov, and A. P. Zakharov. "The mixed mode crack growth rate in cruciform specimens subject to biaxial loading." *Theoretical and Applied Fracture Mechanics* 73 (2014): 68-81.

Silva, A. L. L., A. M. P. De Jesus, J. Xavier, J. A. F. O. Correia, and A. A. Fernandes. "Combined analytical-numerical methodologies for the evaluation of mixed-mode (I+ II) fatigue crack growth rates in structural steels." *Engineering Fracture Mechanics* 185 (2017): 124-138.

Skorupa M, Skorupa A, Schijve J, Machniewicz T, Korbut P. Fatigue crack growth behaviour of 18G2A steel under constant amplitude loading and following a single overload. *Archive of Mechanical Engineering*. 2000;47(2):139-163.

Skorupa M. Load interaction effects during fatigue crack growth under variable amplitude loading—a literature review. part II: Qualitative interpretation. *Fatigue & Fracture of Engineering Materials & Structures*. 1999;22(10):905-926.

Slobodian P., Riha P., Lengalova A., Svoboda P., and Saha P. (2011). “Multi-wall carbon nanotube networks as potential resistive gas sensors for organic vapor detection.” Carbon, 49, 2499-2507.

Socie D. Multiaxial fatigue damage models. *Transactions of the ASME.Journal of Engineering Materials and Technology*. 1987;109(4):293-298.
Sonsino C. Fatigue testing under variable amplitude loading. *Int J Fatigue*. 2007;29(6):1080-1089.

Spitalsky, Z., Tasis, D., Papagelis, K., & Galiotis, C. (2010). Carbon nanotube–polymer composites: Chemistry, processing, mechanical and electrical properties. *Progress in Polymer Science, 35*(3), 357-401.

Subramanian, N., Rai, A., Datta, S., Koo, B., & Chattopadhyay, A. (2015). A multiscale model coupling molecular dynamics simulations and micromechanics to study the behavior of CNT-enhanced nanocomposites. Paper presented at the *56th AIAA/ASCE/AHS/ASC Structures, Structural Dynamics, and Materials Conference,* 0390

Sunder R, Ilchenko B. Fatigue crack growth under flight spectrum loading with superposed biaxial loading due to fuselage cabin pressure. *Int J Fatigue*. 2011;33(8):1101-1110.

Suresh S. Micromechanisms of fatigue crack growth retardation following overloads. *Eng Fract Mech*. 1983;18(3):577-593.

Tasis D., Tagmatarchis N., Georgakilas V., and Prato M. (2003). “Soluble carbon nanotubes.” Chem. Eur. J., 9, 4000-4008.

Thostenson, E.T., Ren, Z., and Tsu-Wei Chou (2001). “Advances in the science and technology of carbon nanotubes and their composites: a review.” *Comp. Sci. and Tech.,* 61, 1899-1912.

Trebules V, Roberts R, Hertzberg R. Effect of multiple overloads on fatigue crack propagation in 2024-T3 aluminum alloy. In: *Progress in flaw growth and fracture toughness testing.* ASTM International; 1973.

Veliky, Kenneth B., “Cast forming of carbon nanotube networks using paraffin” (2014). Honors Theses. Paper 361.

Vohrer U., Kolaric I., Haque M.H., Roth S., and Detlaff-Weglikowska U. (2004). Carbon nanotube sheets for the use as artificial muscles.” Carbon, 42, 1159-1164

Ward-Close C, Blom AF, Ritchie RO. Mechanisms associated with transient fatigue crack growth under variable-amplitude loading: An experimental and numerical study. *Eng Fract Mech*. 1989;32(4):613-638.

Whitby R.L.D., Fukuda T., Maekawa T., James S.L., and Mikhalovsky S.V. (2008). “Geometric control and tuneable pore size distribution of buckypaper and buckydiscs.” *Carbon,* 46, 949-956.

Yamada, T., Hayamizu, Y., Yamamoto, Y., Yomogida, Y., Izadi-Najafabadi, A., Futaba, D. N., & Hata, K. (2011). A stretchable carbon nanotube strain sensor for human-motion detection. *Nature Nanotechnology, 6*(5), 296-301.

Yekani Fard M., Liu Y., and Chattopadhyay A. (2012a). “Analytical solution for flexural response of epoxy resin materials.” *J. of Aerospace Engg.*, 25 (3), 395

Yekani Fard M., Liu Y., and Chattopadhyay A. (2012b). “Characterization of epoxy resin including strain rate effects using digital image correlation system.” *J. of Aerospace Engg.*, 25 (2), 308.

Yekani Fard M., Raji B., and Chattopadhyay A. (2014a). “The ratio of flexural strength to uniaxial tensile strength in bulk epoxy resin polymeric materials.” *J. of Poymer. Testing*, 40, 156-162.

Yekani Fard M., Sadat S.M., Raji B., and Chattopadhyay A. (2014b). “Damage characterization of surface and sub-surface defects in stitch-bonded biaxial carbon/epoxy composites.” Composites: Part B, 56 821-829.

You B, Lee S. A critical review on multiaxial fatigue assessments of metals. *Int J Fatigue*. 1996;18(4):235-244.

Young, Jasmine, “Continuous buckypaper manufacturing process: Process investigation and improvement” (2009). Electron Theses, Treaties and Dissertation. Paper 872.

Yu, X., & Kwon, E. (2009). A carbon nanotube/cement composite with piezoresistive properties. *Smart Materials and Structures, 18*(5), 055010.

Zenner H, Simbürger A, Liu J. On the fatigue limit of ductile metals under complex multiaxial loading. *Int J Fatigue*. 2000;22(2):137-145.

Zhang J., and Jiang D. (2012). “Influence of geometries of multi-walled carbon nanotubes on the pore structures of Buckypaper.” Composites: Part A, 43, 469-474.

Zhang S, Marissen R, Schulte K, Trautmann K, Nowack H, Schijve J. Crack propagation studies on al 7475 on the basis of constant amplitude and selective variable amplitude loading histories. *Fatigue & fracture of engineering materials & structures*. 1987;10(4):315-332.

Zhang X. (2008). “Hydroentangling: A novel approach to high-speed fabrication of carbon nanotube membranes.” *Adv. Mater.,* 20, 4140-4144.

Zhang, W., Picu, R., & Koratkar, N. (2007). Suppression of fatigue crack growth in carbon nanotube composites. *Applied Physics Letters, 91*(19), 193109.

Zhang, Z., Wei, H., Liu, Y., & Leng, J. (2015). Self-sensing properties of smart composite based on embedded buckypaper layer. *Structural Health Monitoring, 14*(2), 127-136.

Zhao T, Zhang J, Jiang Y. A study of fatigue crack growth of 7075-T651 aluminum alloy. *Int J Fatigue*. 2008;30(7):1169-1180.

Zheng C., Qian W., Yu Y., and Wei F. (2013). “Ionic liquid coated single-walled carbon nanotube buckypaper as supercapacitor electrode.” Particuology, 11, 409-414.

Zheng, C., Qian, W., Yu, Y., & Wei, F. (2013). Ionic liquid coated single-walled carbon nanotube buckypaper as supercapacitor electrode. *Particuology, 11*(4), 409-414

Zhu W., Ku D., Zheng J.P., Liang Z., Wang B., Zhang C., Walsh S., Au G., and Plichta E.J. (2010). “Buckypaper-based catalytic electrodes for improving platinum utilization and PEMFC’s performance.” Electrochimica Acta, 55, 2555-2560.